

The Pennsylvania State University
The Graduate School
College of Earth and Mineral Sciences

**CHARGED POINT DEFECT IN RUTILE TiO_2 :
FROM DEFECT CHARGE DISTRIBUTION
TO DEFECT PHONON FREE ENERGY**

A Dissertation in
Materials Science and Engineering
by
Xin Li

© 2010 Xin Li

Submitted in Partial Fulfillment
of the Requirements
for the Degree of

Doctor of Philosophy

May 2010

The dissertation of Xin Li was reviewed and approved* by the following:

Elizabeth C. Dickey
Professor of Materials Science and Engineering
Dissertation Advisor
Chair of Committee

Long-Qing Chen
Professor of Materials Science and Engineering

Clive A. Randall
Professor of Materials Science and Engineering

Suzanne E. Mohny
Professor of Materials Science and Engineering

Vincent H. Crespi
Professor of Physics
Professor of Materials Science and Engineering

Gary L. Messing
Professor of Materials Science and Engineering
Head of the Department of Materials Science and Engineering

*Signatures are on file in the Graduate School

Abstract

The dominant charged point defects in transition metal oxides can change with temperature (T) and oxygen partial pressure (PO_2) to control the electrical properties of the materials. Thus it is important to understand how the defect formation energies (DFEs) of all the defects are changed with T and PO_2 , which is not easily measured experimentally. Density Functional Theory (DFT) is combined with thermodynamics to construct a new methodology to calculate the DFEs *ab initio*. Rutile TiO_2 is chosen as a model material because it is a relatively simple binary system and there is a wealth of existing macroscopic experimental data, such as its dependence of the electrical conductivity on T and PO_2 , temperature dependent thermal expansion coefficient, etc.

Chapter 1 introduces the general method to calculate DFEs, which combines DFT with thermodynamics, including the supercell method to calculate the total energies of defective and pure supercells; the use of Bader analysis to analyze the real space charge distribution, which helps choose a potential alignment method to correct for the artificial interaction caused by periodic boundary conditions, and a thermodynamic approach to extrapolate DFEs to any T and PO_2 .

Chapter 2 discusses the temperature-dependent defect-induced phonon free energy in the harmonic approximation, which gives nontrivial contributions to the DFEs. The

temperature dependences of the defect-induced phonon free energies are different from the pure rutile structure, and more importantly they are different for differently charged defects. The physical origin is largely associated with the soft phonon mode at low frequencies for titanium interstitials, while for oxygen vacancies and titanium vacancies the differences in the phonon free energies are caused by the collective contribution from all phonon modes influenced by the introduction of the charged defects.

Chapter 3 points out the necessity of considering the thermal expansion of the materials in the DFE calculation. The differences between harmonic and quasi-harmonic approximations for the phonon free energy and Gibbs free energy calculations are discussed. Defect phase diagrams are constructed in the PO_2 - T - E_f spaces to explain how the dominant defect types change with environmental conditions.

Table of Contents

List of Figures	vii
List of Tables	xv
Acknowledgements	xvi
Chapter 1	
Background	1
Chapter 2	
Defect Formation Energy Calculation	7
2.1 Formula System	7
2.2 Density Functional Theory	9
2.3 Supercell Size Convergence Test	10
2.3.1 Charge localization and ionic displacement analysis	11
2.3.2 Influence of defect charge distribution on choice of correction method	19
2.3.3 Artificial elastic energy interaction	23
2.4 Defect Energetics	26
Chapter 3	
Charged Point Defect related Phonon Free Energy Calculations	34
3.1 Harmonic Calculation of Phonon Free Energy	34
3.2 Phonons in Pure Rutile TiO ₂	37
3.3 Phonons in Defective Supercells	42
3.3.1 Phonons in Ti interstitial defective supercells	47
3.3.2 Phonons in the vacancy defective supercells	60
3.3.3 Phonon PDOS and their correlations	62

Chapter 4	
Charged Point Defect related Gibbs Free Energy	65
4.1 Quai-Harmonic Calculation of Gibbs Free Energy in Pure Rutile	65
4.2 Quai-Harmonic Calculation of Gibbs Free Energy in Defective Structures	73
4.2.1 Ti interstitial defective supercells	73
4.2.2 Ti vacancy and O vacancy defective supercells	83
4.3 Defect Phase Diagrams	86
4.4 Conclusions	90
4.5 Future Work	91
Appendix	92
Bibliography	93

List of Figures

1.1 Electrical conductivity data from (a) Baumard et al. (b) Blumenthal et al. (c) Lee and Yoo (e) Nowotny et al. for single crystal rutile TiO_2 , and from (d) Balachandran and Error for polycrystalline rutile TiO_2 . 3

2.1 Average number of electron difference (dashed line) per (a) Ti ion and (b) O ion, or partial charge density difference on the atomic scale; and the average ion displacement (solid line) averaged over (a) Ti ion and (b) O ion inside each successive spherical shell within radius R and $R+\Delta R$ from the Ti_i^{4+} defect nucleus in the $3\times 3\times 5$ supercell. 13

2.2 (a) Average number of electron difference per ion, or total charge density difference on the atomic scale, averaged over all ions inside each successive spherical shell within radius R and $R+\Delta R$ from the defect nucleus for 223 and 335 sized differently charged Ti_i^q supercells. (b) Accumulated number of electron difference within radius R around defect nucleus between Ti_i^q defective and perfect supercells. Dashed lines are for 223 sized supercells and solid lines for 335 supercells. The charge states q of Ti_i^q for any group of curves are from 0 at the top to +4 at the bottom successively in both figures.

2.3 The energy of $E_\alpha - E_{perfect}$ (solid line) for Ti_i^{4+} (a) and $\text{V}_{\text{Ti}}^{4-}$ (b) after Makov-Payne correction (dashed line) and ΔV correction (dot-dashed line), respectively, as a function of the supercell sizes. 21

2.4 (a) The elastic strain energies calculated from the external pressures on the constant volume supercells as a function supercell sizes, using formula $E_p = \frac{P}{|P|} \frac{1}{2} \frac{VP^2}{Y}$
 (b) The comparison of the convergence between the constant volume ($E_\alpha - E_{perfect}$) and zero pressure method ($E_\alpha - E_{perfect} - |E_p|$) after ΔV correction for $\text{V}_{\text{Ti}}^{4-}$ and $\text{V}_{\text{Ti}}^{1-}$ supercells. 24

2.5 DFE as a function of E_f at different temperature and PO_2 . The gray areas are forbidden by the charge neutrality condition. CBM is labeled for its experimental values at different temperatures, at 300K it is at 3eV. The insets in plots (a-c) enlarge the transition regions for each type of defect, respectively, which shows that the transition levels are ordered. The transition regions of titanium vacancies are cut by the zero value of Fermi level or the valance band maximum, thus most of them are not seen except for $\text{V}_{\text{Ti}}^{3-}$ and $\text{V}_{\text{Ti}}^{4-}$. 27

2.6 Dominant point defect distribution in the 2D phase space. 32

3.1 Calculated Phonon dispersion curves for pure rutile TiO_2 compared with the neutron inelastic scattering experiments. 40

3.2 Phonon Density of States (DOS) for pure rutile at the q-mesh of 8x8x8. The total

DOS (TDOS) can be further decomposed into partial DOS (PDOS) of Ti and O, respectively. 40

3.3 Calculated phonon free energy for pure rutile TiO_2 compared with the experimental data from NIST database. 41

3.4 Phonon DOS of differently charged Ti interstitial defective supercells for (a) Ti_i^{4+} and Ti_i^{3+} at $2 \times 2 \times 3$ sized supercells, (b) Ti_i^{2+} and Ti_i^{1+} at $2 \times 2 \times 3$ sized supercells, (c) Ti_i^0 at $2 \times 2 \times 3$ sized supercells (d) Ti_i^{4+} at $2 \times 2 \times 3$ sized and $3 \times 3 \times 5$ sized supercells 43

3.5 Phonon DOS of differently charged (a) VTi^q supercells and (b) VO^q supercells at the supercell size of $2 \times 2 \times 3$. 44

3.6 Phonon free energy difference from all optical phonon modes between a $2 \times 2 \times 3$ supercell with a Ti_i^{q+} defect and the perfect structure as a function of temperature. 45

3.7 Phonon free energy difference from all optical phonon modes between a $2 \times 2 \times 3$ supercell with a $\text{V}_{\text{Ti}}^{q-}$ defect and the perfect structure as a function of temperature. 45

3.8 Phonon free energy difference from all optical phonon modes between a $2 \times 2 \times 3$ supercell with a V_O^{q+} defect and the perfect structure as a function of temperature. 46

3.9 Optical phonon frequency differences at the Gamma point for the lowest 120 modes between Ti_i^{4+} and Ti_i^{3+} defect structures in a $2 \times 2 \times 3$ supercells. 47

3.10 Phonon dispersion curves of Ti_i^{4+} (left) and Ti_i^{3+} (right) for the lowest 120 optical modes. 48

3.11 Phonon free energy difference from all the optical phonon modes except for the lowest one between $\text{Ti}_i^{\text{q}+}$ defective 2x2x3 supercells and the perfect structure as a function of temperature. 49

3.12 Phonon free energy difference between Ti_i^{4+} and Ti_i^{4+} structures with and without the 1st optical phonon mode. 49

3.13 The optical phonon mode, ω_{1st}^O , that contributes most to the phonon free energy difference between Ti_i^{4+} and Ti_i^{3+} defect structures at high T. The Ti interstitial defect ion is labeled in green; other Ti ions are labeled in gray and oxygen ions are labeled in red. The arrows show the oscillation directions of the ions near the Ti interstitial defect ion. The viewing direction is along the x-axis for the main figure, while the inset is along the z-direction. Four out of the six O 1NNs of the defect ion are connected by the dashed lines, which forms a plane for the defect ion to oscillate in. 51

3.14 The differences in the number of electrons within the Bader volume of each ion, N_e , for all the corresponding ions between Ti_i^{3+} and Ti_i^{4+} defective supercells. The numbers on the x axis are sorted based on their distances, R , from the defect ion starting from the nearest one. Groups of the oxygen ions with equal distance from the defect ion are labeled with increasing numbers below the symbols, while titanium ion groups are labeled above. 53

3.15 The differences in the distance from the defect ion to each ion, R , for all the corresponding ions between the Ti_i^{3+} and Ti_i^{4+} defective supercells. The numbers on the x axis are sorted based on their distances, R , from the defect ion starting from the nearest

one. Groups of the oxygen ions with equal distance from the defect ion are labeled with increasing numbers below the symbols, while titanium ion groups are labeled above. 54

3.16 Calculated forces on the defect ion along the z-direction from different groups of Ti ions in the two defective supercells. The numbers of groups correspond to the numbers labeled in Figure 3.14 and 3.15. The defect ion is displaced along the positive z direction by 0.02 Angstrom. 56

3.17 Calculated forces on the defect ion along the z-direction from different groups of O ions in the two defective supercells. The numbers of groups correspond to the numbers labeled in Figure 3.14 and 3.15. The defect ion is displaced along the positive z direction by 0.02 Angstrom. 57

3.18 Restoration force difference along the z-direction between the corresponding ion groups in the Ti_i^{3+} and Ti_i^{4+} defective supercells. The numbers of groups correspond to the numbers labeled in Figure 3.14 and 3.15. The defect ion is displaced along the positive z direction by 0.02 Angstrom. 57

3.19 The N_e differences for all the corresponding ions before and after the displacement of the defect ion along positive z direction by 0.02 Angstrom, in the Ti_i^{3+} and Ti_i^{4+} defective supercells, respectively. The numbers on the x axis are sorted based on their distances, R, from the defect ion starting from the nearest one. 58

3.20 Optical phonon frequency differences at the Gamma point for the lowest 150 modes between VTi^{4-} and VTi^{3-} defect structures at 2x2x3 supercells. 61

3.21 Optical phonon frequency differences at the Gamma point for the lowest 150 modes

between VO^{2+} and VO^{1+} defect structures at $2 \times 2 \times 3$ supercells. 62

3.22 Correlations of phonon PDOS between the corresponding ions in the defective and pure supercells at the size of $2 \times 2 \times 3$ unit cells, sorted by their distances from the defect ion. The empty symbols are for O ions and filled symbols are for Ti ions. 64

4.1 Calculated $V_{\min}(T)$ as a function of T up to 1800K in the quasi-harmonic approximation 68

4.2 Calculated volume thermal expansion coefficient compared with experimental data from two different groups up to 1800K. 69

4.3 Calculated molar Gibbs free energy, μ_{QHA}^{Calc} , from the quasi-harmonic approximation; experimental chemical potential, μ^{Expt} ; calculated molar phonon free energy from the quasi-harmonic approximation, F_{QHA}^{Calc} ; and the calculated internal energy, U_{QHA}^{Calc} , from the quasi-harmonic approximation as functions of temperature. 70

4.4 Calculated phonon modes with volume expansion in the unit cell of pure rutile TiO_2 . 72

4.5 Calculated phonon free energy differences between Ti_i^{q+} defective supercells and the pure supercell from the quasi-harmonic approximation. 75

4.6 Lowest 30 optical phonon modes at Gamma point as a function of volume in Ti_i^{4+} , Ti_i^{3+} and pure $2 \times 2 \times 3$ sized supercells. The modes in the highly symmetric pure structure are mostly degenerate, while most modes in the defective supercells are non-degenerate. 75

4.7 Phonon DOS of Ti_i^{3+} and Ti_i^{4+} defective supercells at volume V_0 (left) and $1.05V_0$

(right).

76

4.8 (a) The internal energy, U , plus phonon free energy F_{ph} as a function of supercell volume for pure, Ti_i^{3+} and Ti_i^{4+} 2x2x3 sized supercells at 0K. Note all three curves are shifted in y direction to make them visible in the same energy scale, but this does not influence the definition of ΔE for each defect. (b) The difference between the ΔU of the Ti_i^{q+} defective supercells and the ΔU of the pure supercell as a function of temperature, where ΔU is the internal energy part of the ΔE defined in (a).

77

4.9 Number of electrons within the Bader Volume of each ion (N_e) as a function of volume expansion of the supercell, for (a) Ti ions in Ti_i^{4+} supercell, (b) O ions in Ti_i^{4+} supercell, (c) Ti ions in Ti_i^{3+} supercell, (d) O ions in Ti_i^{3+} supercell. The ion group numbers correspond to the ones defined in Figure 3.14 and 3.15.

79

4.10 Difference between the distances of the ions to the defect ion, $R(V)$, at a certain volume V , and the distances at the volume V_0 , $R(V_0)$, in (a) Ti_i^{4+} supercell for Ti ion groups, (b) Ti_i^{3+} supercell for Ti ion groups, (c) Ti_i^{4+} supercell for O ion groups, (d) Ti_i^{3+} supercell for O ion groups. The ion group numbers correspond to the ones defined in Figure 3.14 and 3.15.

81

4.11 Calculate ΔU differences between Ti_i defective supercells and the pure one from the quasi-harmonic approximation. ΔU is the internal energy change referenced to the energy at 0K.

82

4.12 Calculated Gibbs free energy differences between Ti_i^{q+} defective supercells and the pure one from the quasi-harmonic approximation.

83

- 4.13 Phonon free energy difference between V_{Ti}^{4-} defective supercell and pure supercell calculated with the quasi-harmonic (QHA) and harmonic approximation (HA), respectively. 84
- 4.14 The Gibbs free energy difference between V_{Ti}^{4-} defective and pure supercells calculated with the quasi-harmonic approximation. 85
- 4.15 ΔU differences between V_{Ti}^{4-} defective supercell and the pure supercell calculated from the quasi-harmonic approximation. ΔU is the internal energy change referenced to the one at 0K. 85
- 4.16 Calculated 2-D defect phase diagrams for rutile TiO_2 at 1300K based on (a) the Gibbs free energies G as defined in eq (1.1) and (b) the internal energies U as defined in eq (1.2). The calculated unique Fermi level (E_F) from the electroneutrality condition as a function of PO_2 at 1300K is labeled by red line. 86
- 4.17 Calculated Brower diagram for rutile TiO_2 at 1300K. 90

List of Tables

2.1 Lattice parameter calculated from DFT compared with experiments	11
2.2 DFE after different correction methods. The two MP(q) terms are the Makov-Payne 1 st and 2 nd order corrections by defining the point charges with different radii around the defects between 0.7 to 2 Å.	22
2.3 The DFE of differently charged Frenkel and Schottky pairs compared with experimental values. The calculated pair energies are the direct summation of the individual DFEs calculated using eq (1) thus does not include the association energy between the individual defects, which agrees with the experimental condition of dilute solution.	29
2.4 Total energy differences between successive charge states of titanium interstitial defective supercells show the equal energy difference phenomenon.	30
3.1 Calculated optical phonon frequencies at Gamma point (THz) from different exchange correlation potentials and different explicitly treated electrons, compared with experimental data from optical or neutron scattering measurements.	38

Acknowledgements

I first would like to thank my advisor Professor Elizabeth C. Dickey for her enlightening guidance in the past five years, for her fully support to my research, adventure, and career plan, and also for her patience, tolerance and wisdom to me all the way.

I would also like to thank Professor Mike W. Finnis in England for his important advice and help, and all the Professors in my comprehensive and Ph.D committee for their helpful intellectual interactions with me, including Professor. Long-Qing Chen, Professor Clive A. Randall, Professor Zi-Kui Liu, Professor Vincent H. Crespi, Professor Suzanne E. Mohny.

Special thanks to my wife Dr. Wei Jiang for her understanding, support, resolution, heart and wisdom.

I would also like to thank Jason Britson for his proof reading of my dissertation.

Chapter 1

Background

Charged point defects in TiO_2 are largely responsible for its electrical properties, which have been measured experimentally by several groups [1-5]. Nonetheless, controversies remain about the dominant point defects responsible for the conductivity behavior in certain temperature (T) and oxygen partial pressure (PO_2) ranges, as shown in Figure 1.1. At temperatures above 1600 K and in the reduced PO_2 regime (10^{-11} - 10^{-2} atm) Baumard et al. [1] (Fig. 1.1a) and Blumenthal et al. [5] (Fig. 1.1b) find the measured electrical conductivity versus PO_2 is best fit by a log-log slope of -1/5, which leads to their conclusions that fully charged titanium interstitials (Ti_i^{4+} in Kröger-Vink notation) dominate in this region (Related mass action relation is in Appendix). However, neither study measures directly the impurity concentration in the sample or pays specific attention to thermal equilibrium, although the impurity level is estimated to be around 30ppm in Baumard's sample[6]. At intermediate temperatures, there are more

discrepancies in the data than the previous high temperatures. For example, Baumard et al. [1] measure the electrical conductivity versus PO_2 between 1200K and 1600K in the PO_2 range of 1 atm to 10^{-15} atm obtaining a log-log slope of -1/5, and concluding that fully charged Ti interstitials, Ti_i^{4+} , are dominant, while Blumenthal et al. [5] find there was a slope transition from -1/6 to -1/4 with decreasing PO_2 and conclude that Ti_i^{3+} dominates in the low PO_2 range. In addition, Balachandran and Erer [7] find a slope of -1/6 between 1123K and 1323K in a PO_2 range of 10^{-20} atm to 10^{-10} atm in the polycrystalline rutile TiO_2 and conclude fully charged oxygen vacancies, V_O^{2+} , to be dominant, while at intermediate PO_2 (10^{-10} atm to 1 atm) they speculate that impurities may play a role in their samples to give the slope of -1/4. More recent studies by Lee and Yoo [8] claim Ti_i^{3+} , Ti_i^{4+} , and V_O^{2+} successively dominate as PO_2 increases from 10^{-15} atm to 1 atm between 1200K and 1400K, while Nowotny et al. [3] claim V_O^{2+} dominates at low PO_2 ($<10^{-10}$ atm), while at intermediate PO_2 from 10^{-10} atm to 1 atm, both V_O^{2+} and V_Ti^{4-} dominate. Both of these latter groups pay specific attention to the defect redistribution thermal equilibrium with changing PO_2 and T, and measure directly the impurity level in the samples. The impurity level is 32ppm in Nowotny et al.'s sample and less than 5ppm in Lee and Yoo's sample. Considering that the intrinsic defect concentration can be as low as 10ppm between 10^{-10} atm and 1 atm in the intermediate temperature range in rutile TiO_2 [6, 7, 9, 10], the extremely low impurity level in Lee and Yoo's sample makes their data more representative of the intrinsic defect chemistry in rutile TiO_2 .

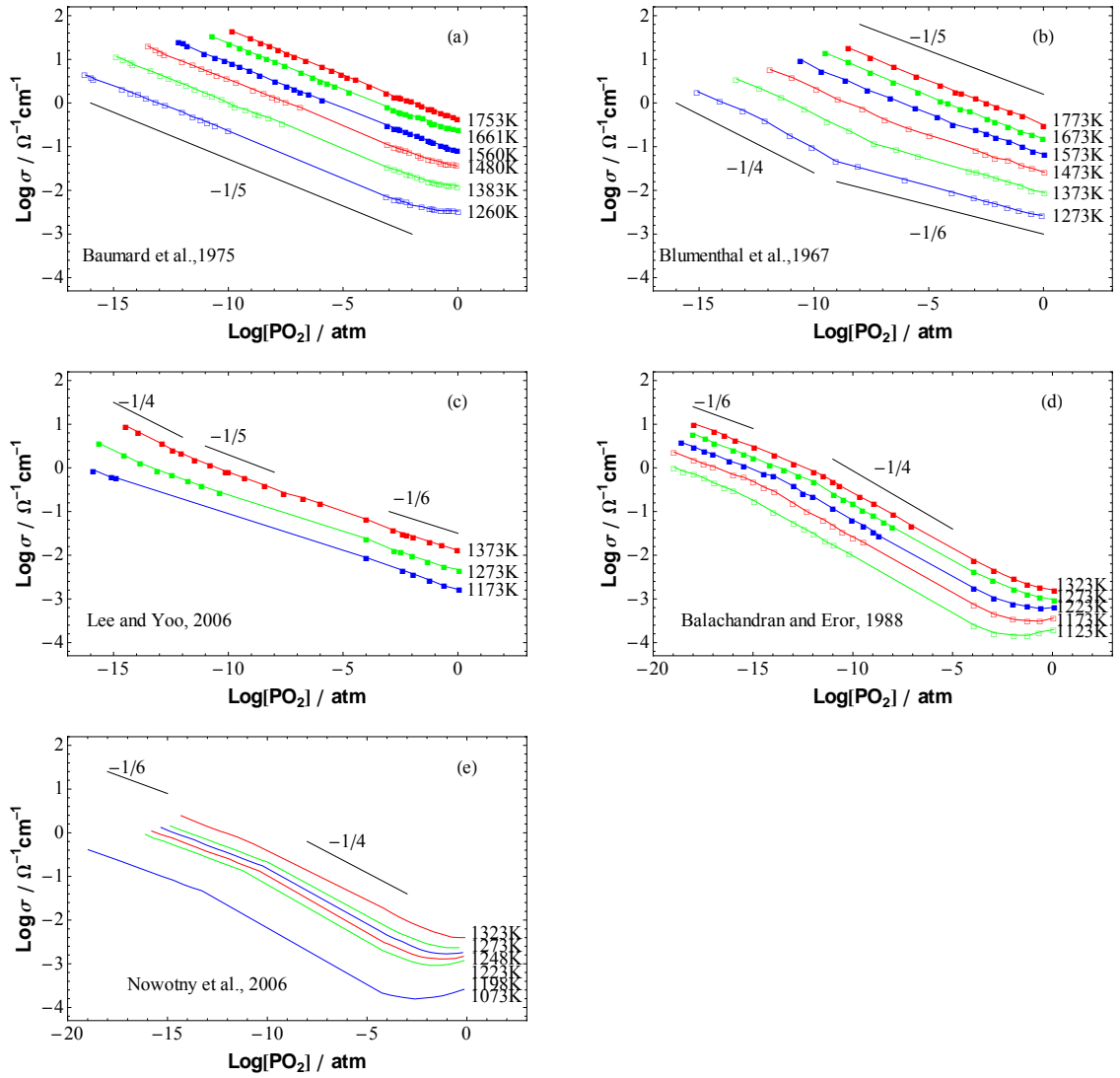


Figure 1.1 Electrical conductivity data from (a) Baumard et al. [1] (b) Blumenthal et al.[5] (c) Lee and Yoo[8] (e) Nowotny et al.[3] for single crystal rutile TiO_2 , and from (d) Balachandran and Eror [7]for polycrystalline rutile TiO_2 .

Not only do the conflicting experimental data provide some confusion about the nature of the dominant defects, but, in addition, there may be more than one possible

dominant defect that can explain the conductivity behavior in certain T and PO₂ ranges from the mass action analysis. For example, the measured slope of -1/4 in the ln(conductivity) vs. ln(PO₂) behavior in TiO₂ in the high-T (1400K) and low PO₂ (< 10⁻¹⁰ atm) regime can correspond to either Ti_i³⁺ or V_O¹⁺ [5, 8], so the dominant defect may not be unambiguously determined by these methods. There is therefore a need to understand point defect thermodynamics from a more fundamental, theoretical perspective.

To provide a predictive understanding of the point defect and electronic behavior of transition metal oxides, there have been considerable efforts to calculate charged point defect formation energies (DFEs) by Density Functional Theory (DFT) [11-16], since the magnitudes of the DFEs decide the charged defect concentrations through Boltzmann distributions and hence determine the electronic carrier concentrations through electroneutrality conditions. For rutile TiO₂, Cho et al.[17] studied the electronic structures and charge distributions of neutral defects, which can give complementary information to the real space charge distribution analysis in charged defect structures discussed in Chapter 2. Iddir et al.[18] calculated the neutral titanium interstitial and oxygen vacancy in rutile TiO₂ and paid specific attention to their migration energies and associated kinetic processes. He and Sinnott [19] calculated the formation energy of a Frenkel pair in rutile TiO₂ by a 2x2x3 sized supercell, which shows the DFE of the pair increases with increasing distance between the interstitial and vacancy defects. This suggests for the DFE calculation of an individual charged point defect that large supercells are necessary to avoid interactions between neighboring defects in the periodic

supercells. He et al. [20] also calculated the DFEs of individual charged point defects in 2x2x3 sized supercells. Unfortunately, the Makov-Payne correction [21], which corrects for the artificial electrostatic interaction between charged point defects by the periodic boundary condition implemented in the supercell approach, was applied in a wrong way as pointed out in ref. [13], which invalidates the presented energies and related analysis in this work[20]. Ma et al. [22] calculated charged point defects in a 2x2x2 supercell without applying any correction method for the above mentioned artificial interactions, making their results problematic. As explained in this thesis and presented in ref. [13], the Makov-Payne correction is, in fact not, an appropriate correction method for charged defect calculations in rutile TiO₂, thus a better potential alignment correction method[23, 24] was applied. The supercell size convergence test up to 3x3x5 unit cells was also done for all the charged defective supercells by ref. [13]. Most recently, Finazzi et al. [25] calculated the neutral Ti interstitial in a 2x2x3 sized supercell with a Hybrid functional in a spin-polarized calculation, and found the degree of localization of the extra electrons introduced by the defect ion is influenced by the ratio of the Hartree-Fock component in the hybrid functionals. However, the adjustment of this ratio is somewhat arbitrary. Furthermore, there was argument by Zheng et al.[12] that although the choice of different hybrid functionals may improve the calculated bandgap for transition metal oxides, the DFEs should not be affected by the bandgap correction.

To calculate the DFEs at a certain T and PO₂, the prior literature has typically used a combination of DFT with thermodynamics[11-16, 26]. However, most use only the two

thermodynamic limits to calculate the DFEs at the oxygen-rich and oxygen-poor boundaries, instead of predicting the specific DFEs over a range of T and PO_2 . The present work takes a more rigorous approach to calculate the chemical potential for O and Ti in rutile TiO_2 at 0K based on a well-defined zero energy reference state of DFT calculation, upon which their values at any T and PO_2 are decided and can be compared directly with DFT-calculated total energies of defective and pure supercells, which can give a definite value of DFE between the two thermodynamic boundaries[13, 20, 26, 27].

Furthermore, in most previous works [11-16, 26] the DFEs are approximated by the defect formation internal energy, U , which assumes that the temperature dependence of the Gibbs free energy is identical between the defective and pure structures. This thesis will show this is not true in rutile TiO_2 system. By considering the temperature dependent defect-induced phonon free energies and Gibbs free energies, which were largely neglected in most previous works [11-16, 26], the calculated stability ranges for partially charged oxygen vacancies and titanium interstitials are expanded, explaining some experimental observations (e.g. the -1/4 slope in the high- T , low PO_2 regime of TiO_2 discussed above)[8, 28]. Also, the contributions of the Gibbs free energies stabilize the titanium vacancy at high T in the p-type region, which matches better the n-p transition point from experiments[1, 3, 5, 6].

All of the above discussed effects will be finally reflected in the defect phase diagrams constructed in the PO_2 - T - E_f spaces to help clarify the experimental discrepancies.

Chapter 2

Defect Formation Energy Calculation[13]

2.1 Formula System

From a DFT perspective, the rigorous definition of a DFE is:

$$\Delta G = G^{defect} - G^{pure} \pm \mu(T, PO_2) + qE_f \quad (2.1)$$

where G^{defect} and G^{pure} are the Gibbs free energies of the defective and the pure structures, respectively. The atom chemical potential $\mu(T, PO_2)$ for the Ti or O atom is used to balance the number of atoms between the two systems, and depending on the defect type the sign in front of the term will be positive for a vacancy or negative for an interstitial defect. The electron chemical potential, E_f , is used to balance the number of electrons between the structures, depending on the charge state, q , of the defect. However, in the practical calculations, the first two Gibbs energy terms in eq (2.1) are usually simplified to the total energy or internal energy terms U^{defect} and U^{pure} calculated from DFT at 0K, with the assumption that the temperature-dependant phonon free energies and the volume-dependant DFE changes can be neglected[11, 13, 20, 24, 29]. In this chapter

this widely used simplified formula (eq. (2.2)) is used initially to calculate the DFEs:

$$\Delta U = U^{defect} - U^{pure} \pm \mu(T, P_{O_2}) + qE_f \quad (2.2)$$

There are different methods to calculate the atom chemical potential $\mu(T, P_{O_2})$ in the literature [11, 13, 20, 24, 29], with most using the chemical potential of the atom at the two thermodynamic boundaries of oxygen-poor (n-type) and oxygen-rich (p-type) status. Here a further step is taken to give the exact chemical potential of the Ti or O atom in rutile TiO_2 at a given T and PO_2 [13, 20]. The chemical potential term is thusly divided into several sub-terms that can be either calculated by *ab initio* methods or measured experimentally with specified T and PO_2 dependence. For oxygen:

$$\begin{aligned} \mu_O &= \mu_O^0 + \Delta\mu_O^0(T) + \frac{1}{2}k_B T \ln\left(\frac{P_{O_2}}{P^0}\right) \\ &= \frac{1}{2}(\mu_{TiO_2}^0 - \mu_{Ti}^0 - \Delta G_{f, TiO_2}^0) + \Delta\mu_O^0(T) + \frac{1}{2}k_B T \ln\left(\frac{P_{O_2}}{P^0}\right) \end{aligned} \quad (2.3)$$

which was originally applied to the Al_2O_3 system by Finnis and coworkers [27, 30];

and for titanium:

$$\mu_{Ti}(T, P_{O_2}) = \mu_{TiO_2}^0 - 2\mu_O(T, P_{O_2}) \quad (2.4)$$

In eq (2.3) and (2.4) the standard chemical potential of a Ti atom, μ_{Ti}^0 , and rutile TiO_2 molecular unit, $\mu_{TiO_2}^0$, are calculated by DFT calculations at 0K. The temperature-dependant part of the chemical potential of oxygen at standard pressure, $\Delta\mu_O^0(T)$, and the standard formation energy, $\Delta G_{f, TiO_2}^0$, are taken from the NIST thermodynamic experimental database [31]. As pointed out by Finnis et al. [32], the standard chemical potentials for TiO_2 and Ti calculated at 0K by DFT are adequate

estimates for the standard temperature and pressure because rutile TiO_2 and metallic Ti are solids. Thus in eq (2.3) the chemical potential of oxygen at 0 K, μ_O^0 , has a well-defined zero energy reference state of DFT calculation at 0K, which makes the chemical potential of O and Ti in the formula system valid to be directly compared with the calculated total energies of defective and pure structures, U^{defect} and U^{pure} , by DFT. With this approach, the DFEs at high temperature, different oxygen partial pressure and Fermi level can be calculated on an *ab initio* basis.

2.2 Density Functional Theory

Instead of diagonalizing the wavefunctions for a many-electron system using the N -particle Schrodinger equation, DFT calculates the ground-state charge density of the whole system, which makes it computationally practical for real materials, and especially low-symmetry defective supercells. All properties of a quantum many-body system can be considered to be unique functionals of the ground state density[33], with the present-day method for treating condensed matter given by W. Kohn and L.J. Sham [34]. The method includes the kinetic energy of non-interacting electrons in terms of independent particle wavefunctions, with interaction terms explicitly treated in the exchange-correlation energy functional of the density $E_{xc}[n]$. The accuracy of a practical calculation based on the Kohn-Sham approach is only limited by the approximations in $E_{xc}[n]$, which are usually approximated as a local or nearly local functional of the density. In the local density approximation (LDA) the exchange correlation energy density is

assumed to be the same as the homogeneous electron gas locally. The generalized gradient approximation (GGA), such as GGA-PBE[35], takes a further step by including the magnitude of the gradient of the density in the functional. The recent development of hybrid functionals, such as PBE0[36] or HSE06[37], which is a combination of orbital-dependent Hartree-Fock and an explicit density functional, may improve the bandgap calculations for the system with relatively high correlation [38].

2.3 Supercell Size Convergence Test

The total energies of defective and pure structures, U^{defect} and U^{pure} , in eq (2.2) are calculated from DFT with the supercell approximation [11, 13, 20, 24, 29]. DFT calculations are carried out using the Vienna Ab-initio Simulation Package (VASP) [39, 40]. The calculations use the generalized gradient approximation Perdew-Burke-Ernzerhof (GGA-PBE) [35] exchange-correlation functionals to obtain the ground-state energies of the supercells. Projector augmented wave (PAW) pseudopotentials [40, 41] that explicitly calculate the $3s^2 3p^6 3d^2 4s^2$ electrons for titanium and the $2s^2 2p^4$ electrons for oxygen are used for all calculations. The cutoff-energy of 354 eV and k-points sampling of $4 \times 4 \times 4$ are determined after careful tests for convergence. The total-energy and residual-force convergence criteria are set to 10^{-4} eV and 0.01 eV/Å, respectively. The calculated lattice parameters of the defect-free unit cell are listed in Table 1, and these are then used to build the supercell.

	a / Å	c / Å
Experiment	4.59	2.96
GGA-PBE	4.65	2.97
	+1.3%	+0.3%

Table 2.1. Lattice parameter of rutile TiO₂ calculated from DFT compared with experiments.

Supercell size convergence is an important issue for charged point defect calculations with periodic boundary conditions. The finite-size effects arising from electrostatic interactions between a charged defect and its periodic images are accessed through the valence-band offset, or ΔV , correction [23] and the Makov-Payne approach [21, 42]. The defective supercells of various sizes from 2x2x2 to 3x3x5 TiO₂ unit cells are examined to evaluate the convergence with increasing supercell size of the DFEs, charge density distribution, external pressure and correction energies. A protocol is finally adopted for obtaining accurate defect formation energies in the TiO₂ system, namely to use as large a supercell as computationally feasible in a 30 days time frame for each defective supercell (in this case 3x3x5 unit cells) and to apply the ΔV correction. The NSF-Teragrid clusters are used for the total energy calculations in this chapter and the phonon calculation in chapter 3 and 4.

2.3.1 Charge localization and ionic displacement analysis

The aim of this section is to give a quantitative procedure for defining the spatial distribution of the Kroger-Vink charge of a defect. This is very important because the lattice around the defect is discrete, strained and polarized, making it problematic simply

to integrate the charge over a region around the defect. For any defective supercell, such as Ti_i^q , the charge state q is not defined without a clear statement of the reference state. In most cases, including the Kroger-Vink convention, the reference background is the perfect supercell. Thus it is the charge density difference between the defective and the perfect supercells that defines the charge associated with point defect Ti_i^q .

A point-by-point subtraction of the charge density of the perfect lattice from the charge density in the defective supercell will exhibit huge spatially dependent oscillations due to the displacements of the nuclear positions around the defect, which carry with them a proportion of the electron density. Instead, a course-graining, discretization procedure for the charge density is employed and mapped onto individual ions. All the electronic charges are allocated to individual ions according to the Bader prescription [43], for both the defective and the perfect crystals. In order to define excess charge the subtraction is then done not point by point in space but atom by atom, which gives the excess charge as a function of distance from the defect.

The Bader volume of each ion is defined by the surface around it whose normal points along the direction in which the surrounding charge density has zero gradient. These volumes fill the space of the supercell seamlessly without empty space or overlap. The integrations of all the electrons inside each unit region defined by the Bader volumes in a perfect supercell give a value of 7.1 electrons around each oxygen ion and 9.8 electrons around each titanium ion. In the perfect crystal this defines an ionic charge of -1.1 for the oxygen ion and +2.2 for the titanium ion, which agrees reasonably well with

the experimental analysis of the effective charge state of a titanium ion in rutile TiO_2 [44], although we do not presume it to have any absolute physical meaning. They also agree well with the results of a simple analysis of the relationship between electronegativity and charge state [45], where the Pauling electronegativity difference between O of 3.5 and Ti of 1.6 [44] predicts a charge state of -1.1 for the O ion in TiO_2 .

Figure 2.1 (a)

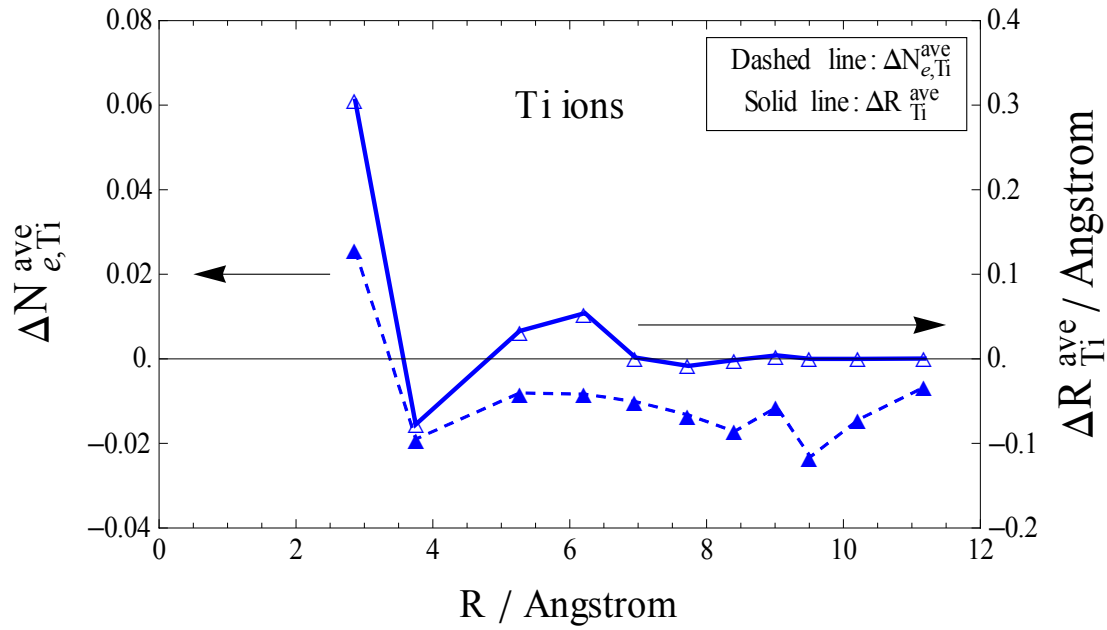


Figure 2.1 (b)

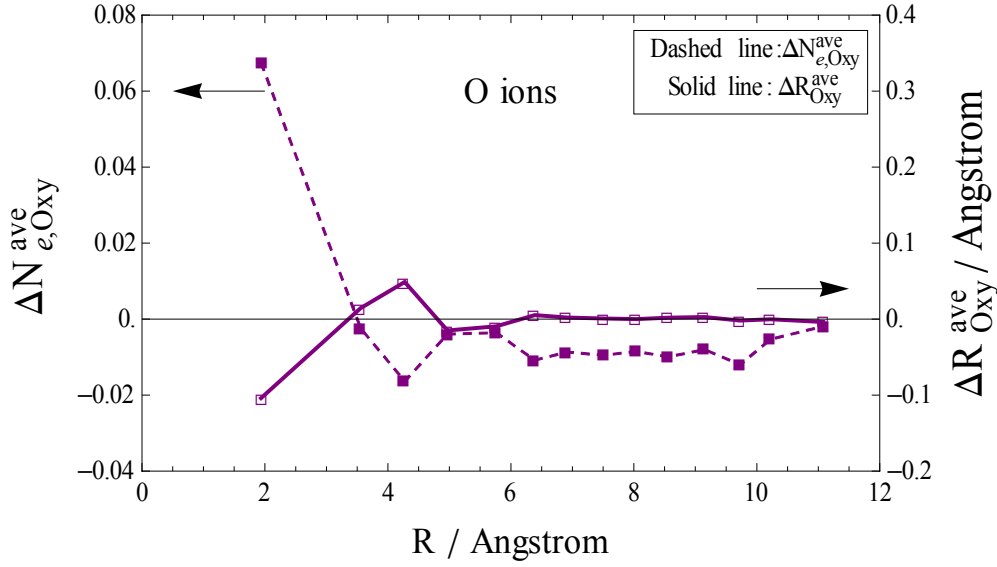
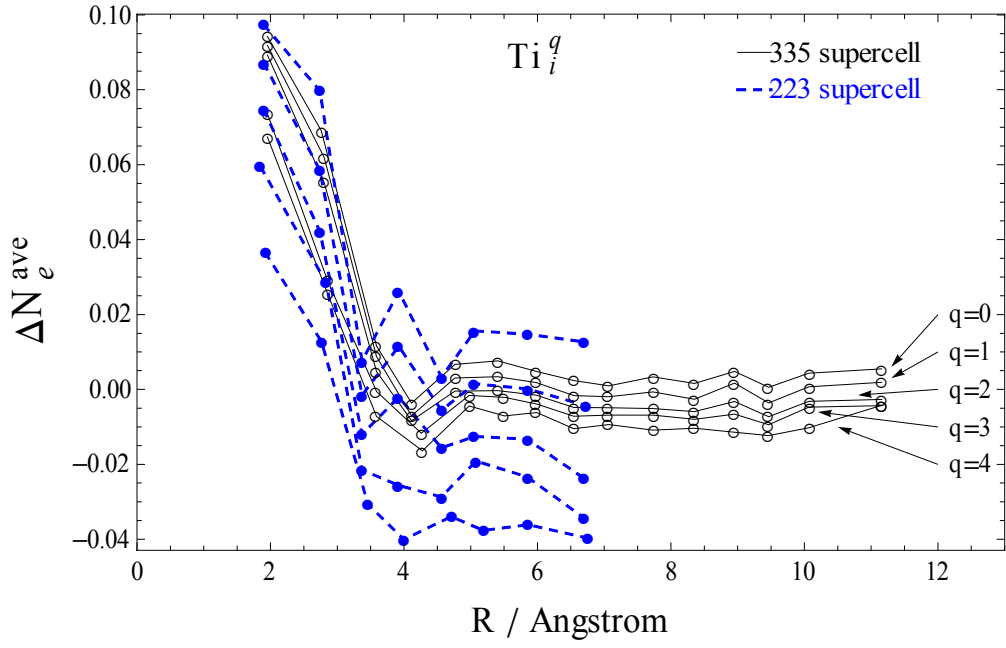


Fig 2.1. Average number of electron difference (dashed line) per (a) Ti ion and (b) O ion, or partial charge density difference on the atomic scale; and the average ion displacement (solid line) averaged over (a) Ti ion and (b) O ion inside each successive spherical shell within radius R and $R+\Delta r$ from the Ti_i^{4+} defect nucleus in the $3 \times 3 \times 5$ supercell.

The number of electrons that belong to each Ti or O ion in the defective and perfect supercells can be obtained by integrating over the respective Bader volumes, and their difference is then calculated. Figure 2.1 illustrates the average number of electron difference (dashed line) and average displacement (solid line) per Ti or O ion inside the successive spherical shells around the Ti interstitial nucleus as a function of distance R from the defect. The thickness Δr of each spherical shell is chosen by the criteria that the

distance between any two ions is always less than 0.5 Å within each shell. The choice of other values for the criteria should not influence our major conclusion. However, a too small value might introduce noise while a too large value might hide the useful details. It shows that the first nearest neighbor (1NN) O ions in Figure 2.1(b) and second nearest neighbor (2NN) Ti ions in Figure 2.1(a) of the Ti interstitials all have positive electron differences, which is due to the partial transfer of charge from these neighbors to the interstitial or farther regions. Beyond the 2NN shell, the charge transfer fluctuates all the way to the edge of the supercell. Comparison of Figures 2.1(a) and (b) indicates that for titanium ions the relaxations toward the titanium interstitial are mostly accompanied with a loss of electrons within their Bader volumes, and the relaxations away from the defect nucleus are associated with gain in local electron density; while for oxygen ions the opposite trend is implied. This is as one would expect if the relaxations are driven by the electrostatic interactions of the ions. The ionic displacements in the defective supercell are found to converge to the perfect crystal values more quickly with increasing distance from the defect site than the charge density.

(a)



(b)

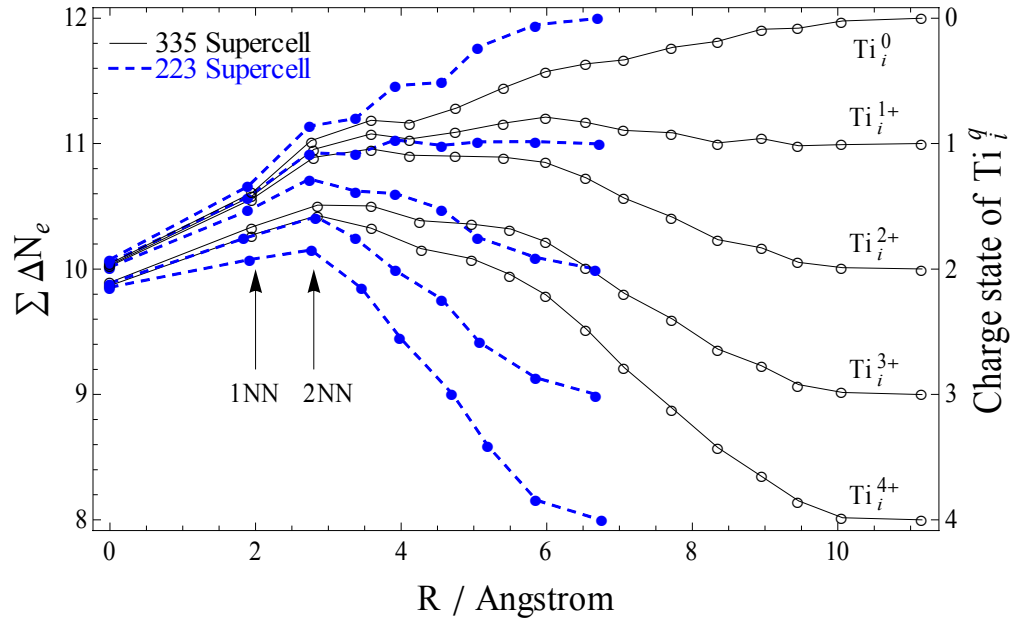


Fig 2.2 (a) Average number of electron difference per ion, or total charge density difference on the atomic scale, averaged over all ions inside each successive spherical shell within radius R and $R+\Delta R$ from the defect nucleus for 223 and 335 sized differently

charged Ti_i^q supercells. (b) Accumulated number of electron difference within radius R around defect nucleus between Ti_i^q defective and perfect supercells. Dashed lines are for 223 sized supercells and solid lines for 335 supercells. The charge states q of Ti_i^q for any group of curves are from 0 at the top to +4 at the bottom successively in both figures.

The spatial extent of the defect charge density is now examined in more detail. Figure 2.2(a) shows the total charge density difference oscillation as a function of distance from the defect nucleus for differently charged Ti_i^q supercells at two different sizes. The excess charge on the nearest neighbors of the interstitial atom is surprisingly insensitive to the charge in the supercell. In the smaller supercell the average charge carried by the nearest neighbors varies in the range -0.1 to -0.03 while the charge in the supercell varies over the whole range from 0 to +4. In the larger supercell, where the excess charge has more room to spread, the variation in charge localized on the nearest neighbors is even less. The charge densities also oscillate with much higher amplitudes as a function of distance from the interstitial in 2x2x3 supercells compared with the 3x3x5 supercells. By summing the electron difference within each discrete radius, the total electron difference around the defect nucleus can be plotted as a function of distance from the defect nucleus, as shown in Figure 2.2(b) for the same set of charged Ti_i^q

supercells of two different sizes. The values for the interstitial itself $\sum \Delta N_e (R=0)$ are all close to 10 regardless of the charge of the overall supercell. A neutral interstitial would have a value $\Delta N_e^{tot} = 12$, which shows that the charge states within the Bader volumes of the titanium interstitial at $R=0$ are always around +2 for all differently charged Ti_i^q supercells, just as they are for Ti lattice sites in the perfect crystal. This result is consistent to the model about the charge self-regulation around a transition metal ion in semiconductors to make the local charge of the ion constant, no matter what the oxidation states of the supercells are[46] .

For the Ti_i^{1+} supercell illustrated in Figure 2.2(b) the excess charge has all been accommodated at the interstitial and its first and second neighbors, a region well within the faces of the supercell. In the other cases, it is clear that the size of the supercell is strongly affecting the charge distribution, because the excess charge density is varying right up to the faces of the supercell. In an infinitely large supercell the amplitude of the charge density oscillation would damp to zero at a certain distance. Within this range all the structural distortion and charge density difference oscillation are the intrinsic structures of the point defect, Ti_i^q , while from any viewpoint far beyond this range the charge state of this entity is always the nominal value q . However, our largest supercells are still too small to contain this range, except perhaps for the Ti_i^{1+} charged supercell.

2.3.2 Influence of defect charge distribution on choice of correction method

The intent of the Makov-Payne correction is to account for the artificial electrostatic interaction between the charged point defect images including the jellium background in the supercell because of the periodic boundary conditions [21]. Its first order correction is identical to Leslie and Gillan's result [42], which was applied to charged defects in TiO_2 in an earlier publication [20]. Examination of the charge localization range by the method of real-space charge integration in the previous section indicates that for the rutile TiO_2 the charge delocalization around the defect invalidates the application of the Makov-Payne correction. Furthermore, as pointed out by Castleton et al. [47], the DFT dielectric constant may not be the same as the experimental value because the dielectric constant is an intrinsically macroscopic quantity arising from an ensemble of ions; its application at this microscopic level is potentially problematic.

Promising new approaches have been very recently proposed by Freysoldt et al. [48] for correcting the electrostatic interactions between supercells that makes use of an analysis of electrostatics in dielectric media. However, here the simpler electrostatic potential alignment correction (ΔV correction) is adequate for our rutile TiO_2 system in that it converges the DFEs very quickly. The ΔV correction takes into account the fact that the valence band minimum (VBM) in the neighborhood of a charged defect is shifted with respect to the perfect crystal, which generates the energy used to exchange the electrons between VBM and the Fermi level. The value of the valence band shift is estimated by the difference between the average electrostatic potential at the edge of the

defective supercell and the perfect supercell [23, 24].

Figure 2.3 presents the DFEs for Ti_i^{4+} and V_{Ti}^{4-} as a function of supercell size with the two different corrections applied. The results indicate that the ΔV correction converges the total energies more rapidly with increasing supercell size than does the Makov-Payne correction. The corrected energies in Figure 2.3 do not include the chemical potential and Fermi level terms in eq (2.2), since these terms do not affect the convergence analysis. Table 2.2 lists the values for the different correction methods and the final DFEs for 2x2x3 and 3x3x5 supercells. It is clear that, even including both first and second order terms, the Makov-Payne correction scheme does not converge as quickly as the ΔV correction for this system. For these reasons the following results consider only the ΔV correction.

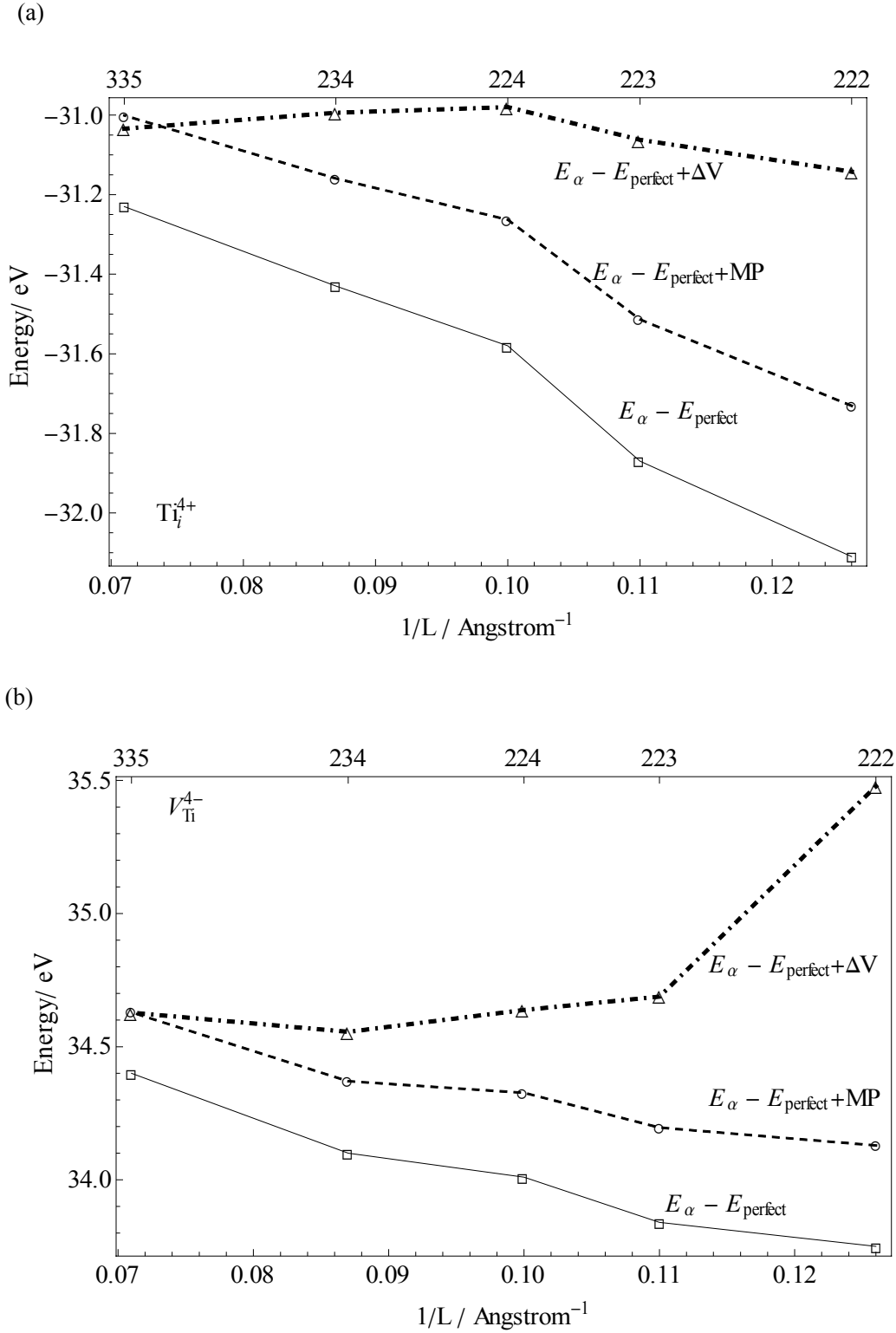


Fig 2.3. The energy of $E_\alpha - E_{\text{perfect}}$ (solid line) for Ti_i^{4+} (a) and $\text{V}_{\text{Ti}}^{4-}$ (b) after Makov-Payne correction (dashed line) and ΔV correction (dot-dashed line),

respectively, as a function of the supercell sizes.

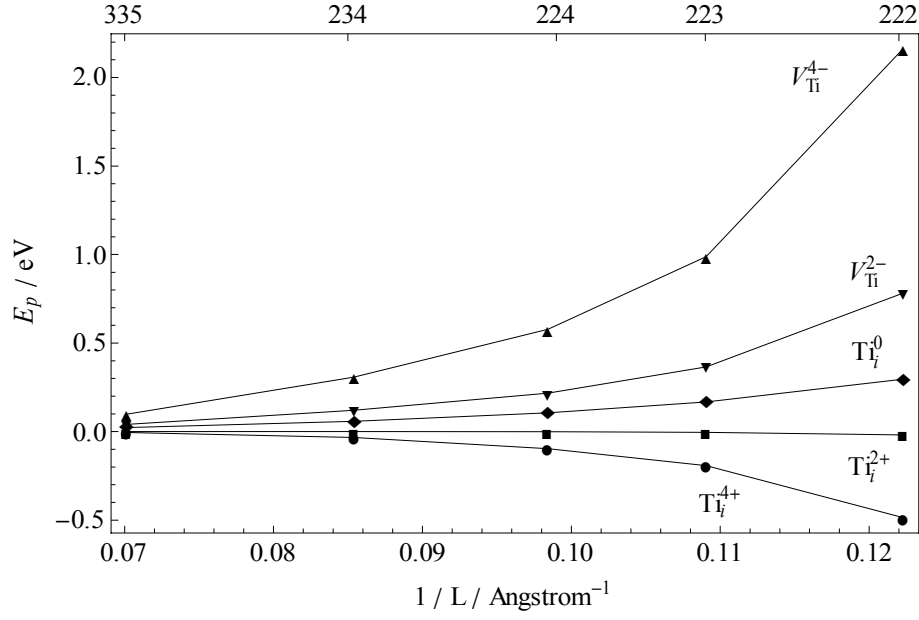
	ΔE	MP(1/L,q)	MP(1/L ³ ,q)	q* ΔV	$\Delta E + \text{MP}(1/L, 1/L^3, q)$	$\Delta E + q * \Delta V$
Ti ⁴⁺ _223	-31.87	0.251	0.099	0.808	-31.520	-31.062
Ti ⁴⁺ _335	-31.23	0.162	0.070	0.196	-30.998	-31.034
Ti ²⁺ _223	-20.78	0.063	0.019	0.454	-20.698	-20.326
Ti ²⁺ _335	-20.47	0.040	0.016	0.108	-20.414	-20.362
V _{Ti} ⁴⁻ _223	33.84	0.251	0.099	0.848	34.190	34.688
V _{Ti} ⁴⁻ _335	34.40	0.162	0.070	0.228	34.632	34.628
V _{Ti} ²⁻ _223	27.65	0.063	0.019	0.400	27.732	28.050
V _{Ti} ²⁻ _335	27.70	0.040	0.015	0.114	27.755	27.814

Table 2.2: DFE after different correction methods. The two MP(q) terms are the Makov-Payne 1st and 2nd order corrections by defining the point charges with different radii around the defects between 0.7 to 2 Å.

2.3.3 Artificial elastic energy interaction

Although the correction methods mentioned above are widely used to correct for artificial electrostatic effects associated with the small system sizes, none explicitly includes a correction for the possible artificial elastic energy interactions inherent in the supercell approach. One possible scheme to account for this effect is to allow the supercell volume to relax in the DFT calculations such that the external pressure on the supercell after relaxation is close to zero; this simulates a physical scenario in which the physical defect concentration is the same as the (extremely high) defect concentration in the supercell. Another approach that is usually considered to be more appropriate for the dilute solution approximation, which is of interest here, is to fix the supercell volume at the relaxed volume of the pure cell during the relaxation, such that the elastic strain field interacts with the boundary of the supercell and leaves an external pressure on the relaxed supercell.

(a)



(b)

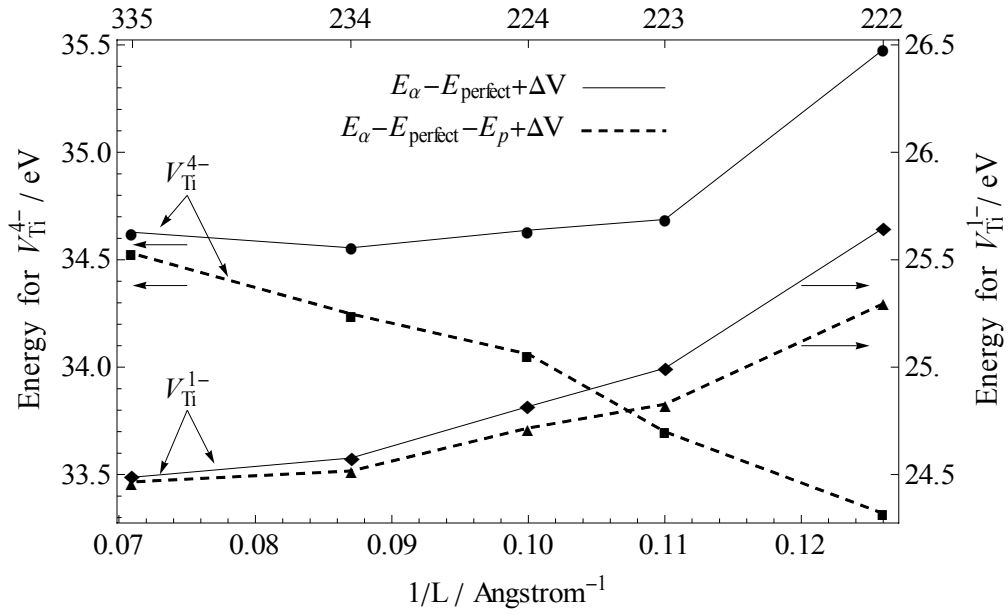


Fig 2.4. (a) The elastic strain energies calculated from the external pressures on the constant volume supercells as a function supercell sizes, using formula $E_p = \frac{P}{|P|} \frac{1}{2} \frac{VP^2}{Y}$ (b) The comparison of the convergence between the constant volume ($E_\alpha - E_{perfect}$) and zero pressure method ($E_\alpha - E_{perfect} - |E_p|$) after ΔV correction for V_{Ti}^{4-} and V_{Ti}^{1-} supercells.

The pressure on the supercells in the constant-volume method can be used to estimate its energy difference E_p from the corresponding zero pressure supercell by the classical formula of elastic strain energy $\frac{1}{2} \frac{VP^2}{Y}$, where V is the volume of the supercell, P is the external pressure on the supercell using the constant volume method from DFT calculation and Y the experimental bulk modulus of bulk rutile TiO_2 [49]. The calculated energy difference as a function of supercell size for five different defective supercells is shown in Figure 2.4(a). These values agree reasonably well with the energy differences taken directly from the DFT-calculated, zero-pressure supercell energies for several tested cases. The figure illustrates that the energy difference can be very large at small supercells: ~ 1 eV for the $2 \times 2 \times 3$ V_{Ti}^{4-} supercell, while at $3 \times 3 \times 5$ supercells the difference is ~ 0.1 eV. We can compare the convergence behavior of the two supercell boundary conditions by firstly calculating the DFEs in the constant volume approach, followed with the subtraction of the elastic strain energy term E_p to get the DFEs in the zero

pressure approach. We find that the constant-volume method converges more quickly than the zero-pressure method for highly charged supercells, i.e. Ti_i^{4+} , Ti_i^{3+} , $\text{V}_{\text{Ti}}^{4-}$, $\text{V}_{\text{Ti}}^{3-}$ and V_{O}^{2+} . For intermediately charged supercells, i.e. Ti_i^{2+} , $\text{V}_{\text{Ti}}^{2-}$ and V_{O}^{1+} , both methods have very similar convergence behaviors, while for the supercells with low charge states, i.e. Ti_i^{1+} , Ti_i^0 , $\text{V}_{\text{Ti}}^{1-}$, V_{Ti}^0 and V_{O}^0 , the zero-pressure method converges more quickly. Figure 2.4(b) shows the case for $\text{V}_{\text{Ti}}^{4-}$ and $\text{V}_{\text{Ti}}^{1-}$ to illustrate some of these trends. Although the convergence speed of the two methods varies with the charge state of the supercell, the differences are always within 0.1 eV for the 3x3x5 supercells as shown in Figure 2.4(a). Thus we use the constant volume method with 3x3x5 supercells for all the subsequent calculations.

2.4 Defect Energetics

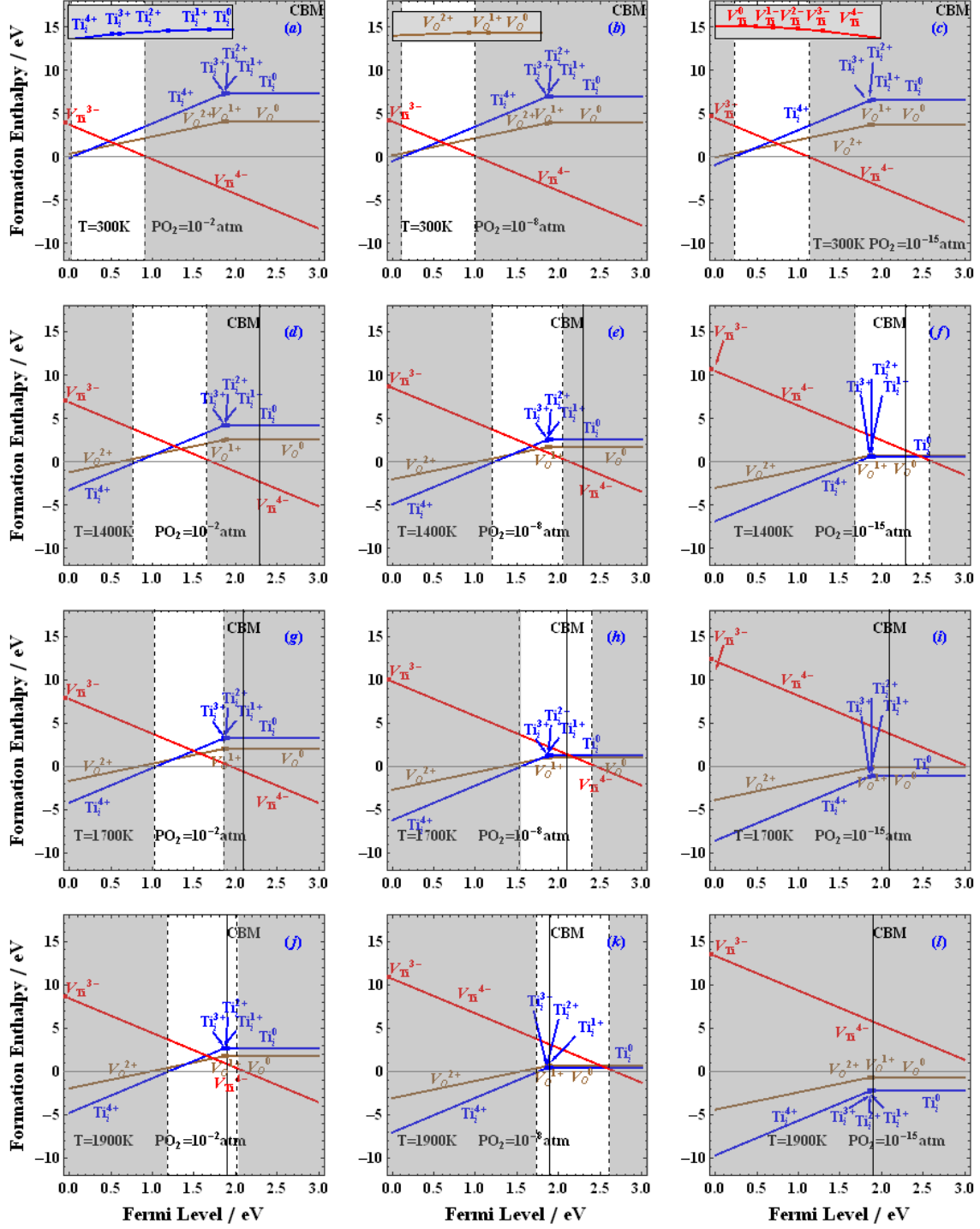


Fig 2.5. DFE as a function of E_f at different temperature and PO_2 . The gray areas are forbidden by the

charge neutrality condition. CBM is labeled for its experimental values at different temperatures, at 300K it is at 3eV. The insets in plots (a-c) enlarge the transition regions for each type of defect, respectively, which shows that the transition levels are ordered. The transition regions of titanium vacancies are cut by the zero value of Fermi level or the valance band maximum, thus most of them are not seen except for V_{Ti}^{3-} and V_{Ti}^{4-} .

Based on the computational approached discussed above, the defect formation energies as a function of the temperature, oxygen partial pressure and Fermi level calculated by eq (2.2) for the supercell size of 3x3x5 are presented in Figure 2.5. The calculated DFE of 3.6 eV for the fully charged Frenkel pair (Ti_i^{4+} and V_{Ti}^{4-}) is ~ 0.8 eV lower than the experimentally derived values of 4.4 eV at ~ 1500 K [6]. Part of this difference might be due to intrinsic errors in the DFT/GGA approach or the exclusion of the vibrational free energy, which was estimated by molecular dynamic calculations to account for around 5% of the DFE at 700K in a Schottky defective supercell [20]. These temperature dependant effects will be discussed in detail in chapter 3 and 4 by computationally expensive phonon calculations, while in this chapter only the DFEs calculated from eq (2.2) are considered. Table 2.3 lists the DFEs of Frenkel pairs and Schottky defects calculated by summing the DFEs of single defects, as well as their comparison with the experimental values [6, 10]. It indicates that the fully charged pairs are most favorable energetically and have energies closest to the experimental values.

$Ti_i^{q+} + V_{Ti}^{q-}$	$DFE_{dv}^{Frenkel}/eV$	$DFE_{Exp}^{Frenkel}/eV$	$V_{Ti}^{2q-} + 2V_O^{q+}$	$DFE_{dv}^{Schottky}/eV$	$DFE_{Exp}^{Schottky}/eV$
q=4	3.594	4.4~4.7	q=2	4.43	≤ 6.6
q=3	5.494	and ≤ 5.0	q=1	8.28	for q=2
q=2	7.452	for q=4	q=0	12.42	
q=1	9.491				
q=0	11.59				

Table 2.3. The DFE of differently charged Frenkel and Schottky pairs compared with experimental values. The calculated pair energies are the direct summation of the individual DFEs calculated using eq (2.2) thus does not include the association energy between the individual defects, which agrees with the experimental condition of dilute solution in ref [2, 6, 9, 10].

By fixing T and PO_2 , the DFEs as a function of Fermi level can be considered, as illustrated in Figure 2.5, where the Fermi level is referenced relative to the VBM. The fully charged defects at nearly all T and PO_2 combinations are more likely to occur, while the partially charged defects are rarely preferred. However, there is a sharp transition from the fully charged defects to the neutral defects at around 1.9 eV for the titanium interstitial and the oxygen vacancy, where all the defect transition levels shrink to a very narrow energy range, as shown in Table 2.4. The close total energy differences between any two supercells with successive charge states are a result of the fact that the differences in the charge distributions of the supercells are similar. In addition, when one electron is added to a Ti_i^{q-1} supercell to form a Ti_i^q supercell, the way that the added

charge density distributes is insensitive to the original charge state, $q-1$. There is no direct evidence of switching of orders or the so-called negative-U effect [50] as the charge state varies.

$[\alpha]^q$	E_α/eV	$E_\alpha^{q-1}-E_\alpha^q/\text{eV}$	$E_\alpha^{q-1}-E_\alpha^q-E_{\text{vbm}}-\Delta V/\text{eV}$
Ti_i^{4+}	-2456.23	5.38	1.854
Ti_i^{3+}	-2450.85	5.38	1.858
Ti_i^{2+}	-2445.47	5.42	1.885
Ti_i^{1+}	-2440.05	5.44	1.907
Ti_i^0	-2434.61		

Table 2.4. Total energy differences between successive charge states of titanium interstitial defective supercells show the equal energy difference phenomenon.

Further examination of Figure 2.5 reveals that regions where the dominant point defect has a negative DFE (the gray areas in the figure) are forbidden regions for pure rutile TiO_{2-x} bulk material. This is because the P_{O_2} , T and Fermi level are not independent variables, but are constrained by the electroneutrality condition. At any given T and P_{O_2} , if the Fermi level were to be in the forbidden region, then the formation of a large concentration of the defect would change the Fermi level of the material drastically, which would then drag the Fermi level back to the allowed regions of Figure 2.5. It is important to note that this does not strictly apply to a doped material in which the Fermi energy can be adjusted by a suitable choice of dopant, but rather to the intrinsic regime in which the Fermi energy in principle, must be self-consistently determined by the intrinsic point defects that are in equilibrium at the given P_{O_2} and T .

Examination of Figure 2.5 reveals several important trends. First, at high temperature and low PO_2 , such as in Figure 2.5(f), the allowed region for the Fermi level is close to the conduction band minimum (CBM), implying the stabilization of n-type TiO_2 . By contrast, at low T and high PO_2 , such as in Figure 2.5(a), the allowed region for the Fermi level is closer to the VBM, implying the stabilization of p-type TiO_2 . Additionally, Figures 2.5(i) and (l) correspond to a combination of T and PO_2 for which rutile TiO_2 is not stable because all the dominant point defects have negative formation energies for all possible Fermi levels within the band gap; thus the forbidden region extends across the entire band gap. This prediction is consistent with the experimental findings that at high T and low PO_2 of the combination illustrated in Figure 2.5(i) rutile transforms into two-dimensional Magneli defect phases [1, 51]. Thus, in general, increasing T or decreasing PO_2 will move the allowed region of the Fermi levels toward the CBM, while decreasing T or increasing PO_2 has the opposite effect. Considering the experimental finding that at around 1700K Ti_i^{4+} is dominant [1, 5], one can conclude from Figure 2.5(g) that the Fermi level in the allowed region is slightly above 1 eV, while in Figure 2.5(h) it is slightly above 1.5 eV. Taking into account the experimental CBM [6] it is clear that n-type TiO_2 is predicted to be stable under these conditions.

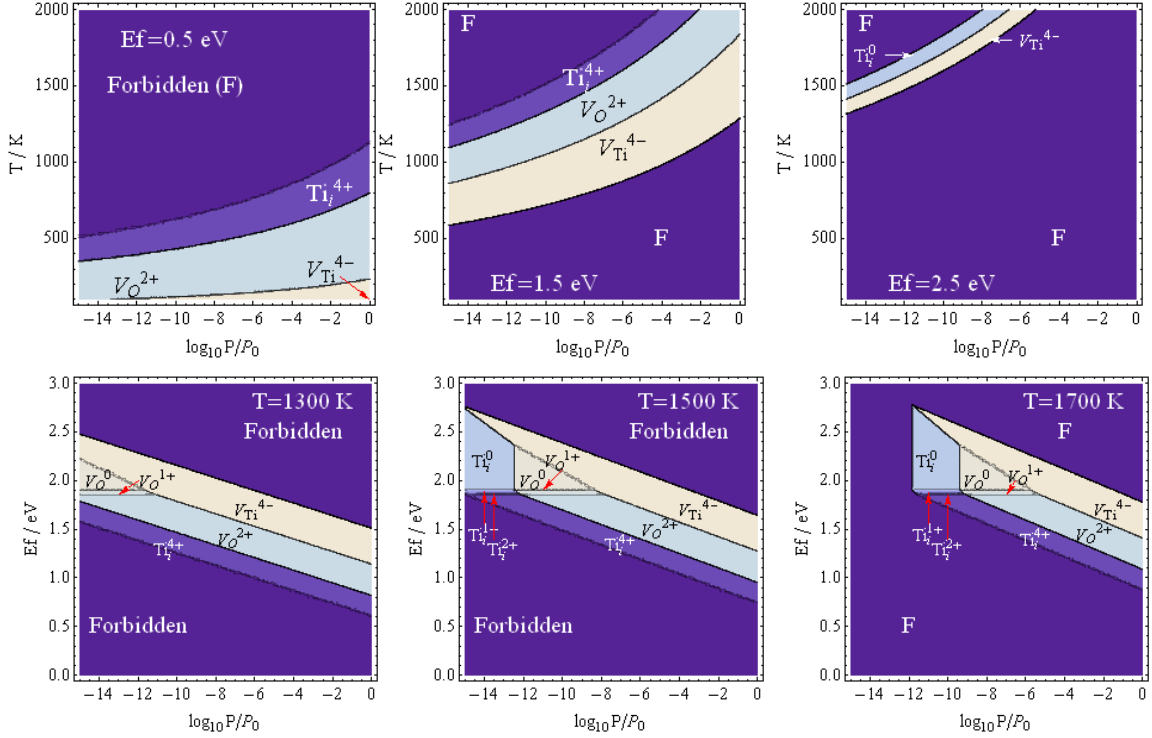


Fig 2.6. Dominant point defect distribution in the 2D phase space .

It is also natural to plot the two-dimensional dominant defect phase diagrams in the PO_2 - T or the E_F - PO_2 phase spaces, as illustrated in Figure 2.6. In the allowed regions the fully charged defects always occupy the largest phase space. In chapter 3 and 4 it will be shown that it is caused by the neglect of the temperature dependent effects in eq (2.2) simplified from eq (2.1). Another evident trend is that when the Fermi level moves from the VBM to CBM the corresponding temperature of the allowed regions in these 2D phase diagrams increases and the stability range becomes narrower.

It is important to note that these results are quantitatively and sometimes qualitatively different to those in a previous publication [20]. Most notably, with the improved ΔV correction scheme, the fully charged defects dominate over a significantly larger phase

space. Thus, as discussed in Section 2.3.2, the $2 \times 2 \times 3$ supercells with the Leslie-Gillan or Makov-Payne correction in ref [20] were not adequately converged.

As a final point, it should be emphasized that the point defect formations energies presented here are in the dilute solution approximation and do not account for any defect associations, which may certainly occur in real systems. Defect associations would be expected to change the formation energies of the defect pairs depending on different conditions.

Chapter 3

Charged Point Defect related Phonon Free Energy Calculations

3.1 Harmonic Calculation of Phonon Free Energy

The linear response approach[52, 53] or frozen phonon method[54-58] is widely used for the DFT based phonon calculation in the pure structures. In the former approach the dynamic matrix is calculated in a self-consistent way through the second derivative of energy to the atom displacements by the perturbation theory. While the latter approach, also called small displacement method, is more straightforward, with the force constants computed from the Hellmann-Feynman forces arising from the small displacements of all the atoms limited by symmetry in the supercell. Although the phonon calculations were widely performed for pure structures[52-58], the calculation of point defect related phonon behavior is very limited, with almost all the previous works focused on the

neutral defects in metals[59-61] or simple substances[62, 63], except for work on charged gallium vacancies in GaAs[64]. In the GaAs work, it was shown that different charge states of V_{Ga} can influence the temperature dependences of phonon free energies calculated from the harmonic approximation. However, this effect was largely neglected for the DFE calculation of charged point defects in oxides [11-16], based on the assumption that the temperature dependant phonon free energies in the defective and pure structures are identical and thus cancel. It will be shown in this chapter that this assumption fails at high temperatures for rutile TiO_2 from the calculation of the temperature dependent phonon free energies with the harmonic approximation [65], $F_{ph}^{harmonic}$, for both defective and pure supercells at the fixed volume of relaxed pure rutile. The thermal expansion effect with in the quasi-harmonic approximation will be studied in Chapter 4.

The frozen phonon method is used in this chapter for the phonon calculation with *fropho*[66] and VASP. The essential part of the calculation is the construction of the force constant matrix, whose matrix element $\Phi(i, j)$ is the derivative of the force on atom i with respect to the displacement of atom j [65]. The quantities directly calculated from DFT are forces introduced by the small displacement of each atom in the supercell. In this work VASP was used to implement all DFT calculations. The energy convergence criteria in VASP was set to 10^{-8} eV and the force convergence criteria set to 10^{-5} eV/Å for the supercell at equilibrium without displacement. For each displaced supercells the energy convergence criteria was set to 10^{-8} eV. A k-mesh of 4x4x4 is used for all

supercells, with the cutoff energy set to 500eV. The projection operators were evaluated in the reciprocal space for precise force calculation. The total number of necessary displacements is limited by the symmetry of the structure; for the rutile structure with space group $4_2/mnm$ only three displacements are needed. However, if a titanium interstitial or oxygen vacancy is introduced into a supercell consisting of $2 \times 2 \times 3$ unit cells the necessary displacements increase to 122 or 236, respectively, since the symmetry of the structure is decreased by the introduction of the defect ion. To ensure precise force calculation, each displacement is done for both positive and negative directions. Once the necessary displacements and resulting forces have been calculated, the force constant matrix of the structure can be constructed. The dynamical matrix element is then calculated from the sum of force constants multiplied by the phase factor over all unit cells in the supercell. The phase factor is the vector product of the phonon wave vector q and a vector between any two atoms of interest. Thus a corresponding dynamical matrix can be formed from the force constant matrix. Possible phonon modes, or frequencies, in a structure are given by the eigenvalues of the dynamical matrix. For rutile, there are 18 different modes corresponding to the 18 degrees of freedom in the unit cell. Among these phonon modes three are acoustic and fifteen are optical. Thermodynamic properties can be calculated from the phonon spectra, which includes the phonon frequencies $\omega(q, \nu)$ of all the possible modes ν at each q -point on a q mesh, by the basic formula describing phonon free energy in statistical thermodynamics[67-69]:

$$\begin{aligned}
F_{ph}^{harmonic} &= -k_B T \ln Z \\
&= \frac{1}{2} \sum_{q,\nu} \hbar \omega(q,\nu) + k_B T \sum_{q,\nu} \ln[1 - \exp(-\hbar \omega(q,\nu) / k_B T)]
\end{aligned} \tag{3.1}$$

where the summation is over all q-points in the reciprocal space and all the phonon modes ν .

3.2 Phonons in Pure Rutile TiO₂

The 15 optical phonon modes at the Gamma point based on DFT calculation are shown in Table 3.1. These calculations were performed with four different exchange-correlation functionals: LDA (Ti: 3d²4s² explicitly treated), LDA (Ti: 3p⁶3d²4s²), PBE (Ti: 3d²4s²) and PBE (Ti: 3s²3p⁶3d²4s²). In each case the same electrons were explicitly treated for oxygen (O: 2s²2p⁴.) Comparing the calculated frequencies in Table 3.1 to the experimental results shows that the LDA functional more accurately describes the vibrational properties of rutile TiO₂ than the gradient corrected functionals, which agrees with the conclusions of a previous work on pure rutile TiO₂[70]. The small core pseudopotential LDA (Ti: 3p⁶3d²4s²), which is computationally more expensive, is not necessarily more accurate than the large core pseudopotential LDA (Ti: 3d²4s².) Thus, the large core pseudopotential LDA (Ti: 3d²4s²) was chosen for all phonon calculations in subsequent calculations.

	LDA Ti3d	LDA Ti3p	PBE Ti3d	PBE Ti3s	Exp Optical	Exp Neutron
B1u	3.60993	3.84824	2.38051	0.0361576	–	3.39
B1g	4.1302	4.16949	2.46883	1.62142	4.29	4.25
Eu	5.155	5.31832	2.85436	2.4146	5.49	5.66
Eu	5.155	5.31832	2.85436	2.4146	5.49	5.66
A2u	5.2486	5.50109	4.38351	4.47904	5.01	5.18
Eu	11.789	11.7207	10.7057	10.7133	11.64	–
Eu	11.789	11.7207	10.7057	10.7133	11.64	–
B1u	12.462	12.2438	10.9774	10.7903	–	12.18
A2g	12.6931	12.7416	12.3226	12.5106	–	–
Eg	13.9579	14.2645	13.0836	12.8896	13.41	13.34
Eg	13.9579	14.2645	13.0836	12.8896	13.41	13.34
Eu	15.0814	14.7416	14.3669	14.1134	15.	14.81
Eu	15.0814	14.7416	14.3669	14.1134	15.	14.81
A1g	18.3558	18.6846	17.3028	17.0734	18.36	18.3
B2g	24.3405	24.5986	23.4372	23.082	24.78	24.72

Table 3.1 Calculated optical phonon frequencies at Gamma point (THz) from different exchange correlation potentials and different explicitly treated electrons, compared with experimental data from optical[71, 72] or neutron[73] scattering measurements.

The calculated phonon dispersion curve was compared with neutron inelastic scattering[73] data, as shown in Figure 3.1. Good agreement was observed, which also supports the previous selection of the large core pseudopotential LDA exchange-correlation functional. The phonon spectrum or density of states (DOS) with a certain q-mesh can also be calculated, as shown in Figure 3.2, in good agreement with the neutron inelastic scattering measurement[73]. The heavy Ti ions contribute mostly to the low frequency part of DOS, while the light O ions contribute to high frequency part above 5 THz. Comparing Figure 3.1, Figure 3.2 and Table 3.1 shows the peak at 3 THz

corresponds to TA phonons, the strong peak at 14 THz are from LO phonons, the peak at 16 and 21.5 THz correspond to TO phonons, in agreement with the previous calculation on pure rutile TiO_2 [58] and experiments[71-73].

From the spectrum of phonon DOS the phonon free energy can be calculated with the harmonic approximation from eq (3.1) to be compared with the experimental chemical potential, as shown in Figure 3.3. Strictly speaking, the experimental chemical potential, or molar Gibbs free energy, also includes the effect of thermal expansion, which increases the internal energy and decreases the phonon free energy of the pure rutile. It will be discussed in chapter 4 that the good agreement in Figure 3.3 is simply a reflection of the fact that the two neglected effects related to thermal expansion happen to almost cancel each other, which makes the harmonic calculation a good approximation for pure rutile TiO_2 . It will be shown in Chapter 4 that the thermal expansion related effects can influence the calculated DFE in a non-trivial way. But in this chapter only the harmonic approximation is used in all the following calculations.

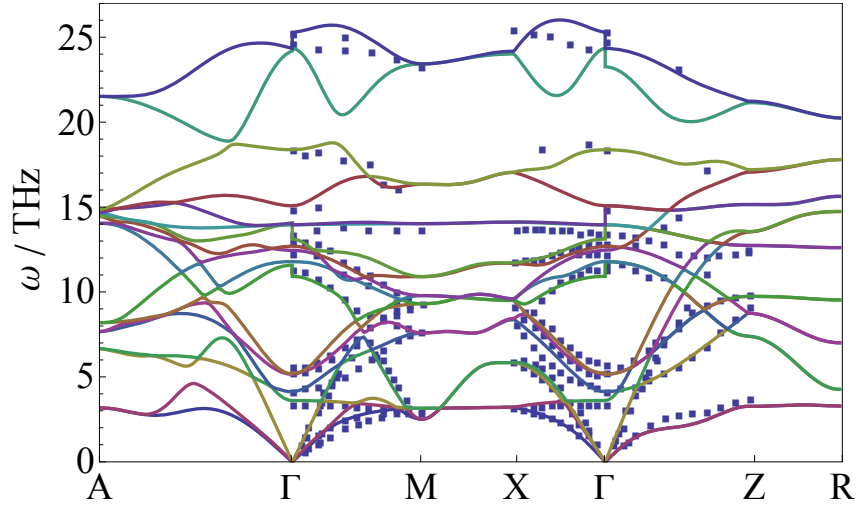


Figure 3.1 Calculated Phonon dispersion curves for pure rutile TiO_2 compared with the neutron inelastic scattering experiments [73].

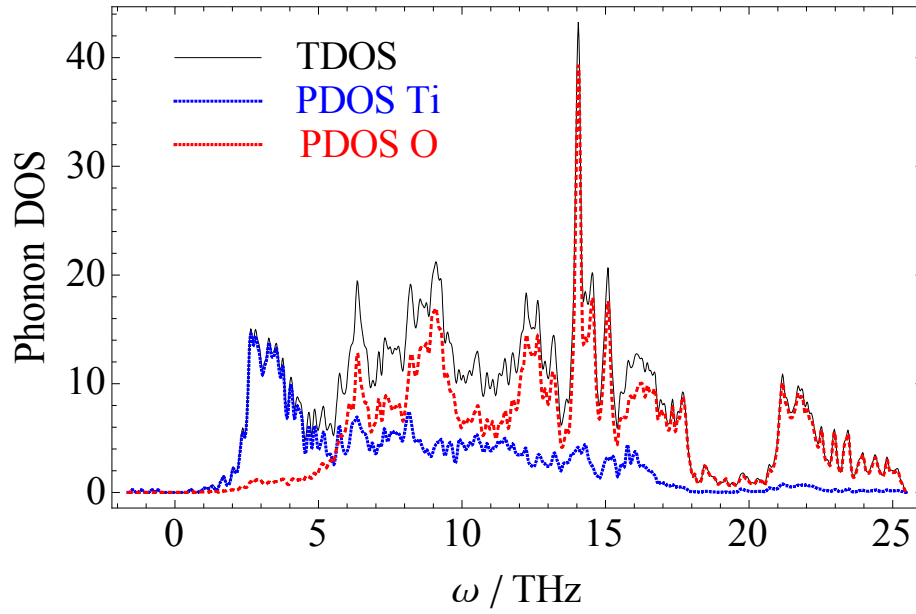


Figure 3.2 Phonon Density of States (DOS) for pure rutile at the q-mesh of 8x8x8. The total DOS (TDOS) can be further decomposed into partial DOS (PDOS) of Ti and O, respectively.

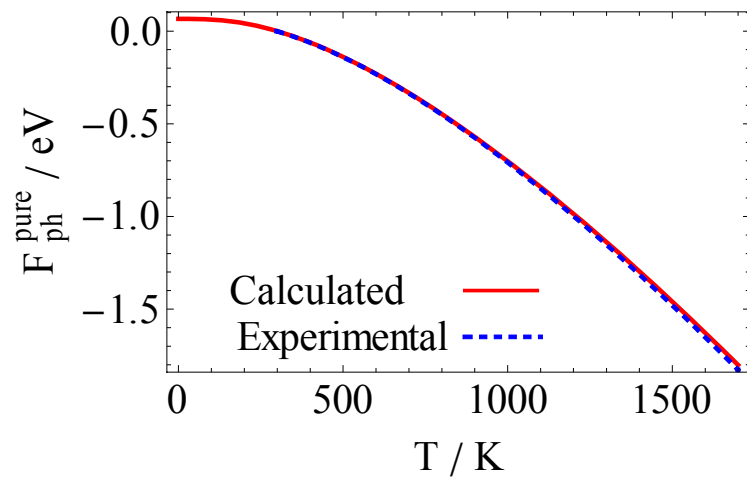


Figure 3.3 Calculated phonon free energy for pure rutile TiO_2 compared with the experimental data from NIST database[31].

3.3 Phonons in Defective Supercells

Phonon DOS of differently charged Ti_i^q defective supercells are shown in Figure 3.4. From the comparison from Figure 3.4 (a) to (c) it can be observed the peaks of negative frequencies are strongly influenced by the charge state of the supercells. In neutral Ti_i^0 and low charge state Ti_i^{1+} supercells, the phonon DOS is free of negative frequencies, while in highly charged Ti_i^{2+} , Ti_i^{3+} and Ti_i^{4+} supercells, the peaks of negative frequencies are strengthened by increasing charge state of the supercell. Further study of their phonon dispersion curves show these negative frequencies are only contributed from the three acoustic phonon modes at non-Gamma points, while at the Gamma point the frequencies are always zero as expected. In order to indentify whether it is caused by the artificial electrostatic interaction in the limited supercell size of $2 \times 2 \times 3$, the phonon DOS in a $3 \times 3 \times 5$ sized Ti_i^{4+} defective supercell is calculated, which takes 1000 dedicated CPUs to finish within 30 days. Since the total number of phonon modes is proportional to the number of atoms in the supercell, all the peaks are magnified by this proportionality in $3 \times 3 \times 5$ sized supercell compared to $2 \times 2 \times 3$ sized supercell, except the peak of negative frequencies, as shown in Figure 3.4(d). Thus, the invariable strength of this peak indicates it is not influenced by the increasing size of the supercell and is not caused by the artificial electrostatic interaction. Similar trend is found in charged V_O supercells as shown in Figure 3.5(b), while Figure 3.5(a) shows most V_Ti supercells are free of negative frequencies, except the V_Ti^{4+} supercell with a slight amount of negative

frequencies. Further study of the energy profile versus displacement of these acoustic modes suggests the calculated acoustic phonon frequencies at non-Gamma points are not precise enough, since technically treating the defective supercells as new 1x1x1 sized unit structures in the frozen phonon calculation only guarantees the calculated frequencies at the Gamma point.

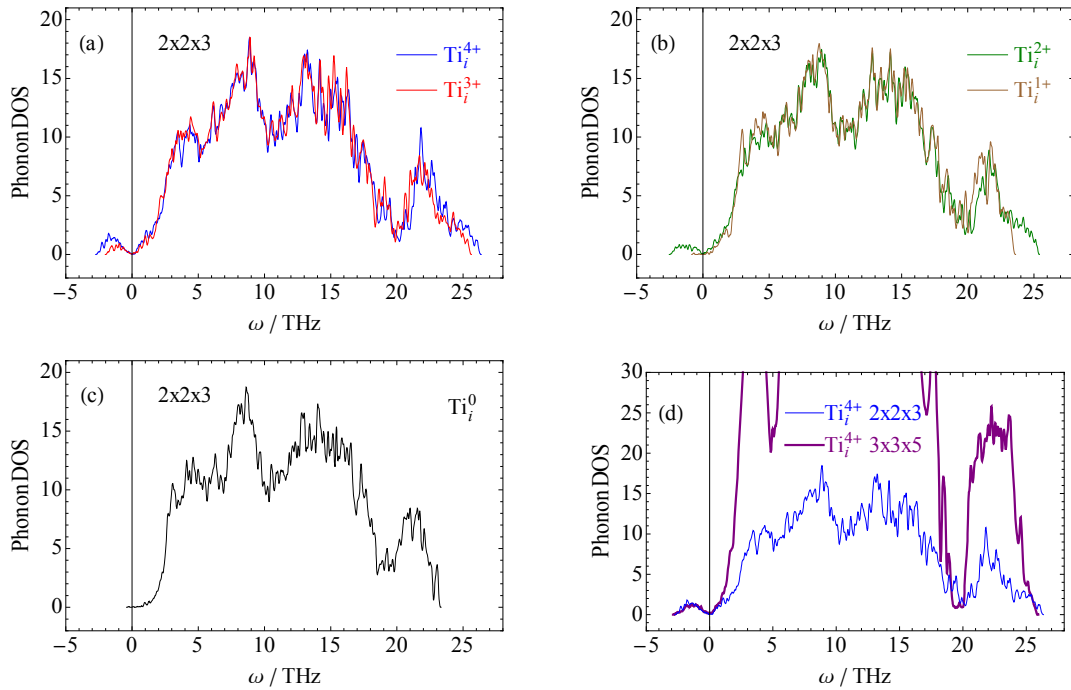


Figure 3.4 Phonon DOS of differently charged Ti interstitial defective supercells for (a) Ti_i^{4+} and Ti_i^{3+} at $2 \times 2 \times 3$ sized supercells, (b) Ti_i^{2+} and Ti_i^{1+} at $2 \times 2 \times 3$ sized supercells, (c) Ti_i^0 at $2 \times 2 \times 3$ sized supercells (d) Ti_i^{4+} at $2 \times 2 \times 3$ sized and $3 \times 3 \times 5$ sized supercells

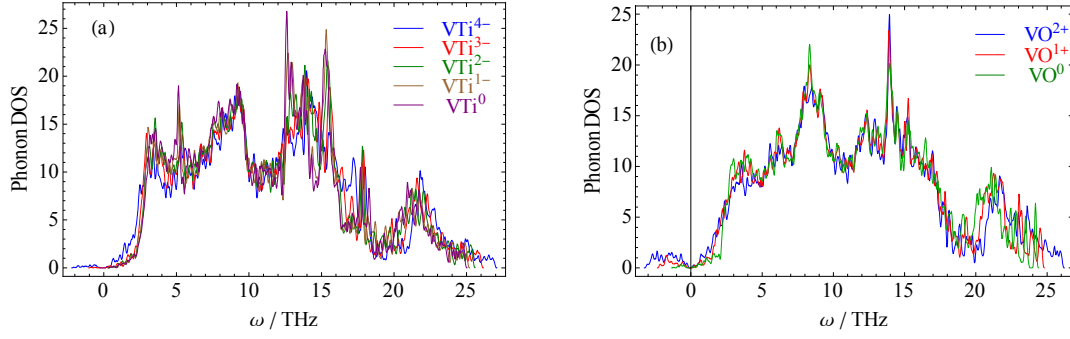


Figure 3.5 Phonon DOS of differently charged (a) VTi^q supercells and (b) VO^q supercells at the supercell size of $2 \times 2 \times 3$.

Since only the three acoustic phonon modes contribute to the negative frequencies in the phonon DOS of defective supercells, the entire three acoustic modes were excluded from the calculation of the following phonon free energy differences to minimize the numerical error in the comparison. The exclusion of the acoustic phonon modes does not introduce any meaningful error in calculating the energy differences from a methodological point of view since, in principle, the three acoustic modes should be very similar among different supercells of a same material, including defective and pure cells, within the dilute solution approximation for the defects; while the optical phonon modes describe the most significant energy differences between these various structures[65, 74].

Phonon free energies of defective supercells and their energy differences from the pure rutile can then be calculated from the phonon DOS with the harmonic approximation. Results from these calculations are shown in Figure 3.6 for titanium interstitials, in Figure 3.7 for titanium vacancies and in Figure 3.8 for oxygen vacancies.

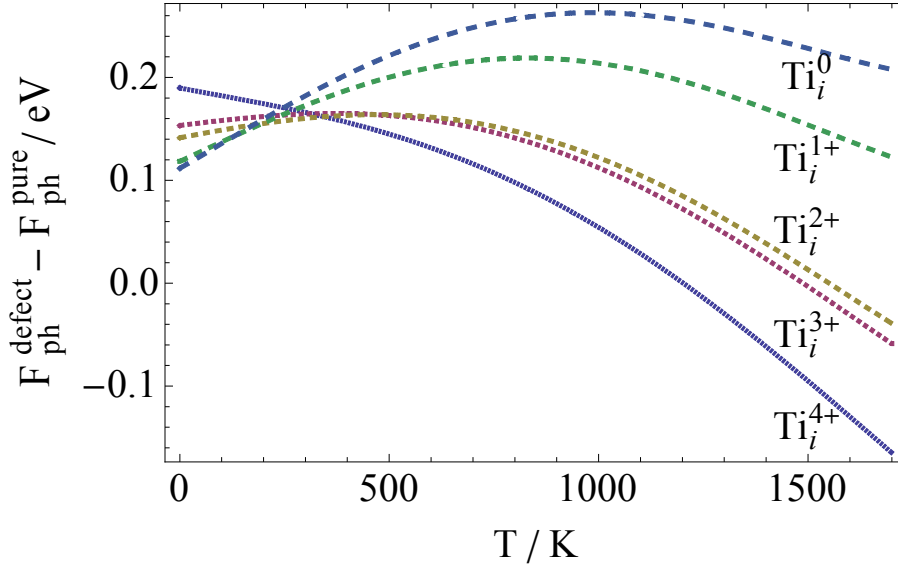


Figure 3.6 Phonon free energy difference from all optical phonon modes between a 2x2x3 supercell with a Ti_i^{q+} defect and the perfect structure as a function of temperature.

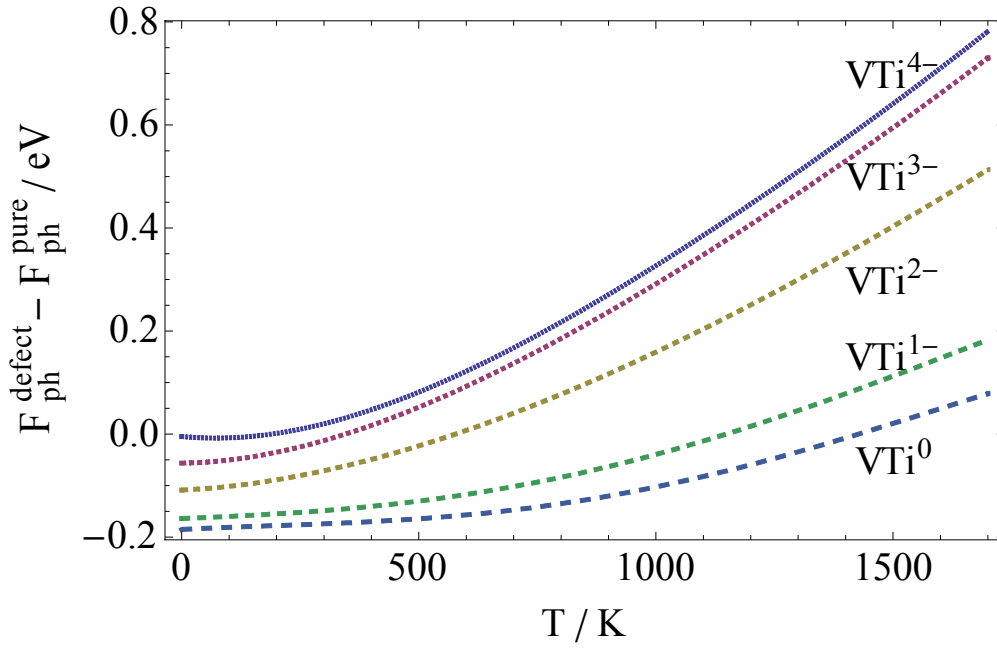


Figure 3.7 Phonon free energy difference from all optical phonon modes between a 2x2x3 supercell with a $\text{V}_{\text{Ti}}^{q-}$ defect and the perfect structure as a function of temperature.

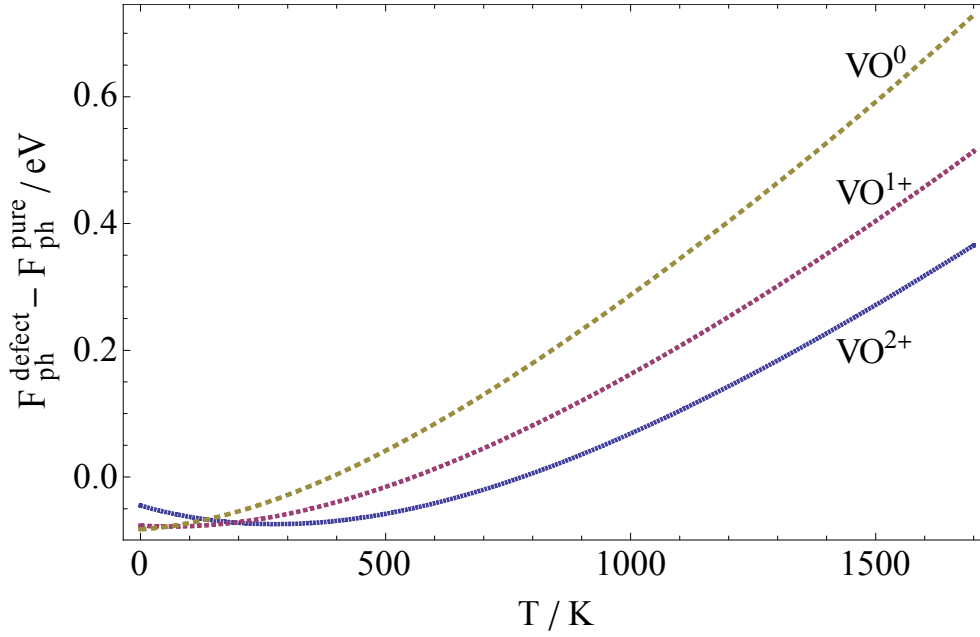


Figure 3.8 Phonon free energy difference from all optical phonon modes between a 2x2x3 supercell with a $\text{V}_\text{O}^{\text{q}+}$ defect and the perfect structure as a function of temperature.

Figures 3.6, 3.7 and 3.8 show fully charged Ti interstitial and O vacancy are stabilized by $F_{\text{ph}}^{\text{harmonic}}$ at high T, while partially charged Ti vacancies are more stabilized by $F_{\text{ph}}^{\text{harmonic}}$ at high T. Since the most possible dominant defects in rutile are Ti_i^{4+} , Ti_i^{3+} , V_Ti^{4-} , V_Ti^{3-} , V_O^{2+} and V_O^{1+} , the following discussion will be focused on the phonon free energy of these defects.

3.3.1 Phonons in Ti interstitial defective supercells

For 2x2x3 sized Ti interstitial defective supercell there are 213 optical phonon modes spreading from 0 THz up to around 25 THz. However, only those modes with relatively low frequencies contribute significantly to the phonon free energy at high T, as can be seen from eq (3.1). The differences between phonon frequencies of the two defect structures at the Gamma point for each phonon mode up to 12 THz (lowest 120 optical phonon modes) are shown in Figure 3.9. The first optical phonon mode, ω_{lst}^O , has the largest difference. And in general the phonon frequencies are lower in the supercell with the Ti_i^{4+} defect.

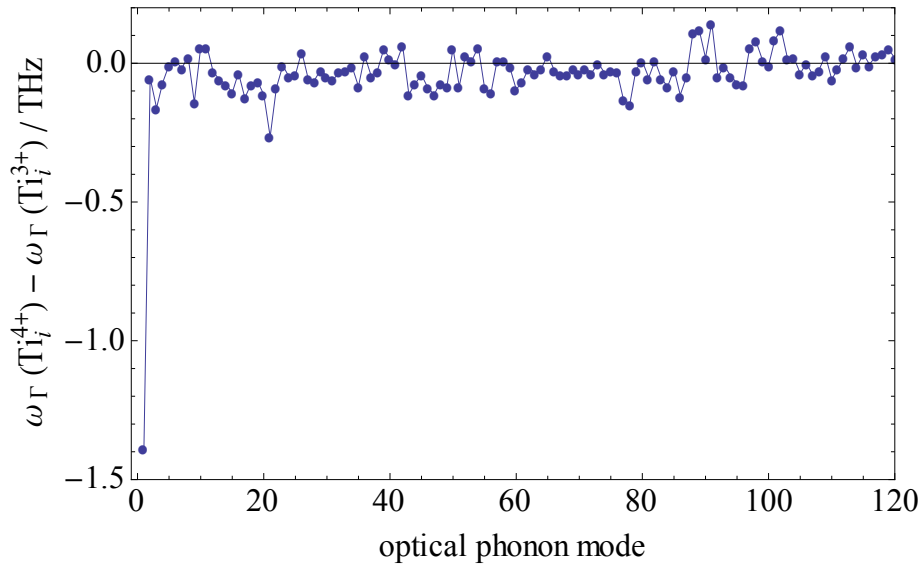


Figure 3.9 Optical phonon frequency differences at the Gamma point for the lowest

120 modes between Ti_i^{4+} and Ti_i^{3+} defect structures in a 2x2x3 supercells.

Phonon dispersion curves of the lowest 120 optical modes for the two defective supercells, shown in Figure 3.10, shows ω_{1st}^O is lower for Ti_i^{4+} in all symmetry directions. This softest mode of the Ti_i^{4+} defect structure, as well as the contribution from all other modes, makes its phonon free energy much lower at high T than the energy of the Ti_i^{3+} defect structure. If this mode is excluded in the phonon free energy calculation, as shown in Figure 3.11, the energy difference between the two structures can be reduced by more than 80% at high T as compared with the case where it is included (Figure 3.6) This trend is clear when the phonon free energy difference between the Ti_i^{4+} and Ti_i^{3+} structures is shown with and without the contribution from ω_{1st}^O as shown in Figure 3.12. Thus the following discussion will be focused on the specific type of the oscillation, shown in Figure 3.13, associated with this phonon mode of the Ti_i^{4+} interstitial defect structure.

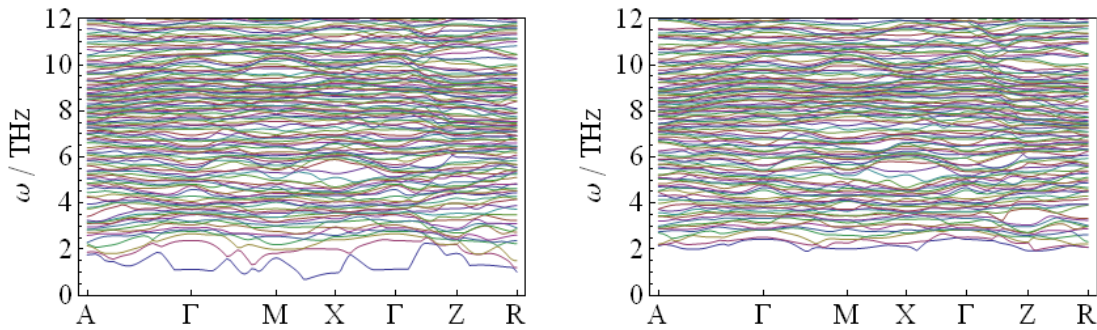


Figure 3.10 Phonon dispersion curves of Ti_i^{4+} (left) and Ti_i^{3+} (right) for the lowest 120 optical modes.

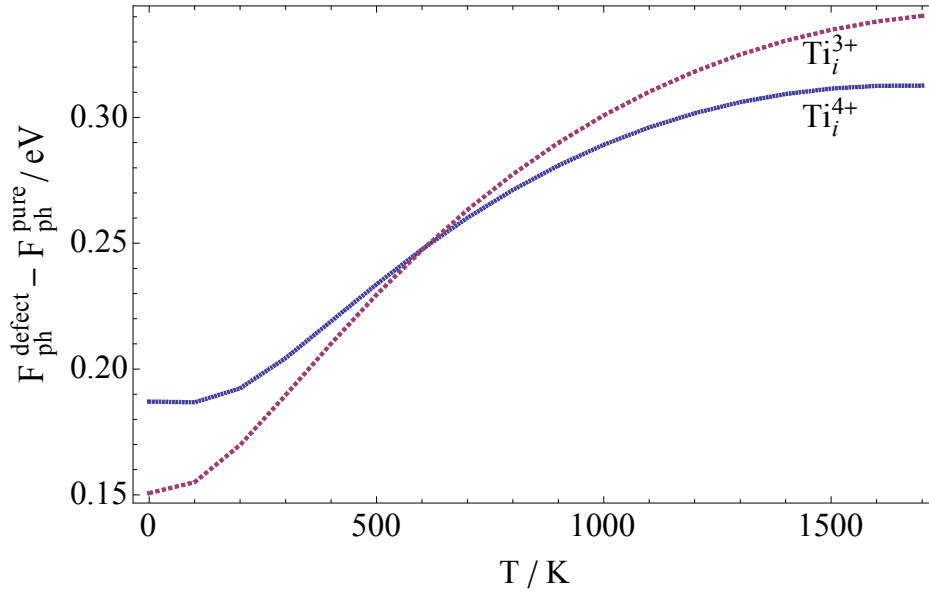


Figure 3.11 Phonon free energy difference from all the optical phonon modes except for the lowest one between $\text{Ti}_i^{\text{q}+}$ defective 2x2x3 supercells and the perfect structure as a function of temperature.

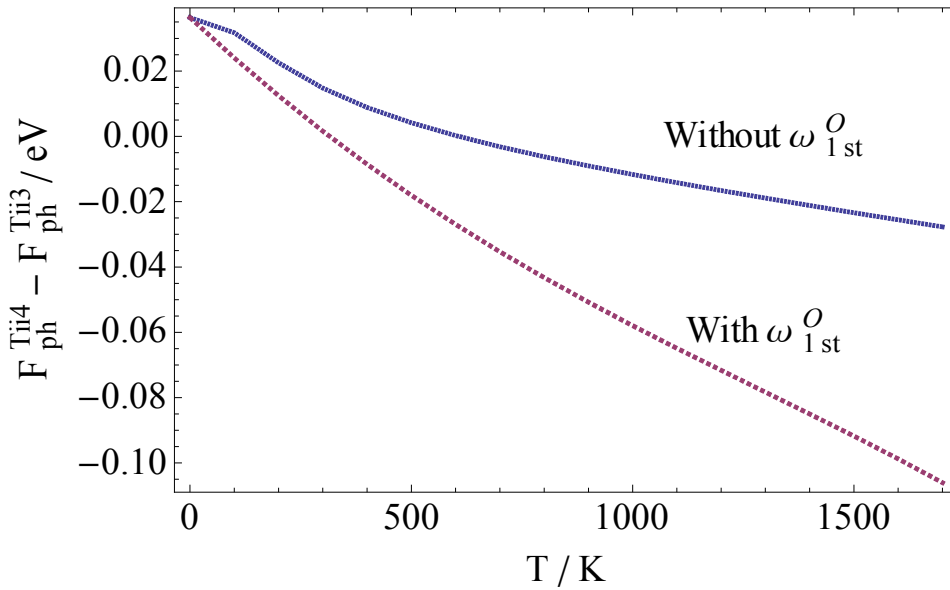


Figure 3.12 Phonon free energy difference between Ti_i^{4+} and Ti_i^{3+} structures with and

without the 1st optical phonon mode.

Figure 3.13 shows this oscillation mode is unique to Ti interstitial defective supercells. The oscillations of the ions involved in this mode are centered around, and strongly correlated with the movement of the defect ion. The defect ion oscillates back and forth along the open channel in the z-direction formed by four chains of Ti-O octahedra. The six 1NN oxygen ions around the interstitial defect form a Ti-O octahedron, which directly limits the amplitude of the defect oscillation. Four of the 1NN oxygen ions on a same plane, in which the Ti defect ion oscillates, involve in the oscillation mode actively. Their oscillation directions have three spatial components, while the other two O ions out of the plane are less actively involved and only oscillate oppositely to the movement of the Ti defect ion in the z direction. The nearest Ti ions around the defect ion are involved in the oscillation mode in a complex manner, among which the Ti ions with a non-zero velocity in the x or y component responding most actively to the movement of the defect ion.

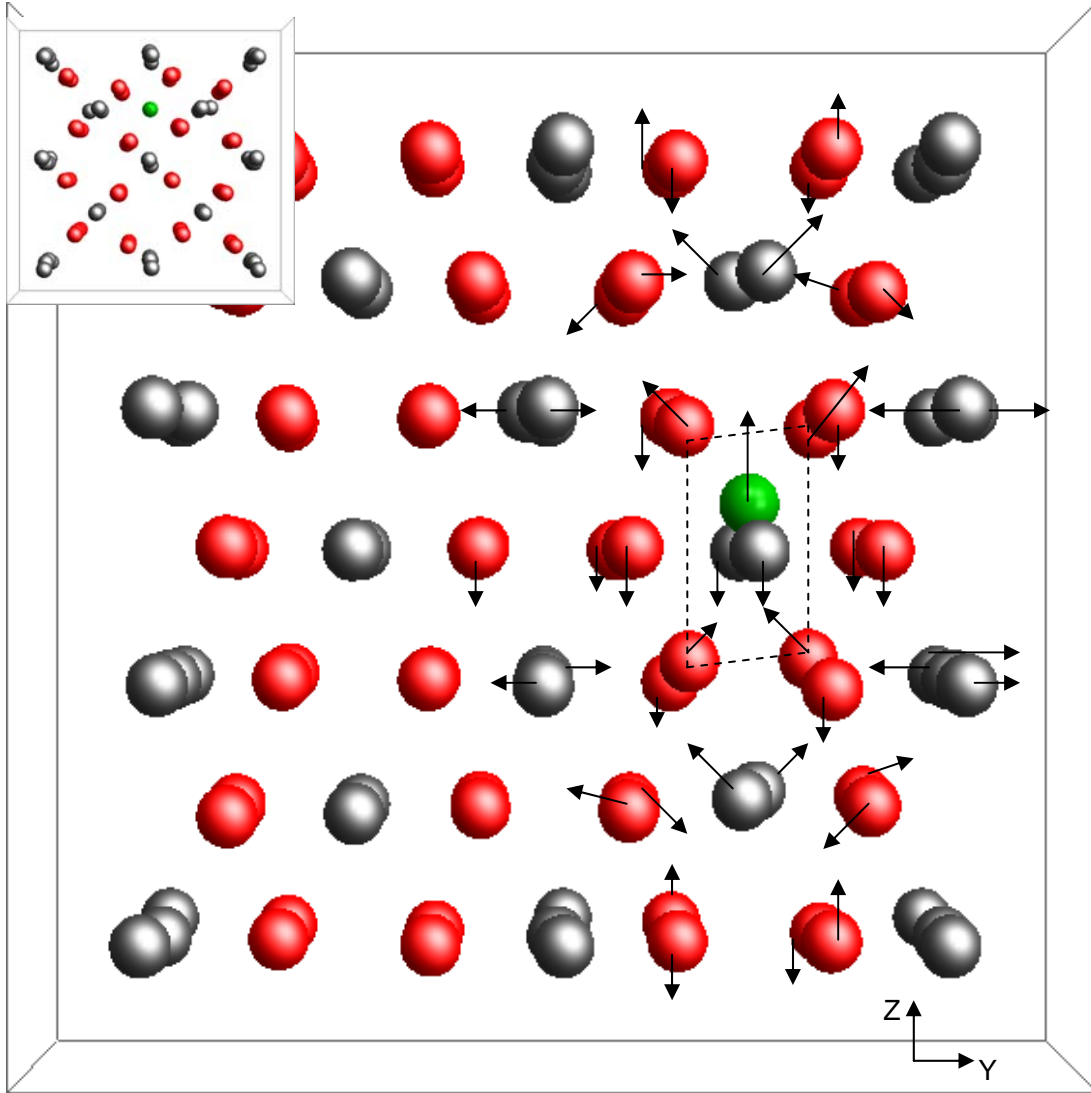


Figure 3.13 The optical phonon mode, ω_{1st}^O , that contributes most to the phonon free energy difference between Ti_i^{4+} and Ti_i^{3+} defect structures at high T. The Ti interstitial defect ion is labeled in green; other Ti ions are labeled in gray and oxygen ions are labeled in red. The arrows show the oscillation directions of the ions near the Ti interstitial defect ion. The viewing direction is along the x-axis for the main figure, while the inset is along the z-direction. Four out of the six O 1NNs of the defect ion are

connected by the dashed lines, which forms a plane for the defect ion to oscillate in.

As shown in Figure 3.9, the oscillation frequency of this ω_{1st}^O mode for the Ti_i^{4+} defect structure is about 1.4 THz lower than for the Ti_i^{3+} at Gamma point, which indicates a lower stiffness constant for Ti_i^{4+} defect ion oscillating along the z-direction. This is confirmed by the DFT calculation of the force on the defect ion induced by its displacement along the z direction in the open channel for both defective supercells. The origin of the difference in the stiffness constants can be understood by a microscopic analysis of the charge distributions and bond lengths in these structures. In Figure 3.14 the difference in the number of electrons within the Bader volume of the corresponding ions between the two defective supercells are calculated by the same Bader analysis method as described in Chapter 2. As analyzed in Chapter 2, the additional unit charge in the Ti_i^{3+} supercell is distributed throughout the whole supercell. Immediately around the defect ion, the charge difference is more significant, but Figure 3.14 shows only around 10% of the one unit charge difference is involved in this area, while the other 90% is distributed throughout the supercell without any obvious localization. However, the ion relaxation profile in Figure 3.15 shows that the positions of the ions farther away from the defect ion can still relax very differently depending on the charge of the interstitial despite the relatively homogenous charge difference distribution in the region— see for example the four Ti ions in the Ti group 6 (from #54 to #57) or the two O ions in the O group 6 (#28 and #29). The six 1NN oxygen ions experience less electrostatic attraction

to the defect ion and are thus farther away from it in Ti_i^{3+} supercell, since the decrease of positive charge state for the Ti defect ion is much larger than the increase of negative charge state for the six O 1NN ions. Two Ti ions in Ti group 1(#8 and #9) move much closer to the defect ion in the Ti_i^{3+} supercell, as the positive charge states of all the three Ti ions involved in the interaction decrease, making the electrostatic repulsion forces smaller. The reason is the same for the farther Ti ions in the Ti group 6 (between # 54 and #57) to move toward the defect ion. It is in response to the movements of the these Ti ions that makes the two oxygen ions in the O group 6 (#28 and #29) become abnormally closer to the defect ion. Most of the other Ti and O ions reside at almost the same distances from the defect ion in the two defective supercells, which reflects the constraint of the fixed supercell volume relative to the relaxed pure structure.

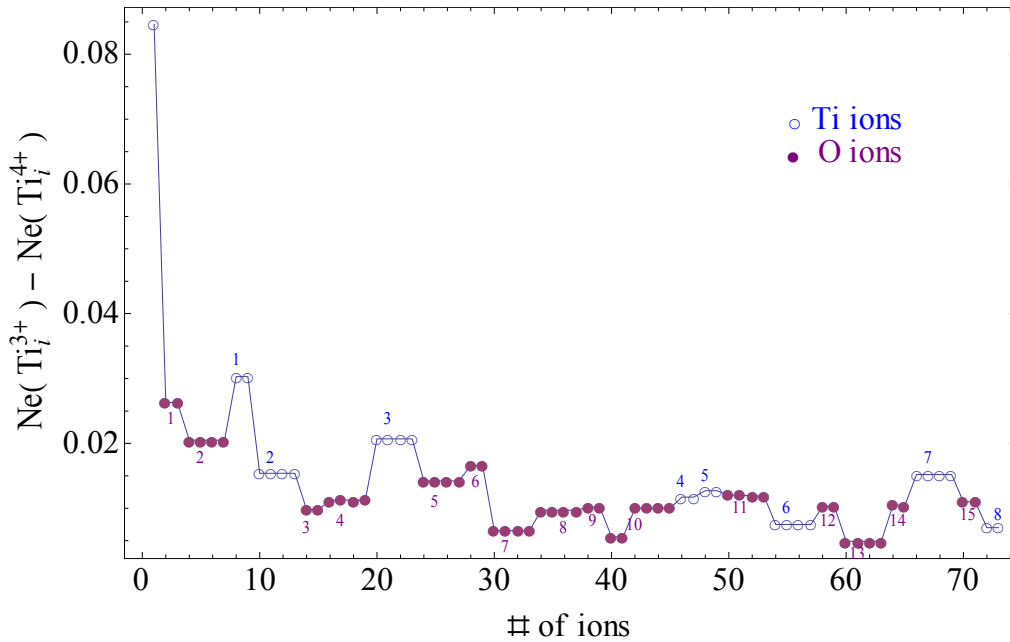


Figure 3.14 The differences in the number of electrons within the Bader volume of each

ion, N_e , for all the corresponding ions between Ti_i^{3+} and Ti_i^{4+} defective supercells. The numbers on the x axis are sorted based on their distances, R , from the defect ion starting from the nearest one. Groups of the oxygen ions with equal distance from the defect ion are labeled with increasing numbers below the symbols, while titanium ion groups are labeled above.

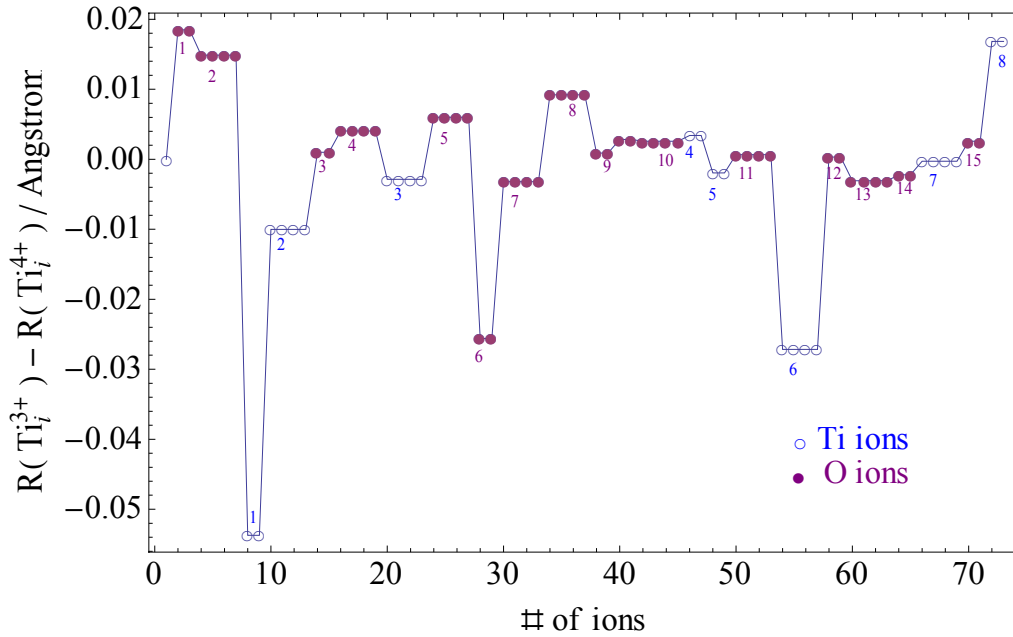


Figure 3.15. The differences in the distance from the defect ion to each ion, R , for all the corresponding ions between the Ti_i^{3+} and Ti_i^{4+} defective supercells. The numbers on the x axis are sorted based on their distances, R , from the defect ion starting from the nearest one. Groups of the oxygen ions with equal distance from the defect ion are labeled with increasing numbers below the symbols, while titanium ion groups are labeled above.

The charge distribution and ion position relaxation shown in Figure 3.14 and 3.15, respectively, can be further inserted into Coulomb interaction formula to help build a simplified model to analyze how a specific group of ions influences the stiffness constant of the defect ion oscillating in the z direction. The charge state of each ion is defined by the summation of negative N_e and its positive nuclear core charge state, as in Chapter 2. The position of each ion after relaxation is also known from the DFT calculation. The vector summation of the electrostatic forces from all the ions in the supercell to the defect ion can be calculated when the defect ion moves along the z direction in the open channel. However, the calculated total electrostatic force on the defect ion does not provide a restoring force for the defect to oscillate in the z direction. Instead, it is an anti-restoration force along the z direction. This is not surprising as the short range repulsion force was not included in the model. There are several available models can be used to describe this behavior, as reviewed by Finnis[75]. The major problem is indentified to be the neglect of the charge transfer effect among all the ions in the supercell associated with the displacement of the defect ion away from its equilibrium position. The charge transfer effect can be considered by analyzing the charge redistribution and the total force on the defect ion directly from the static DFT calculation when the defect ion is displaced along the z direction. The recalculated total force on the defect ion from this modified model gives the restoration forces as described below, with the one for the Ti_i^{3+} defective supercell larger than that for the Ti_i^{4+} defective supercell.

One advantage of the model is that the contribution to the total restoration force from different groups of ions in the supercell can be analyzed separately to help identify which group of ions dominates the effect. Figure 3.16 shows all the NN Ti ions (Ti group #1 and #2) provide the anti-restoration forces, while the 3rd Ti group is the only Ti group of ions that provides the restoration force. The four Ti ions in the 3rd Ti group are located in the same y coordinate as the defect ion, but have different z coordinate as shown in Figure 3.13. Figure 3.17 shows the two O NN ions in the 1st O group, which are located out of the plane labeled by the dashed lines formed by the other four NN O ions in the 2nd O group, provide the strongest restoration force among all groups. The four O ions in the 2nd O group provide the largest difference in the restoration force between the Ti_i^{3+} and Ti_i^{4+} defective supercells, which can be more clearly seen in Figure 3.18.

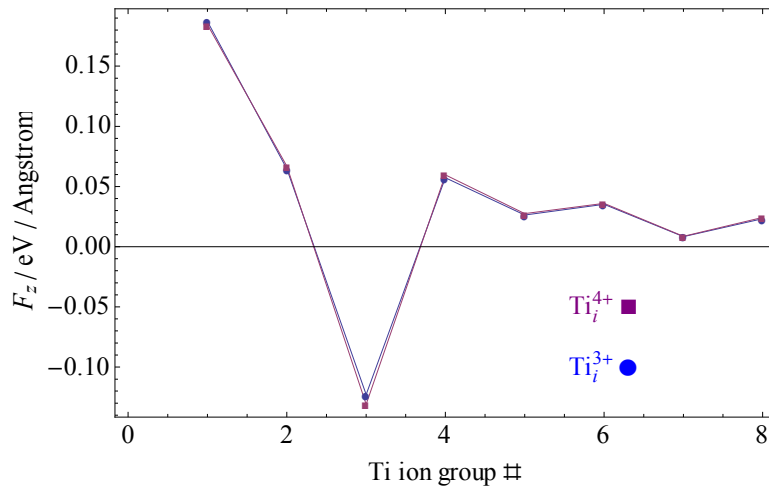


Figure 3.16. Calculated forces on the defect ion along the z-direction from different groups of Ti ions in the two defective supercells. The numbers of groups correspond to the numbers labeled in Figure 3.14 and 3.15. The defect ion is displaced along the positive z direction by 0.02 Angstrom.

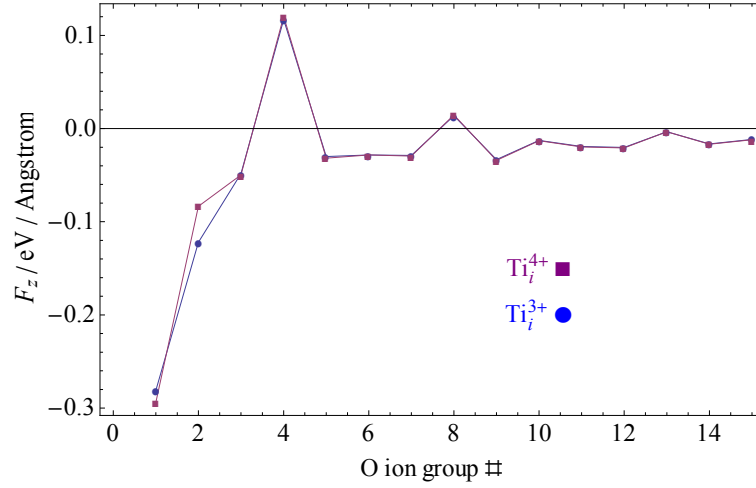


Figure 3.17. Calculated forces on the defect ion along the z-direction from different groups of O ions in the two defective supercells. The numbers of groups correspond to the numbers labeled in Figure 3.14 and 3.15. The defect ion is displaced along the positive z direction by 0.02 Angstrom.

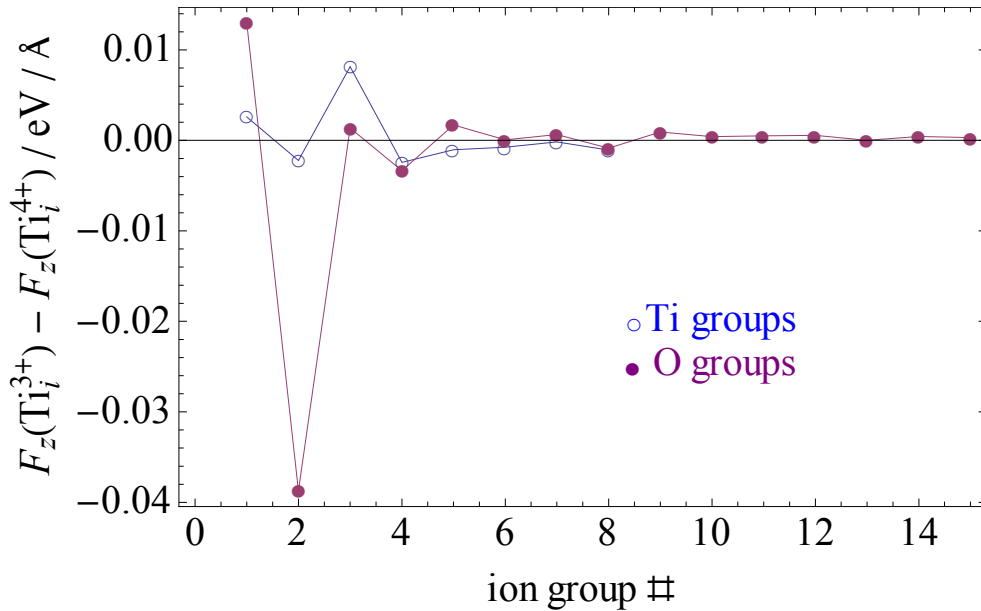


Figure 3.18 Restoration force difference along the z-direction between the corresponding ion groups in the Ti_i^{3+} and Ti_i^{4+} defective supercells. The numbers of groups correspond

to the numbers labeled in Figure 3.14 and 3.15. The defect ion is displaced along the positive z direction by 0.02 Angstrom.

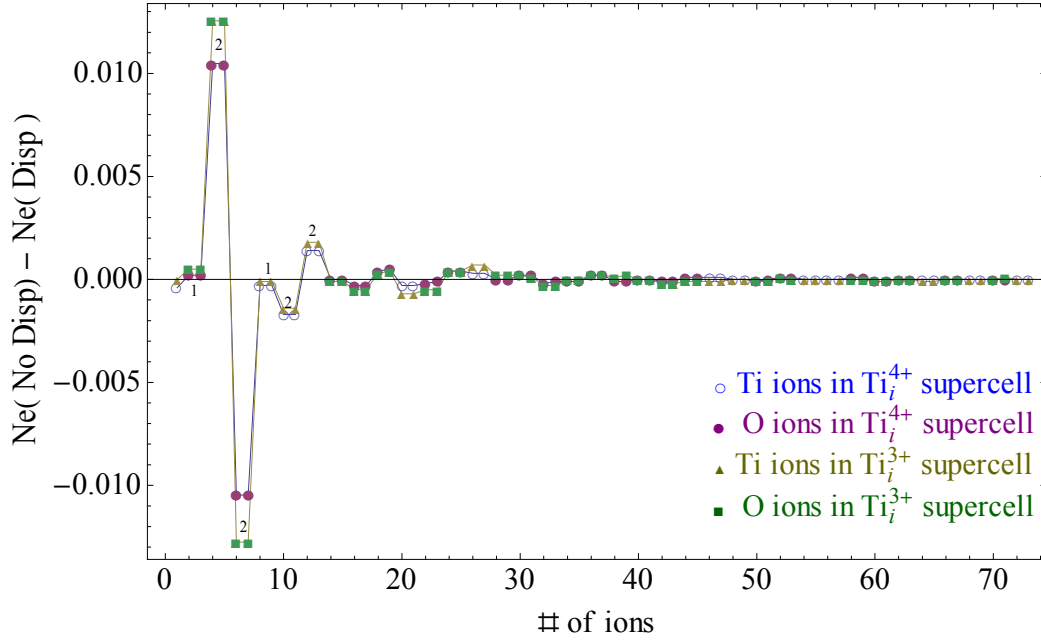


Figure 3.19 The N_e differences for all the corresponding ions before and after the displacement of the defect ion along positive z direction by 0.02 Angstrom, in the Ti_i^{3+} and Ti_i^{4+} defective supercells, respectively. The numbers on the x axis are sorted based on their distances, R , from the defect ion starting from the nearest one.

As mentioned earlier, the charge transfer effect among other ions caused by the displacement of the defect ion is important in providing the restoring force in this model. Figure 3.19 shows the largest charge transfer effect happens to the four NN O ions in the 2nd O group. These four O ions are on the corners of the rectangle labeled by the dashed lines in Figure 3.13; the first two O ions (#3 and #4) are higher in the z direction. Figure

3.19 shows that when the defect ion is moved up in the z direction by 0.02 Angstrom, around $0.01e$ negative charges are transferred from the upper two O ions to the lower two ones in the 2nd O group in the Ti_i^{4+} defective supercell, while around 0.013 charges are transferred in the Ti_i^{3+} defective supercell. Obviously, this charge transfer strengthens the electrostatic attraction forces from the lower two O ions to the defect ion, with a weakening of the attractive forces from the upper two O ions in the 2nd O group. The net effect is a strengthening of the restoration force for the defect ion. The larger charge transfer in the Ti_i^{3+} defective supercell among the O ions in the 2nd O group is the major reason for its larger restoration force to the defect ion. The origin of this charge transfer partly arises from the Pauli Exclusion Principle or the anti-symmetrical exchange relation of the fermions that applies to the overlapping electron clouds between the defect ion and the NN O ions associated with the movement of the defect. Compared with the corresponding ions in the Ti_i^{4+} defective supercell, the 0.08 more negative charges on the Ti defect ion and 0.02 more negative charges on each of the four O ions in the 2nd O group are the major reason for the stronger charge transfer in the Ti_i^{3+} defective supercell caused by the Pauli exclusion effect; without the additional charge transfer, the Ti-O bond length extension in the defect Ti-O octahedron of the Ti_i^{3+} supercell is not big enough to fully balance the effect caused by the negative charge accumulation in this region when the defect ion moves.

From Figure 3.19 it is also seen that there is a transfer of around 0.002 negative charges from the two lower Ti ions to the two upper ions along the z direction in the 2nd

Ti group when the defect is displaced upward along the z direction, which strengthens the anti-restoration force provided by the 2nd Ti group. This effect can be considered as a response of the negative charges to balance the upward movement of the positive Ti defect ion. However, it is a minor effect compared with the charge transfer among the O ions in the 2nd O group.

3.3.2 Phonons in the vacancy defective supercells

Figure 3.20 and 3.21 show that neither the V_{Ti} nor V_O defective supercells have an obvious single mode that accounts for most of the phonon free energy differences between different charge states shown in Figure 3.7 and 3.8. Instead, it is the collective contribution from all modes. The phonon modes of the V_{Ti}^{4-} supercells generally have higher frequencies than the partially charged supercells, which accounts for its higher phonon free energy. Conversely, the modes of the V_O^{2+} supercell are generally lower in frequencies when compared with the modes of the partially charged defective supercell, which accounts for its lower phonon free energy. The trend depicted in Figure 3.20 and 3.21 is consistent to the phonon density of states analysis, which includes all the q-points in the q-mesh. Thus the above argument is general and not limited to the Gamma point.

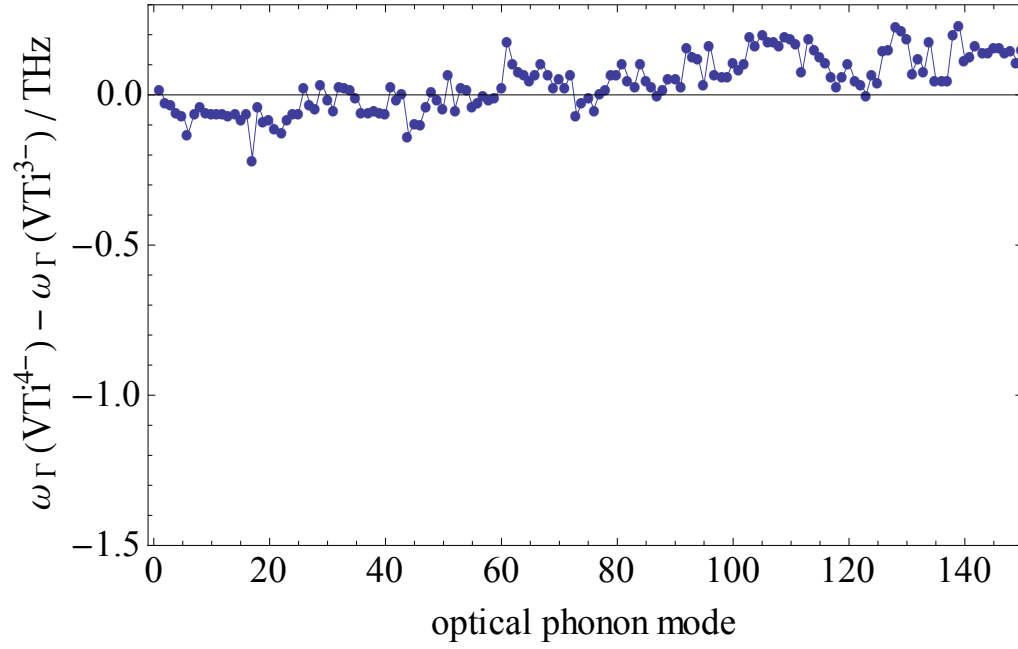


Figure 3.20 Optical phonon frequency differences at the Gamma point for the lowest 150 modes between V_{Ti}^{4-} and V_{Ti}^{3-} defect structures at 2x2x3 supercells.

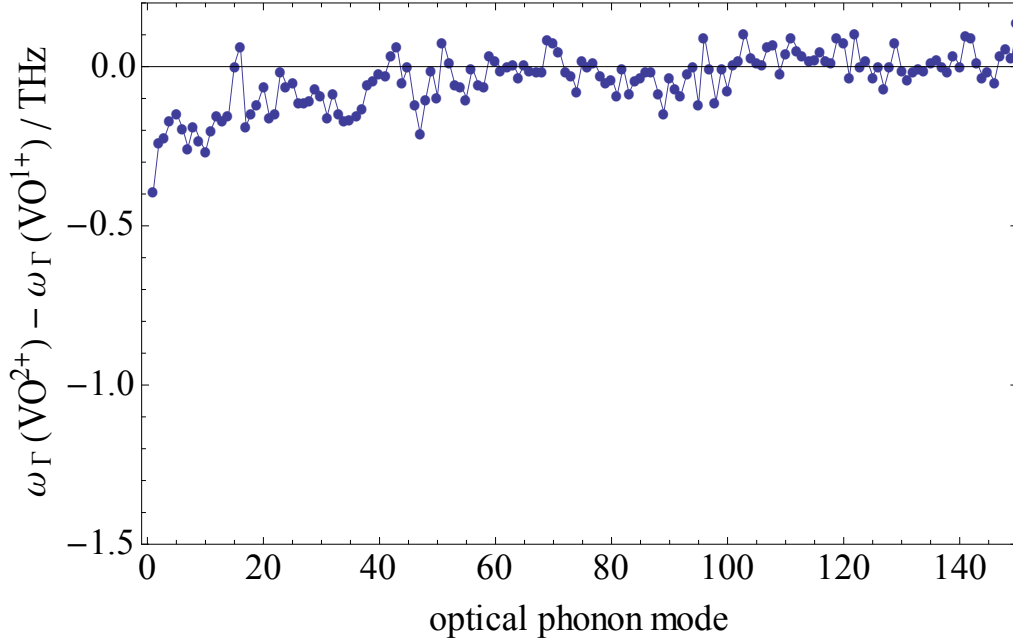


Figure 3.21 Optical phonon frequency differences at the Gamma point for the lowest 150 modes between VO^{2+} and VO^{1+} defect structures at $2 \times 2 \times 3$ supercells.

3.3.3 Phonon PDOS and their correlations

By using the polarization vector, which is the eigenvector of the dynamical matrix, the partial phonon density of states (PDOS) can be calculated for each ion in the defective and pure supercells. The similarity of the PDOS between corresponding ions in the defective and pure supercells can be indicated by the correlation value of the two PDOS spectra. Two identical spectra have the correlation value of 1. In an infinitely large defective supercell, the PDOS of the ions far away from the defect ion should be very close to the corresponding PDOS in the pure supercell and thus have the correlation

values close to 1. The average correlation value around 0.7 between the ions close to the edge of the defective and pure supercells shown in Figure 3.22 may suggest that larger supercells than 2x2x3 are needed if one is interested in the absolute values of the phonon free energy difference between the defective and the pure supercell. But the phonon calculation in the larger 3x3x5 Ti interstitial supercell requires one thousand dedicated CPUs to finish within 30 days, which is beyond the usual computational resources available. However, Figure 3.22 shows the correlation values for the corresponding ions between the Ti_i^{3+} and Ti_i^{4+} defective supercells are very close to 1 with little fluctuation beyond 4 Angstrom, while the major difference is localized around the defect ion. Therefore, the phonon free energy differences between the 2x2x3 sized differently charged defective supercells should be much more precise than the phonon free energy difference between the 2x2x3 defective and the pure supercells.

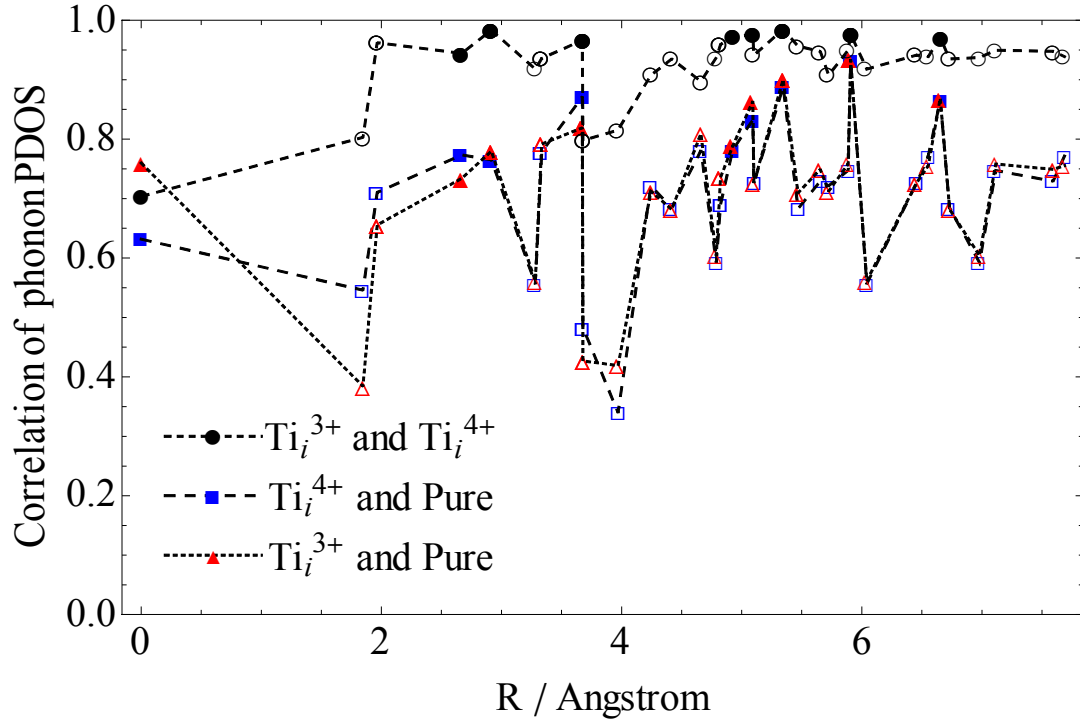


Figure 3.22. Correlations of phonon PDOS between the corresponding ions in the defective and pure supercells at the size of $2 \times 2 \times 3$ unit cells, sorted by their distances from the defect ion. The empty symbols are for O ions and filled symbols are for Ti ions.

Chapter 4

Charged Point Defect related Gibbs Free Energy

4.1 Quasi-Harmonic Calculation of Gibbs Free Energy in Pure Rutile

In Chapter 3 the phonon free energies and internal energies of the defective and pure structures were calculated with the harmonic approximation at the fixed volume of relaxed pure rutile. However, this calculation neglected the fact that both the phonon spectrum distribution and internal energy of the structure can change with temperature. More importantly, these effects can change in different ways depending on the defects present in the supercells. In this Chapter, the Quasi-Harmonic approximation is used to address the effect of temperature on the phonon free energy and Gibbs free energy in the pure rutile structure (Section 4.1) and in the defective structures (Section 4.2). The influence of this correction on the defect phase diagram will be discussed in Section 4.3.

The overall effect of temperature on the phonon spectrum distribution can be separated into pure-volume and pure-temperature components[76]. As T increases, the pure-volume effect, i.e. the thermal expansion of the material, tends to decrease most phonon frequencies in rutile TiO_2 [70, 76]. At the same time the pure-temperature effect tends to increase the frequency of certain optical mode in rutile, such as the soft long-wavelength transverse-optical A_{2u} mode[73]. Phonon mode A_{2u} is a relative oscillation between the whole cation and the whole anion sublattices along the c -axis of

rutile. A previous work [70] has modeled this phonon mode by a combination of short range Buckingham-type potential and long range electrostatic potential, which found the long-range electrostatic interaction favors the ferroelectric phase whereas the short-range repulsive interaction favors the paraelectric phase related to the A_{2u} mode. When the volume of the rutile unit cell expands in response to an increasing temperature, the short-range repulsive interaction decreases, softening the A_{2u} mode, as has been predicted from the previous DFT works[70, 77] and the current calculation shown later. To counter this effect a pure-temperature effect, which can not be included in the DFT quasi-harmonic approximation, was proposed to cause an increase in the effective short-range interatomic repulsion with increasing temperature and reduces the long range electrostatic interaction to harden the A_{2u} mode[70]. Since the pure-temperature effect dominates in this mode, the A_{2u} mode makes rutile TiO_2 an incipient ferroelectric observed experimentally[44, 73, 76]. This is an example of the anharmonic effect in the phonon mode with changing temperature. The possible anharmonic effects include thermal expansion, phonon-phonon interactions, where the atomic motions are beyond the harmonic range[65, 68]. Phonon-phonon interactions and thermal smearing, which largely belong to the pure-temperature effect, can be treated using the pseudoharmonic approximation or self-consistent harmonic approximation[74]. The quasi-harmonic approximation considers these anharmonicities in the pure-temperature contribution as weak effects [74]. There are some approaches to expanding the anharmonic part of the Helmholtz free energy in terms of powers of T to correct the quasi-harmonic

approximation, but the drawback is the introduction of many volume-dependent adjustable parameters [69, 78-80]. In this section, the part of the anharmonic effect of the phonons at high temperatures arising from thermal expansion is considered for both the defective and the pure structures using the quasi-harmonic approximation, while other anharmonic effects from the pure-temperature contribution are neglected in this approach. The validity of the choice of the quasi-harmonic approximation will be evaluated through the comparison of the calculated thermal expansion coefficient to the experimental one.

Gibbs free energy, $G(T,P)$, can be transformed from Helmholtz free energy, $F(V,T)$, through the Legendre transformation. This involves the evaluation of the minima of $[F(V,T)+PV]$ with respect to the volume, as shown below:

$$\begin{aligned} G(T, P) &= \min_V [F(V, T) + PV] \\ &= \min_V [U(V) + F_{ph}(V, T) + PV] \end{aligned} \quad (4.1)$$

The internal energy $U(V)$ in eq (4.1) is the total electronic energy calculated from DFT. $F_{ph}(V,T)$ is the phonon free energy calculated by the harmonic phonon calculations described in Chapter 3. The PV term is the work done by the system on the environment and can be neglected at ambient pressure. The thermal expansion can be evaluated by identifying the volume that minimizes the right hand side of eq (4.1) over a series of temperatures in the quasi-harmonic approximation. The energies and the phonon free energies of pure rutile are calculated for a series of 29 different volumes in a range of $0.977V_0$ to $1.061V_0$, where V_0 is the volume of relaxed pure rutile when the phonon energy is not considered.

The calculated volume expansion and thermal expansion coefficient as a function of T are shown in Figures 4.1 and 4.2, respectively. The calculated thermal expansion coefficient is further compared with two sets of experiments in Figure 4.2 [81]. Saxena's measurement correctly captures the trend that the thermal expansion coefficient vanishes as T approaches 0K [67], making it more reliable than Touloukian's data. The calculated thermal expansion coefficient agrees reasonably well with Saxena's measurement in the whole temperature range shown in Figure 4.2. Particularly, there is no obvious divergence from the experimental data at high T , which validates the choice of the quasi-harmonic approximation for the following analyses.

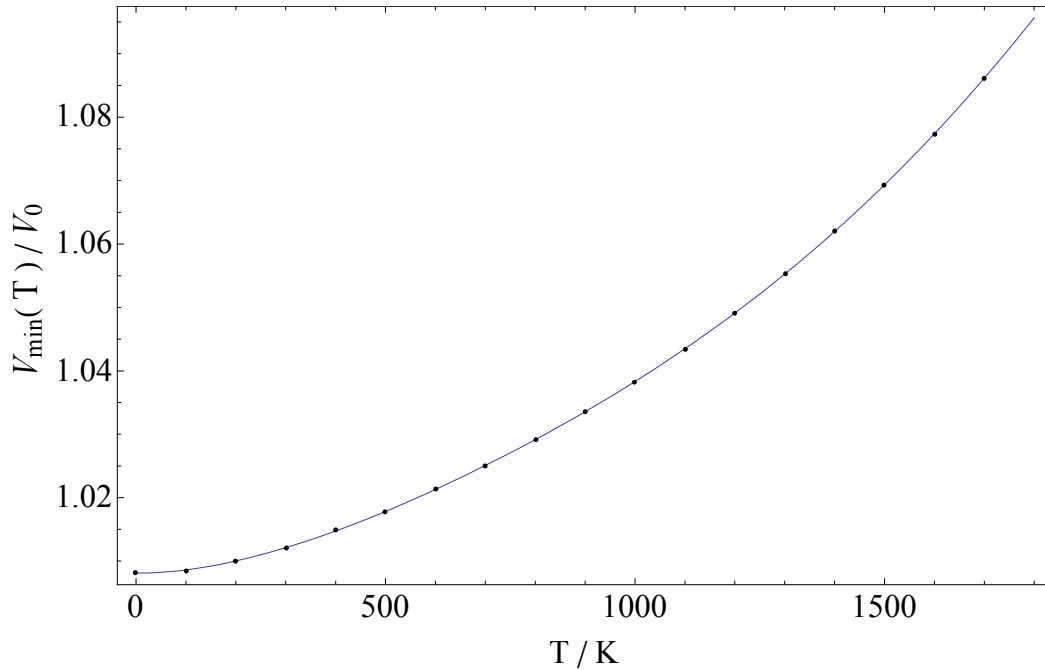


Figure 4.1 Calculated $V_{\min}(T)$ as a function of T up to 1800K in the quasi-harmonic approximation.

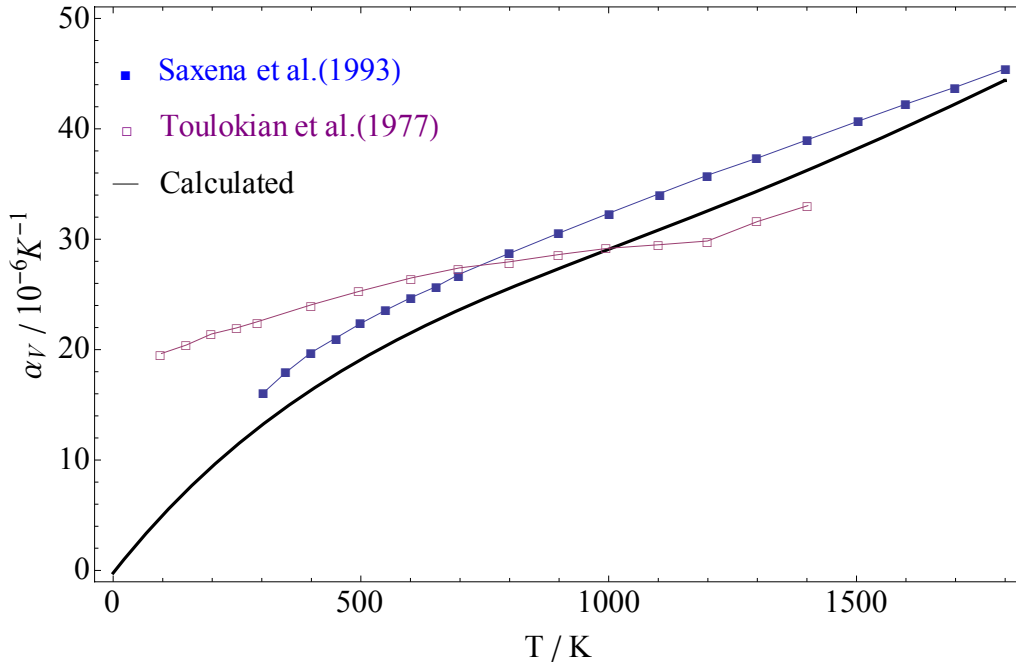


Figure 4.2 Calculated volume thermal expansion coefficient compared with experimental data from two different groups up to 1800K.

Figure 4.3 compares the calculated molar Gibbs free energy of rutile with experimental chemical potential measurements up to 1800K. The molar phonon free energy and internal energy from the quasi-harmonic approximation are also shown in Figure 4.3. For pure rutile the internal energy increases with temperature, while the phonon free energy decreases with it. Their combined effect gives the calculated chemical potential, which agrees well with experimental results, shown in Figure 4.3. The good agreement between the phonon free energy calculated with the harmonic approximation and the experimental chemical potential shown in Figure 3.3 in the previous chapter reflected the fact that the influences of the thermal expansion to the

phonon free energy and the internal energy happened to cancel each other in pure rutile. However, these two effects in the quasi-harmonic approximation behave differently when the charged point defects are considered, which will be discussed in the next section.

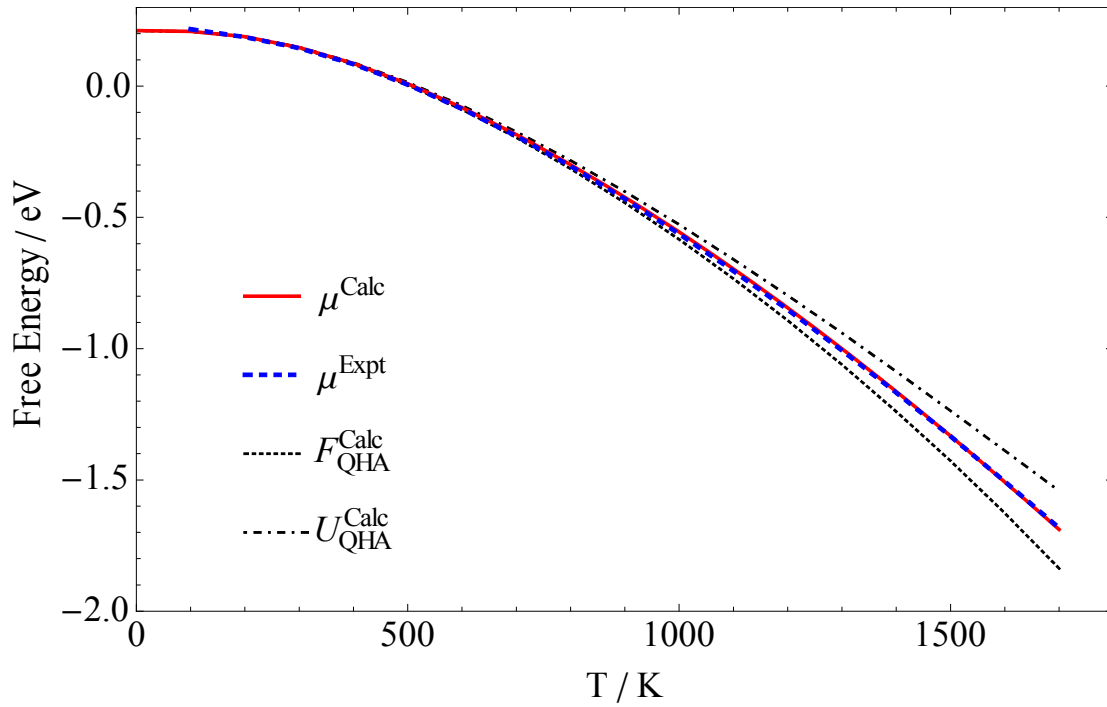


Figure 4.3 Calculated molar Gibbs free energy, $\mu_{\text{QHA}}^{\text{Calc}}$, from the quasi-harmonic approximation; experimental chemical potential of rutile TiO_2 , μ^{Expt} ; calculated molar phonon free energy from the quasi-harmonic approximation, $F_{\text{QHA}}^{\text{Calc}}$; and the calculated internal energy, $U_{\text{QHA}}^{\text{Calc}}$, from the quasi-harmonic approximation as functions of temperature for rutile TiO_2 .

The decrease in the phonon free energy with increasing volume expansion at a

certain T , as shown in Figure 4.4, suggests most of the phonon modes soften with increasing volume in rutile TiO_2 in agreement with previous works[70, 76] and the basic argument from quantum mechanics and statistical physics that the energy levels are lowered by the volume expansion of the system[65, 69]. This phenomenon can also be understood from the charge transfer effect as discussed in the previous chapter that the expanded volume, in general, lowers the short-range repulsive forces caused by the local charge transfer. However, the sharp frequency drop of the A_{2u} mode to negative values when the applied negative pressures exceed -40 kBar predicted in one previous work [70] can not be replicated. The ferroelectric transition is predicted by applying negative pressures until up to around -140 kBar in the present work tested by the exchange-correlation functionals of LDA ($\text{Ti}:3d^24s^2$, $\text{O}:2s^22p^4$) and LDA ($\text{Ti}:3p^63d^24s^2$, $\text{O}:2s^22p^4$). This difference may be due to the inadequate force convergence criteria of 0.02 eV / Angstrom used in the previous work[70] for the phonon calculation, while the criteria in the present work is 10^{-5} eV /Angstrom. The current result agrees well with a recent work[77] with similar force convergence criteria. The B_{1g} mode is the only mode with negative Gruneisen parameter in rutile, in agreement with previous works[70, 77], which was speculated to account for the pressure-induced phase transition of rutile to CaCl_2 structure at around 26 kBar[76].

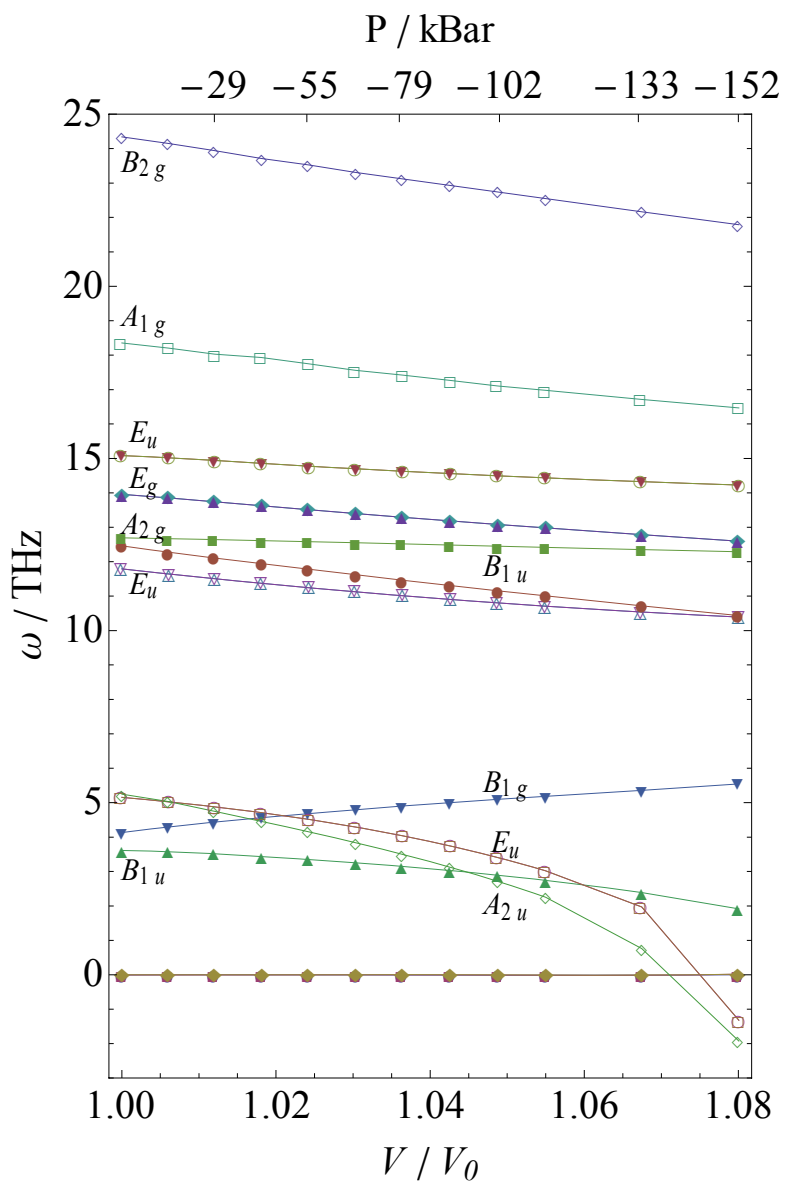


Figure 4.4 Calculated phonon modes with volume expansion in the unit cell of pure rutile TiO_2 .

4.2 Quasi-Harmonic Calculation of Gibbs Free Energy in Defective Structures

4.2.1 Ti interstitial defective supercells

To meet the dilute solution approximation, the volume of the defective supercell at a certain T for the quasi-harmonic calculation is set at the equilibrium volume of the pure structure corresponding to that T (See Figure 4.1.) The calculated phonon free energy differences between the $2 \times 2 \times 3$ defective supercells with $\text{Ti}_i^{\text{q}+}$ defects and the $2 \times 2 \times 3$ pure supercell are shown in Figure 4.5. For the supercell with the Ti_i^{4+} defect, the energy difference slightly decreases with T below 600K and then increases with T quickly above 600K. For the supercell with the Ti_i^{3+} defect, it increases with T though the whole temperature range. These trends are opposite to the prediction of the harmonic approximation shown in Figure 3.6. The reason for the discrepancy is that the frequencies of most phonon modes in the $\text{Ti}_i^{\text{q}+}$ defective supercell decay more slowly than in the pure structure with volume expansion, as shown in Figure 4.6, which makes the phonon free energies of the Ti_i defective supercells larger than that of the pure supercell at high T . One noticeable exception is the first optical phonon mode, ω_{1st}^O , discussed in detail in Chapter 3 for a supercell with volume V_0 , which drops very quickly to zero frequency and then to negative frequencies in the Ti_i^{4+} supercell with increasing supercell volume. The quick softening of this mode below 600K, or $1.02V_0$, balances the effect of the slower

frequency drops of most other modes in the Ti_i^{4+} supercell as compared to the pure supercell, accounting for its relatively flat temperature dependence of the phonon free energy difference below 600K in Figure 4.5. Above 600K, or $1.02V_0$, because the negative frequencies of this mode do not contribute to the calculated phonon free energy, the slower frequency decay of other phonon modes compared to the pure structure dominate, which accounts for the quick increase of the phonon free energy difference above 600K in Ti_i^{4+} supercell. The negative frequency of the ω_{1st}^O mode in the Ti_i^{4+} supercell may suggest that Ti_i^{4+} is not stable or energetically favorable at expanded volumes beyond $1.02V_0$. The detailed property change of this ω_{1st}^O mode is discussed later. Also, the comparison of the phonon DOS in Figure 4.7 shows that the frequencies of most modes drop more slowly in the Ti_i^{4+} supercell than in the Ti_i^{3+} supercell with increasing volume, especially for high-frequency hard modes, making the phonon free energy higher in the Ti_i^{4+} supercell than in the Ti_i^{3+} supercell at high T, where the frequency of ω_{1st}^O is negative in Ti_i^{4+} supercell and thus does not dominate.

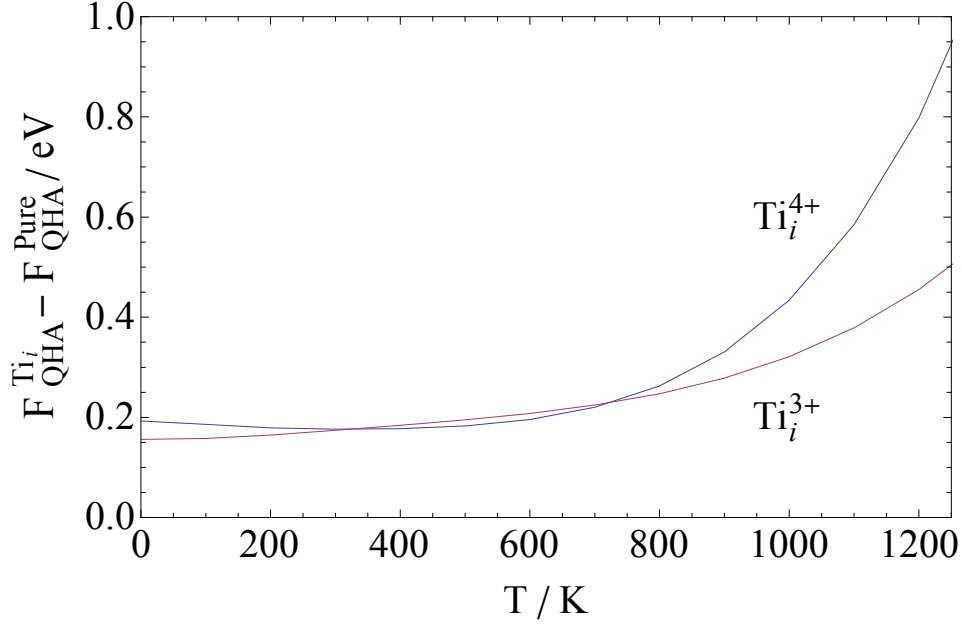


Figure 4.5 Calculated phonon free energy differences between Ti_i^{q+} defective supercells and the pure supercell from the quasi-harmonic approximation.

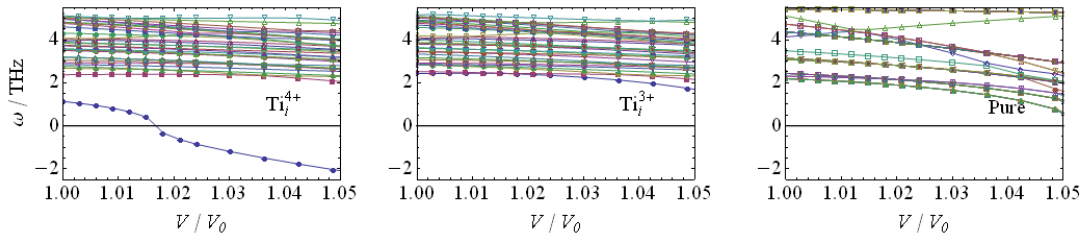


Figure 4.6 Lowest 30 optical phonon modes at Gamma point as a function of volume in Ti_i^{4+} , Ti_i^{3+} and pure 2x2x3 sized supercells. The modes in the highly symmetric pure structure are mostly degenerate, while most modes in the defective supercells are non-degenerate.

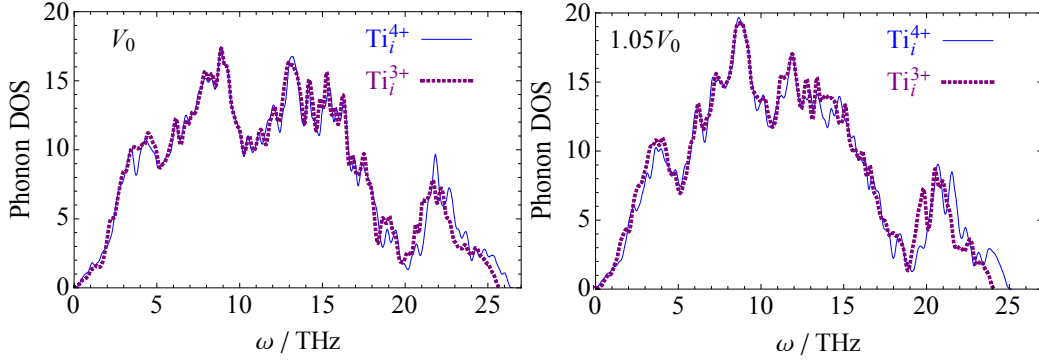
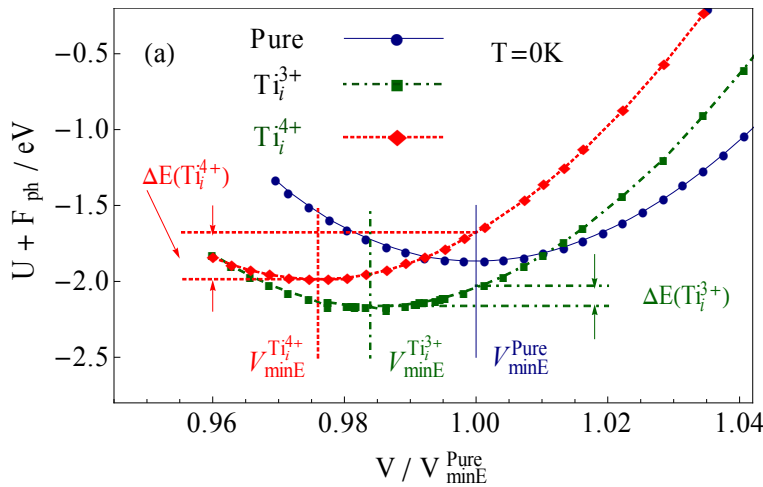


Figure 4.7 Phonon DOS of Ti_i^{3+} and Ti_i^{4+} defective supercells at volume V_0 (left) and $1.05V_0$ (right).

The above general trends of the frequency changes can be further understood from the change of strain energies in different structures with volume expansion. Fig. 4.8(a) presents the Helmholtz free energy of the Ti_i^{4+} and Ti_i^{3+} defective supercells in comparison to a pure supercell as a function of the normalized supercell volume at 0 K. In this figure the minima in energy for the charged Ti_i^{q+} defects fall at smaller supercell volumes than the perfect crystal, indicative of the local lattice strain induced by the presence of the defect with a tendency to shrink the volume. ΔE is defined to be the energy difference between the minima in each curve and the energy at a normalized volume of 1 as outlined in Fig. 4.8(a), whose internal energy part ΔU is a measure of the local strain energy induced by the presence of the defect. The magnitude of ΔU depends on the defect charge, e.g. $\Delta U(\text{Ti}_i^{4+})$ is almost twice that of $\Delta U(\text{Ti}_i^{3+})$ at 0K as shown in Figure 4.8(b), which helps harden high frequency phonon modes in the defective Ti_i^{4+} supercell as shown in Figure 4.7 at V_0 . But as discussed in Chapter 3 it is the ω_{1st}^O mode

that dominates in the harmonic approximation, which makes the phonon free energy of Ti_i^{4+} decay faster than the energy of Ti_i^{3+} supercell shown in Figure 3.6. However, when the thermal expansion is considered with the quasi-harmonic approximation, the temperature dependence of the lattice strain energy in Figure 4.8(b) shows that $\Delta U(\text{Ti}_i^{4+})$ increases much more quickly than $\Delta U(\text{Ti}_i^{3+})$, especially above 600K, which hardens the modes in Ti_i^{4+} supercell more than the modes in the Ti_i^{3+} supercell to give the trends at expanded volumes shown in Figure 4.7 and at higher temperatures shown in Figure 4.5. Also, the higher local strains in both Ti_i^{4+} and Ti_i^{3+} supercells than in the pure supercell help harden their modes compared to the modes in the pure supercell, which explains the slower frequency drops of most modes compared to the pure supercell shown in Figure 4.6 and the positive phonon free energy differences shown in Figure 4.5.



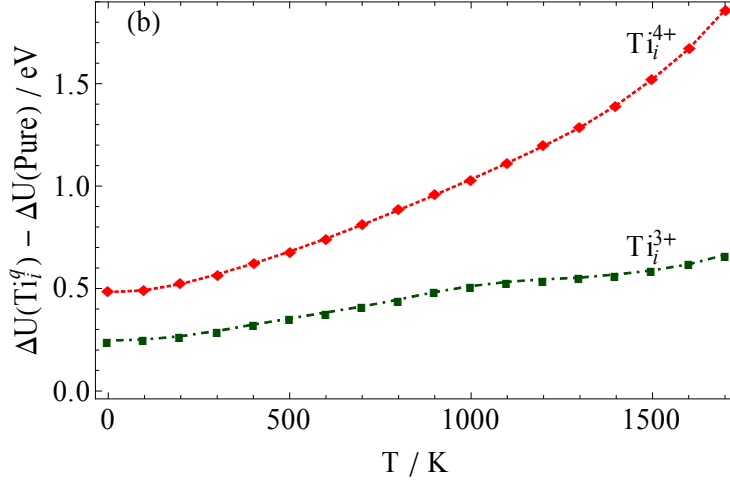


Figure 4.8 (a) The internal energy, U , plus phonon free energy F_{ph} as a function of supercell volume for pure, Ti_i^{3+} and Ti_i^{4+} $2 \times 2 \times 3$ sized supercells at 0K. Note all three curves are shifted in y direction to make them visible in the same energy scale, but this does not influence the definition of ΔE for each defect. (b) The difference between the ΔU of the Ti_i^{q+} defective supercells and the ΔU of the pure supercell as a function of temperature, where ΔU is the internal energy part of the ΔE defined in (a).

The quick softening of the ω_{1st}^O mode at the Gamma point in the Ti_i^{4+} supercell shown in Figure 4.6 is of particular interest because of its large effect on the phonon free energy of the Ti_i^{4+} defect below 600K. As discussed in Chapter 3, this ω_{1st}^O mode is unique in the Ti_i^{q+} defective supercell, which may account for its abnormal behavior here. The underlying charge distributions associated with the volume expansion among the defect ions and the NN Ti and O ions are shown in Figure 4.9. The continuous frequency drop of the ω_{1st}^O mode with volume expansion until the volume of the supercell reaches $1.02V_0$ in the Ti_i^{4+} supercell may be caused by the almost unchanged charge state of the

defect ion and all other NN ions except the continuous increase of charge state of the two Ti ions in Ti ion group #2 below the volume of $1.02V_0$, which make the increasing anti-restoration force from the two Ti ions dominant. In contrast, for the Ti_i^{3+} supercell in the full volume range the continuous and relatively large charge state increase of the defect ion with volume expansion increases the restoration force from the O ion group #1 and #2, which balances the increase of the anti-restoration force from Ti ion group #2 and other groups. For the Ti_i^{4+} supercell beyond $1.02V_0$, although the charge state of the defect ion increases with volume expansion, the increase is relatively slow compared to the Ti_i^{3+} supercell. Thus the increase of the restoration force from its NN O ion groups may not be big enough to balance the increase of the anti-restoration force from the NN Ti ion groups.

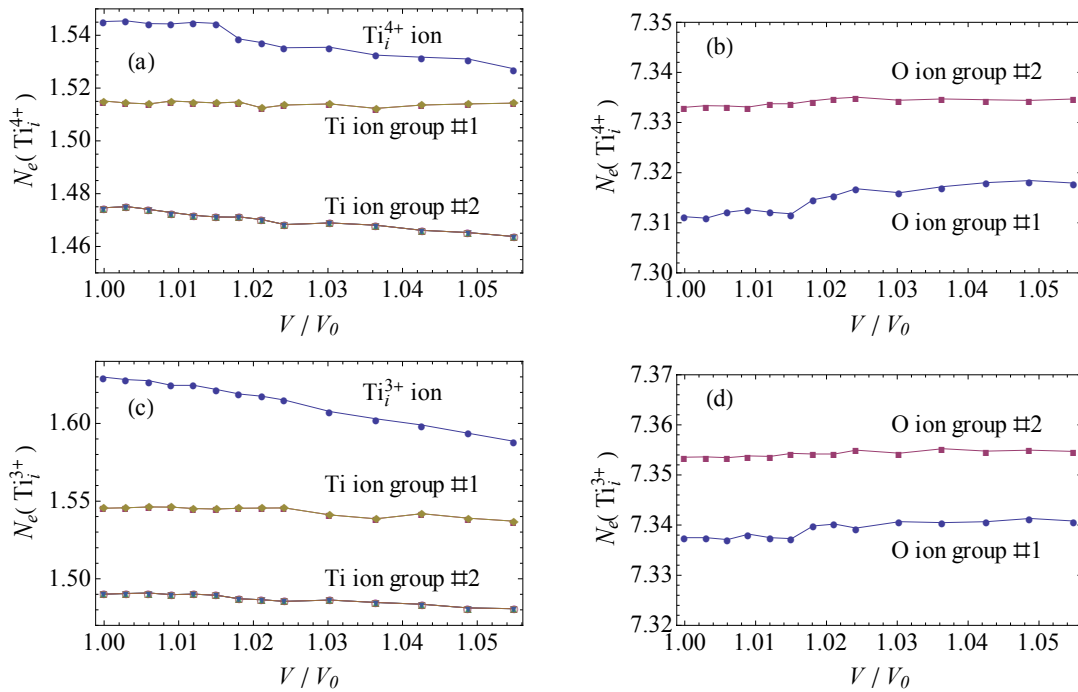


Figure 4.9 Number of electrons within the Bader Volume of each ion (N_e) as a function of

volume expansion of the supercell, for (a) Ti ions in Ti_i^{4+} supercell, (b) O ions in Ti_i^{4+} supercell, (c) Ti ions in Ti_i^{3+} supercell, (d) O ions in Ti_i^{3+} supercell. The ion group numbers correspond to the ones defined in Figure 3.14 and 3.15.

The distances of these NN Ti and O ions from the defect ion with volume expansion are shown in Figure 4.10. Because of the quicker increase of the charge state on the defect ion, the Ti_i^{3+} defect ion binds more tightly the two O ions in the O ion group #1 and repels the two Ti ions in the Ti ion group #1 more strongly with volume expansion. The combined effect of the charge distribution and bond length extension causes the ω_{1st}^O mode to soften more quickly in the Ti_i^{4+} supercell than in the Ti_i^{3+} supercell with increasing supercell volume. Interestingly, this combined effect also makes the mode unstable beyond a volume of $1.02V_0$ in the $2 \times 2 \times 3$ sized Ti_i^{4+} supercell. These behaviors of the charge distribution and bond length extension with volume expansion are tested by LDA ($\text{Ti}:3p^6 3d^2 4s^2$, $\text{O}:2s^2 2p^4$) pseudopotential and at larger $3 \times 3 \times 5$ supercells, which show analogous behavior and thus confirm it is not an artifact from the selection of pseudopotentials or the limited supercell sizes. However, it is worth noting that the current quasi-harmonic calculation does not include the pure-temperature contribution or other anharmonic effects to the phonon oscillation, which may help stabilize this mode in the Ti_i^{4+} supercell at high temperatures.

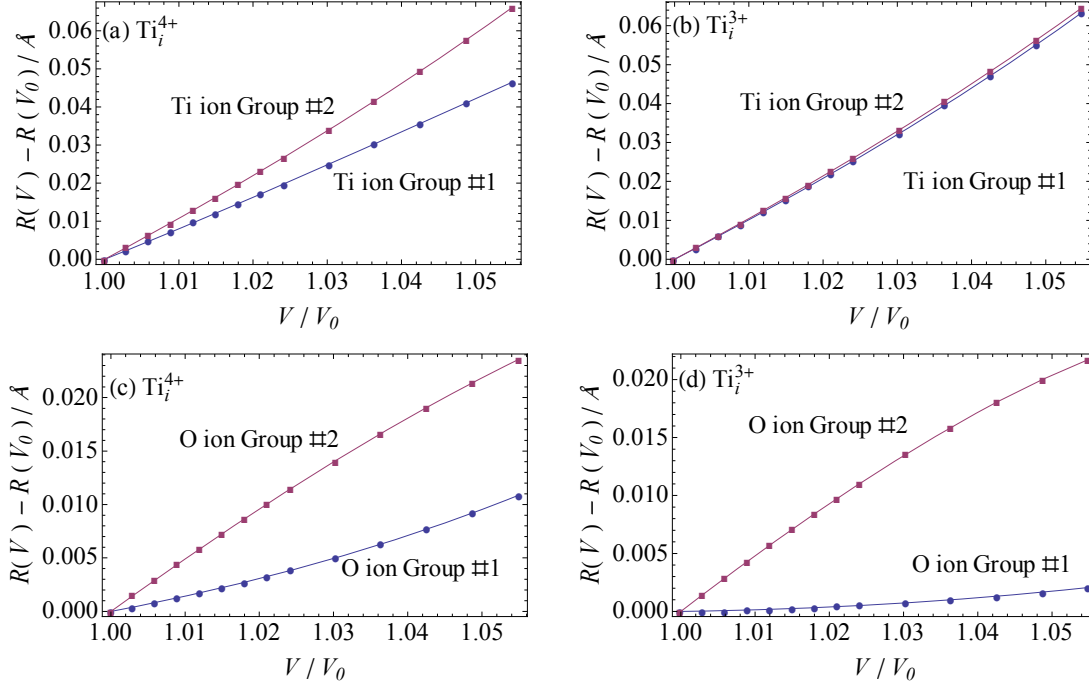


Figure 4.10. Difference between the distances of the ions to the defect ion, $R(V)$, at a certain volume V , and the distances at the volume V_0 , $R(V_0)$, in (a) Ti_i^{4+} supercell for Ti ion groups, (b) Ti_i^{3+} supercell for Ti ion groups, (c) Ti_i^{4+} supercell for O ion groups, (d) Ti_i^{3+} supercell for O ion groups. The ion group numbers correspond to the ones defined in Figure 3.14 and 3.15.

The Gibbs free energy differences can be calculated from the quasi-harmonic approximation by adding the volume-dependant internal energy changes shown in Figure 4.11 to the phonon free energy differences shown in Figure 4.5. The result is shown in Figure 4.12. Since the local strain tends to shrink the volume in the Ti_i^{q+} defective supercells as shown in Figure 4.8, thermal expansion increases the internal energy of the defective supercells, making the Gibbs free energies calculated with the quasi-harmonic

approximation to trend strongly in the opposite direction with increasing temperature compared to the phonon free energy and Helmholtz free energy calculated with the harmonic approximation in the previous chapter. The internal energy of the Ti_i^{4+} defect increases more quickly than the internal energy of the Ti_i^{3+} defect with thermal expansion, which is consistent with its higher strain energy calculated in Figure 4.8.

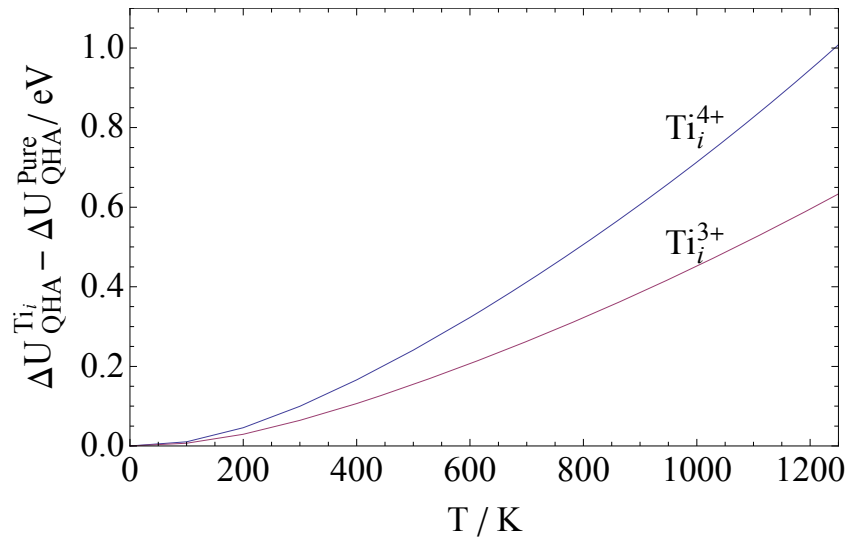


Figure 4.11 Calculate ΔU differences between Ti_i defective supercells and the pure one from the quasi-harmonic approximation. ΔU is the internal energy change referenced to the energy at 0K.

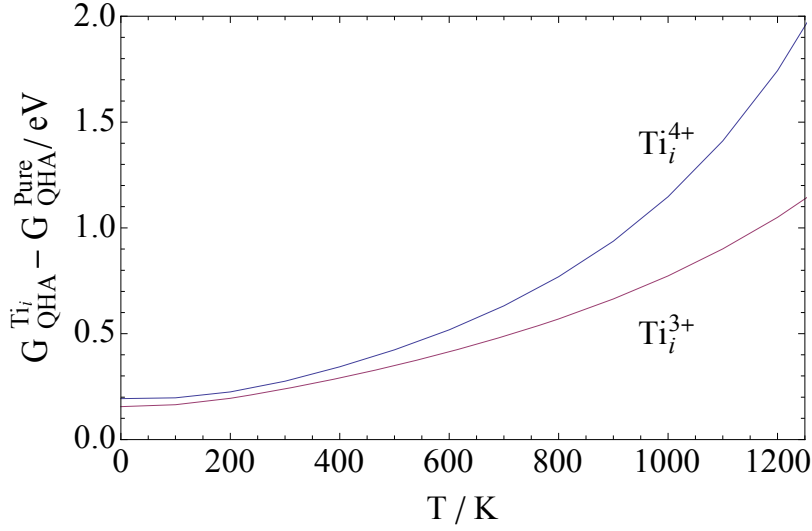


Figure 4.12 Calculated Gibbs free energy differences between Ti_i^{q+} defective supercells and the pure one from the quasi-harmonic approximation.

4.2.2 Ti vacancy and O vacancy defective supercells

The calculated phonon free energy difference between V_{Ti}^{4-} defective supercells and pure supercells increases more quickly with T when calculated with the quasi-harmonic approximation than with the harmonic approximation. Figure 4.13 indicates that most phonon modes decrease in frequency more slowly than the modes in the pure structure with volume expansion, which is confirmed by a similar analysis as the one presented in Figure 4.6. The reason is, like for the Ti_i^{q+} supercells, from the higher

local strain in the V_{Ti}^{4-} defective supercell than in the pure supercell, which helps harden the modes in V_{Ti}^{4-} supercell. However, unlike the $\text{Ti}_i^{\text{q}+}$ supercells, the absolute value of the local strain drops with volume expansion for the V_{Ti}^{4-} supercell, which accounts for its relatively small phonon free energy difference at high T between the QHA and HA calculations when compared to the $\text{Ti}_i^{\text{q}+}$ supercells.

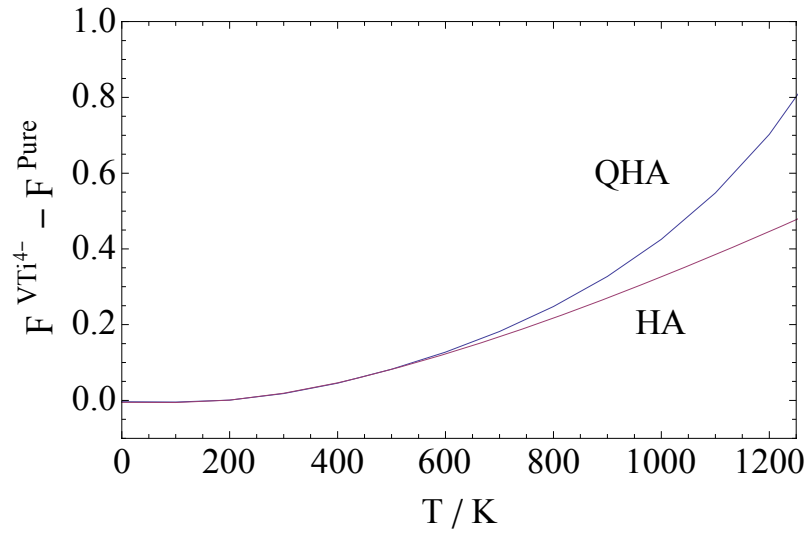


Figure 4.13 Phonon free energy difference between V_{Ti}^{4-} defective supercell and pure supercell calculated with the quasi-harmonic (QHA) and harmonic approximation (HA), respectively.

The calculated Gibbs free energy difference between the V_{Ti}^{4-} defective and pure supercells drops with volume expansion noticeably as shown in Figure 4.14. This substantial decrease is caused by the decrease of internal energy difference with volume

expansion as shown in Figure 4.15. Internal energy and strain energy trend in the same direction.

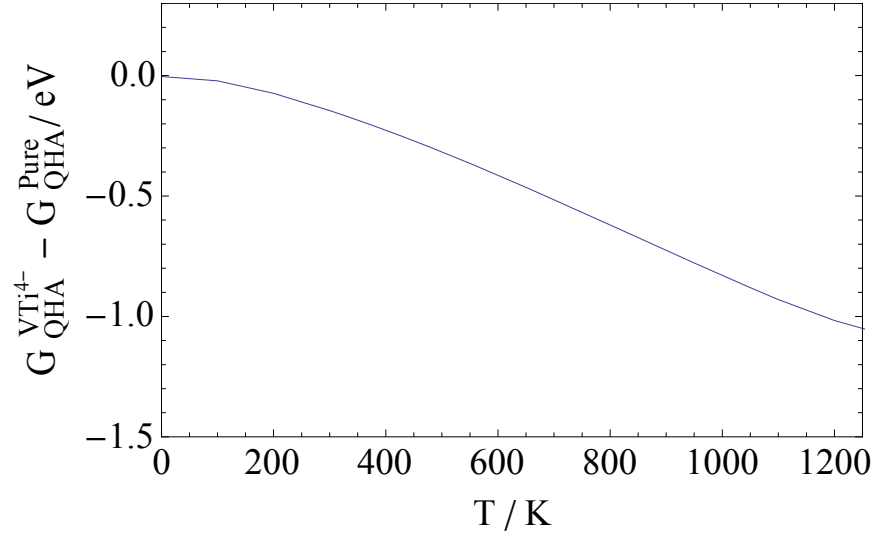


Figure 4.14 The Gibbs free energy difference between V_{Ti}^{4-} defective and pure supercells calculated with the quasi-harmonic approximation.

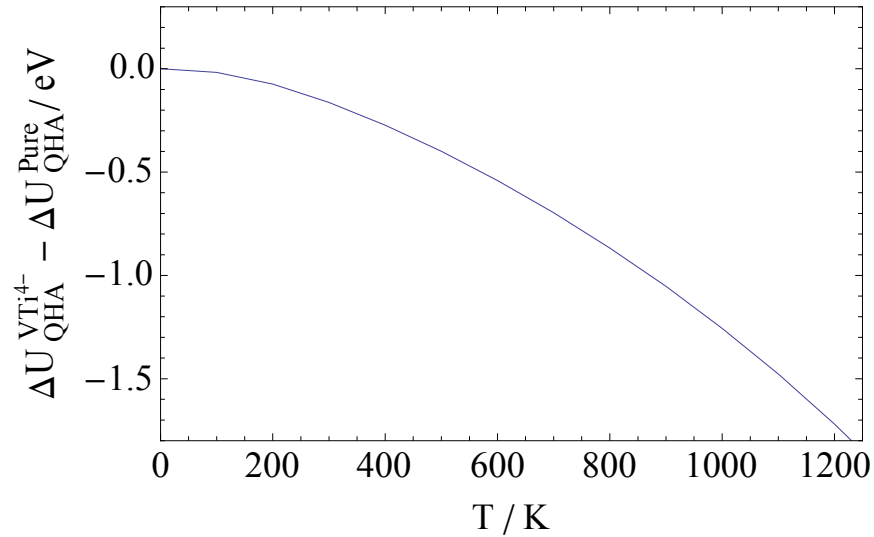


Figure 4.15 ΔU differences between V_{Ti}^{4-} defective supercell and the pure supercell calculated from the quasi-harmonic approximation. ΔU is the internal energy change referenced to the one at 0K.

In the V_O^{2+} and V_O^{1+} defective supercells the phonon free energies still increase more quickly with volume expansion when calculated with the QHA than with the HA. The internal energy differences between the V_O^{q+} supercells and pure supercell increase with volume expansion, but the internal energy difference for the V_O^{2+} supercell increases more quickly.

4.3 Defect Phase Diagrams

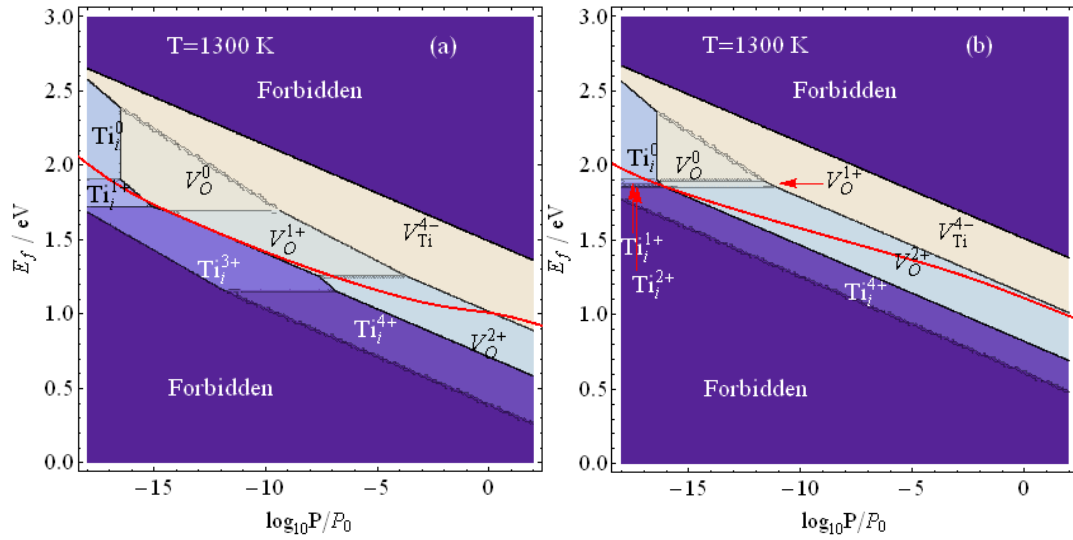


Figure 4.16 Calculated 2-D defect phase diagrams for rutile TiO_2 at 1300K based on (a) the Gibbs free energies G as defined in eq (2.1) and (b) the internal energies U as defined in eq (2.2). The calculated unique Fermi level (E_F) from the electroneutrality condition as a function of PO_2 at 1300K is labeled by red line.

The calculated 2-D defect phase diagrams in Figure 4.16 show only the dominant defects (lowest energy) in each region in the E_f - PO_2 space at 1300K. Results for the dominant defects vary depending on whether the full Gibbs free energies are used, as in Figure 4.16(a), or if only the internal energies are used, as in Figure 4.16(b). The major difference is the dominant regions for the partially charged point defects of V_O^{1+} and Ti_i^{3+} extend much more broadly when the Gibbs free energy is considered, which is due to the smaller increase of the Gibbs free energies with T for these partially charged defects compared to fully charged defects, as shown Figure 4.12. This gives the chance for the partially charged defects to be dominant in the low PO_2 region, which is not observed if only the internal energies are considered.

The charged defects in rutile are governed by the electroneutrality condition:

$$\sum_{\alpha} q_{\alpha} N_{\alpha} - n + p = 0 \quad (4.2)$$

where q_{α} and N_{α} are the charge state and concentration of defect α , respectively, n and p are the electron and hole concentrations, respectively. The point defect concentration is calculated by $N_{site} e^{-\Delta G/kT}$ where N_{site} is the number of sites the particular defect can occupy, while the electron and hole concentrations are calculated by $N_c e^{-(E_g - E_f)/kT}$ and $N_v e^{-E_f/kT}$, respectively, with N_c and N_v being the density of states for electrons and holes.

$$N_c = \frac{1}{4} \left(\frac{2m_c kT}{\pi \hbar^2} \right)^{3/2} \quad (4.3)$$

$$N_v = \frac{1}{4} \left(\frac{2m_v kT}{\pi \hbar^2} \right)^{3/2} \quad (4.4)$$

The bandgap, E_g , and electron and hole effective masses, m_e and m_v respectively, are all taken from experimental values[2, 6, 82, 83]. Thus, the only unknown quantity is E_f , which can be calculated from eq (4.2) at a given T and PO_2 . The result for E_f is shown in Figure 4.16 as a function of PO_2 at 1300K.

The positions of the unique Fermi levels in Figure 4.16 convey useful information. First, the calculation of the Fermi level with the Gibbs free energies in Figure 4.16(a) captures the n-p transition point of around 1 atm at 1300K correctly[1, 3, 5, 6], while the calculation with the internal energies in Figure 4.16(b) does not. This is mostly due to the decrease of the Gibbs free energy difference between V_{Ti}^{4+} and the pure supercell with T shown in Figure 4.14. Second, the calculation with Gibbs free energy suggests it is likely in the n-p transition region close to the atmospheric that the dominant defects are a combination of V_{Ti}^{4+} and V_O^{2+} [3]. At relatively reduced PO_2 levels V_O^{2+} defects are dominant [3, 5, 8]. In the highly reduced PO_2 region, the calculation indicates that either Ti_i^{3+} [8, 84] or V_O^{1+} can be the dominant defect. Lee and Yoo [8] and Blumenthal et al.[5] suggest at this temperature range Ti_i^{4+} may be dominant in a very narrow PO_2 range around 10^{-10} atm from their measured log-log slope of -1/5. This may be alternatively explained by a transition region from dominant V_O^{2+} with slope -1/6 to dominant Ti_i^{3+} or V_O^{1+} with slope -1/4 from our calculation. However, since the absolute values of the phonon free energies calculated in the 2x2x3 sized supercells are not fully converged

with respect to the supercell size as discussed in section 3.3.3, additional calculations of phonon free energy in larger supercells may extend the defect region of Ti_i^{4+} into the lower PO_2 region and allow it to overlap with the path of the unique Fermi level. Third, the calculation suggests it is not likely that Ti_i^{4+} defects dominant in a whole PO_2 range at this temperature, which disagrees with the analysis from Baumard[1, 6].

With the calculated unique Fermi level and DFEs of all the intrinsic defects, the Brower diagram, which originally can only be schematically shown through the defect mass action analysis, can be further calculated at any given temperature as shown in Figure 4.17, to give all the defect and carrier concentrations. It is worth noting that these quasi-harmonic phonon calculations in the defective supercells are computationally expensive. Each type of the defect requires around 80K computational units, or 500 dedicated CPUs to complete the calculation within seven days. Thus, the current calculation does not extend to higher temperatures than 1300K for the defective supercells. However, in principle the current methodology of DFE calculation built in this work can be applied to higher temperatures for most binary oxide systems as long as the structures are stable in the T and PO_2 regions. The dominant defect phase diagram shown in Figure 4.16, together with the unique Fermi level, can be used to adjust and control the dominant intrinsic defect types in a certain material by environmental variables such as T and PO_2 or the dopant levels, to further achieve the ideal electrical properties of any particular interest.

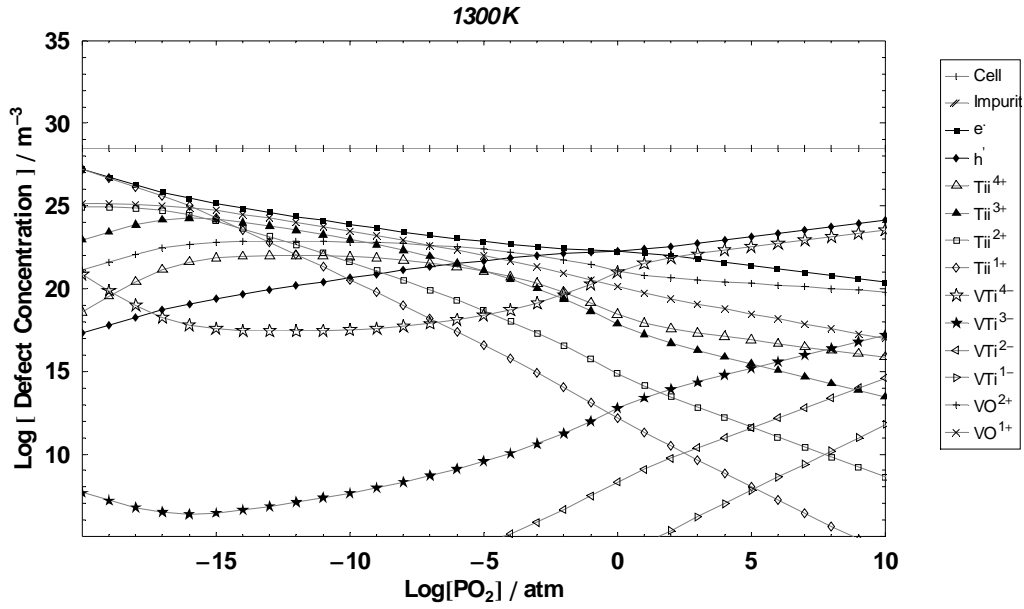


Figure 4.17 Calculated Brower diagram for rutile TiO_2 at 1300K.

4.4 Conclusions

A methodology of calculating DFEs in the PO_2 - T - E_f spaces was built for rutile TiO_2 , which can be applied to similar binary oxide systems. The defect phonon free energies were calculated with both harmonic and quasi-harmonic approximations. The thermal expansion effect was shown to be able to change the phonon free energy and internal energy of the defect structure in a nontrivial way, which can stabilize the partially charged Ti_i^{3+} and V_o^{1+} in the low PO_2 region and fully charged $\text{V}_{\text{Ti}}^{4-}$ in the n-p transition region. Finally, the unique Fermi level is calculated by applying the electroneutrality condition to give the defect concentration as a function of T and PO_2 and the Brower diagrams.

4.5 Future Work

Because of the computational limitation, the current frozen phonon calculation only considers the defective supercells as 1x1x1 sized new unit structures, which is only precise for the frequencies at the Gamma point. To sample the whole Brillouin zone, at least 2x2x2 sized new structures with the current supercells as unit are necessary, which may become computationally applicable in a few years.

For the Ti_i^{4+} defective supercell, the lowest optical phonon mode drops to negative frequencies very quickly with volume expansion, which may indicate a defect structure transition at high temperatures. More detailed studies of this particular phonon mode are necessary to explore whether a transition can happen.

Further calculation of the dielectric constant of certain defect structure with volume expansion may suggest some useful applications.

Appendix

Defect Mass Action Relation

For fully charged Ti interstitial:

$$\begin{aligned} Ti_{Ti} + 2O_O + V_I &\rightleftharpoons O_2 + Ti_i^{4+} + 4e' \\ n &\approx C_1 P(O_2)^{-1/5} \end{aligned} \quad (A.1)$$

For fully charged O vacancy:

$$\begin{aligned} O_O &\rightleftharpoons 1/2 O_2 + V_O^{2+} + 2e' \\ n &\approx C_2 P(O_2)^{-1/6} \end{aligned} \quad (A.2)$$

For +1 charged O vacancy:

$$\begin{aligned} O_O &\rightleftharpoons 1/2 O_2 + V_O^{1+} + e' \\ n &\approx C_3 P(O_2)^{-1/4} \end{aligned} \quad (A.3)$$

For +3 charged Ti interstitial:

$$\begin{aligned} Ti_{Ti} + 2O_O + V_I &\rightleftharpoons O_2 + Ti_i^{3+} + 3e' \\ n &\approx C_1 P(O_2)^{-1/4} \end{aligned} \quad (A.4)$$

Bibliography

- [1] Baumard JF, Panis D, Ruffier D. Electrical-Conductivity of Rutile Single-Crystals at High-Temperature. *Revue Internationale Des Hautes Temperatures Et Des Refractaires* 1975;12:321-327.
- [2] Baumard JF, Tani E. Electrical-Conductivity and Charge Compensation in Nb Doped TiO_2 Rutile. *Journal of Chemical Physics* 1977;67:857-860.
- [3] Nowotny MK, Bak T, Nowotny J. Electrical properties and defect chemistry of TiO_2 single crystal. I. Electrical conductivity. *Journal of Physical Chemistry B* 2006;110:16270-16282.
- [4] Lee DK, Jeon JL, Kim MH, Choi W, Yoo HI. Oxygen nonstoichiometry (δ) of $\text{TiO}_{2-\delta}$ -revisited. *Journal of Solid State Chemistry* 2005;178:185-193.
- [5] Blumenthal Rn, Baukus J, Hirthe WM. Studies of Defect Structure of Nonstoichiometric Rutile TiO_{2-x} . *Journal of the Electrochemical Society* 1967;114:172-&.
- [6] D.M.Smyth. *The Defect Chemistry of Metal Oxides*. New York: Oxford University Press, 2000.
- [7] Balachandran U, Eror NG. Electrical-Conductivity in Non-Stoichiometric Titanium-Dioxide at Elevated-Temperatures. *Journal of Materials Science* 1988;23:2676-2682.
- [8] Lee DK, Yoo HI. Unusual oxygen re-equilibration kinetics of $\text{TiO}_{2-\delta}$. *Solid State*

Ionics 2006;177:1-9.

[9] Ikeda JAS, Chiang YM. Space-Charge Segregation at Grain-Boundaries in Titanium-Dioxide .1. Relationship between Lattice Defect Chemistry and Space-Charge Potential. Journal of the American Ceramic Society 1993;76:2437-2446.

[10]Ikeda JAS, Chiang YM, Garrattreed AJ, Vandersande JB. Space-Charge Segregation at Grain-Boundaries in Titanium-Dioxide .2. Model Experiments. Journal of the American Ceramic Society 1993;76:2447-2459.

[11]Kohan AF, Ceder G, Morgan D, Van de Walle CG. First-principles study of native point defects in ZnO. Physical Review B 2000;61:15019-15027.

[12]Zheng JX, Ceder G, Maxisch T, Chim WK, Choi WK. First-principles study of native point defects in hafnia and zirconia. Physical Review B 2007;75:-.

[13]Li X, Finnis MW, He J, Behera RK, Phillpot SR, Sinnott SB, Dickey EC. Energetics of charged point defects in rutile TiO₂ by density functional theory Acta Materialia 2009;57:5882-5891.

[14]Oba F, Togo A, Tanaka I, Paier J, Kresse G. Defect energetics in ZnO: A hybrid Hartree-Fock density functional study. Physical Review B 2008;77:-.

[15]Zheng JX, Ceder G, Maxisch T, Chim WK, Choi WK. Native point defects in yttria and relevance to its use as a high-dielectric-constant gate oxide material: First-principles study. Physical Review B 2006;73:-.

[16]Janotti A, Van de Walle CG. Oxygen vacancies in ZnO. Applied Physics Letters 2005;87:-.

- [17]Cho E, Han S, Ahn HS, Lee KR, Kim SK, Hwang CS. First-principles study of point defects in rutile TiO_{2-x} . *Physical Review B* 2006;73:-.
- [18]Iddir H, Ogut S, Zapol P, Browning ND. Diffusion mechanisms of native point defects in rutile TiO_2 : Ab initio total-energy calculations. *Physical Review B* 2007;75:-.
- [19]He J, Sinnott SB. Ab initio calculations of intrinsic defects in rutile TiO_2 . *Journal of the American Ceramic Society* 2005;88:737-741.
- [20]He J, Behera RK, Finnis MW, Li X, Dickey EC, Phillpot SR, Sinnott SB. Prediction of high-temperature point defect formation in TiO_2 from combined ab initio and thermodynamic calculations. *Acta Materialia* 2007;55:4325-4337.
- [21]Makov G, Payne MC. Periodic Boundary-Conditions in Ab-Initio Calculations. *Physical Review B* 1995;51:4014-4022.
- [22]Ma XG, Jiang JJ, Liang P, Wang J. An accurate theoretical study on intrinsic defect energetics in rutile TiO_2 . *Transactions of Nonferrous Metals Society of China* 2007;17:S50-S54.
- [23]Baldereschi A, Baroni S, Resta R. Band Offsets in Lattice-Matched Heterojunctions - a Model and 1st-Principles Calculations for GaAs/Alas. *Physical Review Letters* 1988;61:734-737.
- [24]Van de Walle CG, Neugebauer J. First-principles calculations for defects and impurities: Applications to III-nitrides. *Journal of Applied Physics* 2004;95:3851-3879.
- [25]Finazzi E, Di Valentin C, Pacchioni G. Nature of Ti Interstitials in Reduced Bulk Anatase and Rutile TiO_2 . *Journal of Physical Chemistry C* 2009;113:3382-3385.

- [26]Erhart P, Albe K. Modeling the electrical conductivity in BaTiO₃ on the basis of first-principles calculations. Journal of Applied Physics 2008;104:-.
- [27]Batyrev I, Alavi A, Finnis MW. Ab initio calculations on the Al₂O₃(0001) surface. Faraday Discussions 1999;33-43.
- [28]Blumenth.Rn, Kirk JC, Hirthe WM. Electronic Mobility in Rutile (TiO₂) at High Temperatures. Journal of Physics and Chemistry of Solids 1967;28:1077-&.
- [29]Zhang SB, Northrup JE. Chemical-Potential Dependence of Defect Formation Energies in Gaas - Application to Ga Self-Diffusion. Physical Review Letters 1991;67:2339-2342.
- [30]Lozovoi AT, Alavi A, Finnis MW. Surface energy and the early stages of oxidation of NiAl(110). Computer Physics Communications 2001;137:174-194.
- [31]NIST data base. <http://webbook.nist.gov/chemistry/>.
- [32]Finnis MW, Lozovoi AY, Alavi A. The oxidation of NiAl: What can we learn from ab initio calculations? Annual Review of Materials Research 2005;35:167-207.
- [33]Hohenberg P, Kohn W. Inhomogeneous Electron Gas. Physical Review B 1964;136:B864-&.
- [34]Kohn W, Sham LJ. Self-Consistent Equations Including Exchange and Correlation Effects. Physical Review 1965;140:1133-&.
- [35]Perdew JP, Burke K, Ernzerhof M. Generalized gradient approximation made simple. Physical Review Letters 1996;77:3865-3868.
- [36]Perdew JP, Ernzerhof M, Burke K. Rationale for mixing exact exchange with density

- functional approximations. *Journal of Chemical Physics* 1996;105:9982-9985.
- [37]Heyd J, Scuseria GE, Ernzerhof M. Hybrid functionals based on a screened Coulomb potential. *Journal of Chemical Physics* 2003;118:8207-8215.
- [38]Martin RM. *Electronic Structure: Basic Theory and Practical Methods*: Cambridge University Press, 2004.
- [39]Kresse G, Furthmuller J. Efficient iterative schemes for ab initio total-energy calculations using a plane-wave basis set. *Physical Review B* 1996;54:11169-11186.
- [40]Kresse G, Joubert D. From ultrasoft pseudopotentials to the projector augmented-wave method. *Physical Review B* 1999;59:1758-1775.
- [41]Blochl PE. Projector Augmented-Wave Method. *Physical Review B* 1994;50:17953-17979.
- [42]Leslie M, Gillan MJ. The Energy and Elastic Dipole Tensor of Defects in Ionic-Crystals Calculated by the Supercell Method. *Journal of Physics C-Solid State Physics* 1985;18:973-982.
- [43]Bader RFW. *Atoms in Molecules: A Quantum Theory*. Oxford: Clarendon Press, 1990.
- [44]Parker RA. Static Dielectric Constant of Rutile (TiO₂), 1.6-1060 Degrees K. *Physical Review* 1961;1:1719-&.
- [45]Binks JH, Duffy JA. Ionicity of Simple Binary Oxides. *Journal of the Chemical Society-Faraday Transactions II* 1985;81:473-478.
- [46]Raebiger H, Lany S, Zunger A. Charge self-regulation upon changing the oxidation

state of transition metals in insulators. *Nature* 2008;453:763-766.

[47]Castleton CWM, Hoglund A, Mirbt S. Managing the supercell approximation for charged defects in semiconductors: Finite-size scaling, charge correction factors, the band-gap problem, and the ab initio dielectric constant. *Physical Review B* 2006;73:-.

[48]Freysoldt C, Neugebauer J, Van de Walle CG. Fully Ab Initio Finite-Size Corrections for Charged-Defect Supercell Calculations. *Physical Review Letters* 2009;102:-.

[49]Zhu J, Yu JX, Wang YJ, Chen XR, Jing FQ. First-principles calculations for elastic properties of rutile TiO₂ under pressure. *Chinese Physics B* 2008;17:2216-2221.

[50]Anderson PW. Model for Electronic-Structure of Amorphous-Semiconductors. *Physical Review Letters* 1975;34:953-955.

[51]Jacob KT, Hoque SM, Waseda Y. Synergistic use of thermogravimetric and electrochemical techniques for thermodynamic study of TiO_x ($1.67 \leq x \leq 2.0$) at 1573 K. *Materials Transactions Jim* 2000;41:681-689.

[52]Gonze X. First-principles responses of solids to atomic displacements and homogeneous electric fields: Implementation of a conjugate-gradient algorithm. *Physical Review B* 1997;55:10337-10354.

[53]Baroni S, Giannozzi P, Testa A. Green-Function Approach to Linear Response in Solids. *Physical Review Letters* 1987;58:1861-1864.

[54]Ackland GJ, Warren MC, Clark SJ. Practical methods in ab initio lattice dynamics. *Journal of Physics-Condensed Matter* 1997;9:7861-7872.

[55]Frank W, Elsasser C, Fahnle M. Ab-Initio Force-Constant Method for Phonon

Dispersions in Alkali-Metals. Physical Review Letters 1995;74:1791-1794.

[56]Kresse G, Hafner J. Abinitio Hellmann-Feynman Molecular-Dynamics for Liquid-Metals. Journal of Non-Crystalline Solids 1993;156:956-960.

[57]Parlinski K, Li ZQ, Kawazoe Y. First-principles determination of the soft mode in cubic ZrO₂. Physical Review Letters 1997;78:4063-4066.

[58]Sikora R. Ab initio study of phonons in the rutile structure of TiO₂. Journal of Physics and Chemistry of Solids 2005;66:1069-1073.

[59]Mattsson TR, Sandberg N, Armiento R, Mattsson AE. Quantifying the anomalous self-diffusion in molybdenum with first-principles simulations. Physical Review B 2009;80:-.

[60]Mantina M, Wang Y, Arroyave R, Chen LQ, Liu ZK, Wolverton C. First-principles calculation of self-diffusion coefficients. Physical Review Letters 2008;100:-.

[61]Lucas G, Schaublin R. Vibrational contributions to the stability of point defects in bcc iron: A first-principles study. Nuclear Instruments & Methods in Physics Research Section B-Beam Interactions with Materials and Atoms 2009;267:3009-3012.

[62]Al-Mushadani OK, Needs RJ. Free-energy calculations of intrinsic point defects in silicon. Physical Review B 2003;68:-.

[63]Estreicher SK, Sanati M, West D, Ruymgaart F. Thermodynamics of impurities in semiconductors. Physical Review B 2004;70:-.

[64]El-Mellouhi F, Mousseau N. Thermally activated charge reversibility of gallium vacancies in GaAs. Journal of Applied Physics 2006;100:-.

- [65]Born M, Huang K. Dynamical theory of crystal lattices. Oxford: Clarendon Press, 1954.
- [66]Togo A. <http://fropo.sourceforge.net/>.
- [67]Kittel C. Introduction to Solid State Physics: John Wiley & Sons, Inc., 2005.
- [68]Ashcroft, Mermin. Solid State Physics: Thomson Learning, Inc., 1976.
- [69]Landau LD, Lifshitz EM. Course of Theoretical Physics, Statistical Physics, Part I. Oxford: Butterworth & Heinemann, 1980.
- [70]Montanari B, Harrison NM. Lattice dynamics of TiO₂ rutile: influence of gradient corrections in density functional calculations. Chemical Physics Letters 2002;364:528-534.
- [71]Porto SPS, Fleury PA, Damen TC. Raman Spectra of TiO₂,MgF₂,ZnF₂,FeF₂,and MnF₂. Physical Review 1967;154:522-&.
- [72]Eagles DM. Polar Modes of Lattice Vibration + Polaron Coupling Constants in Rutile (TiO₂). Journal of Physics and Chemistry of Solids 1964;25:1243-&.
- [73]Trayler JG, Smith HG, Nicklow RM, Wilkins MK. Lattice Dynamics of Rutile. Physical Review B 1971;3:3457-&.
- [74]Srivastava GP. The Physics of Phonons. New York: Taylor & Francis, 1990.
- [75]Finnis MW. Interatomic forces in condensed matter: OXFORD, 2005.
- [76]Samara GA, Peercy PS. Pressure and Temperature-Dependence of Static Dielectric-Constants and Raman-Spectra of TiO₂ (Rutile). Physical Review B 1973;7:1131-1148.

- [77]Liu Y, Ni LH, Ren ZH, Xu G, Song CL, Han GR. Negative pressure induced ferroelectric phase transition in rutile TiO_2 . Journal of Physics-Condensed Matter 2009;21:-.
- [78]Kern G, Kresse G, Hafner J. Ab initio calculation of the lattice dynamics and phase diagram of boron nitride. Physical Review B 1999;59:8551-8559.
- [79]Oganov AR, Dorogokupets PI. All-electron and pseudopotential study of MgO : Equation of state, anharmonicity, and stability. Physical Review B 2003;67:-.
- [80]Wallace DC. Thermodynamics of Crystal. New York: Wiley, 1972.
- [81]Isaak DG, Carnes JD, Anderson OL, Cynn H, Hake E. Elasticity of TiO_2 rutile to 1800 K. Physics and Chemistry of Minerals 1998;26:31-43.
- [82]Bak T, Nowotny J, Nowotny MK. Defect disorder of titanium dioxide. Journal of Physical Chemistry B 2006;110:21560-21567.
- [83]Bak T, Nowotny J, Rekas M, Sorrell CC. Defect chemistry and semiconducting properties of titanium dioxide: III. Mobility of electronic charge carriers. Journal of Physics and Chemistry of Solids 2003;64:1069-1087.
- [84]Nowotny J, Bak T, Nowotny MK, Sheppard LR. Defect chemistry and electrical properties of titanium dioxide. 1. Defect diagrams. Journal of Physical Chemistry C 2008;112:590-601.

Vita

Xin Li

Education

2005 ~ 2010 PhD, Materials Science and Engineering,
Pennsylvania State University

2004 ~ 2005 PhD Candidate, Physics, University of Georgia

1999 ~ 2003 BS, Physics, Nanjing University, China

Awards

Dec, 2009 MRS (Materials Research Society) Graduate
Student Silver Award